

# Optical hot carrier solar cell: A general method of spectrum management in photovoltaics

**Author:**

YANG, Jianfeng

**Publication Date:**

2018

**DOI:**

<https://doi.org/10.26190/unsworks/20246>

**License:**

<https://creativecommons.org/licenses/by-nc-nd/3.0/au/>

Link to license to see what you are allowed to do with this resource.

Downloaded from <http://hdl.handle.net/1959.4/59632> in <https://unsworks.unsw.edu.au> on 2024-05-04

# Optical hot carrier solar cell: A general method of spectrum management in photovoltaics

Jianfeng Yang

Supervised by  
Prof. Gavin Conibeer  
Dr. Robert Patterson  
Dr. Xiaoming Wen  
Dr. Santosh Shrestha  
Dr. Shujuan Huang

A thesis in fulfilment of the requirements for the degree of  
Doctor of Philosophy



School of Photovoltaic and Renewable Energy Engineering  
Faculty of Engineering

5 January 2018



PLEASE TYPE

THE UNIVERSITY OF NEW SOUTH WALES  
Thesis/Dissertation Sheet

Surname or Family name: Yang

First name: Jianfeng

Other name/s:

Abbreviation for degree as given in the University calendar:  
SOLABR1655

School: School of Photovoltaic and Renewable Energy  
Engineering

Faculty: Faculty of Engineering

Title: Optical hot carrier solar cell: A general method of spectrum  
management in photovoltaics

Abstract 350 words maximum: (PLEASE TYPE)

The design and operating principles of the optical hot carrier solar cell (OHCS) have been investigated in this thesis. An OHCS integrates a hot carrier absorber and a conventional solar cell using a photonic structure called the optical contact, which enhances the carrier hot-luminescence transfer rate at the bandgap frequency of the solar cell to reduce the thermalization losses during photovoltaic conversion. Such an optically-integrated system has the physical features of both a hot carrier solar cell and a spectrum up/down converter. Therefore, it is a valuable general method to explore spectrum management for solar cells.

One goal of this study was to establish a comprehensive understanding of the device characteristics in both thermal equilibrium (detailed-balance) and non-equilibrium (relaxation-time-approximation) steady states. These demonstrate the general efficiency enhancement conditions for the optically-integrated system and particular dependencies of its operating voltage on the luminescence yield. The device performance relies on the slow carrier cooling rate in the absorber and the large enough luminescence enhancement ratio of the optical contact, which is on the order of ~1 ns and ~1000 x for the up-converter while ~500 ps and ~100 x for the down-converter.

The second aspect was to develop a theoretical framework for the analysis of the optical contacts. Using the electromagnetic Green's functions constructed by the quasi-normal modes, the photon transfer spectrum function can quantify the coupling rate more accurately, especially for the near-field coupling. The hot-luminescence transfer has been investigated in detail using a plasmonic core-shell nanowire illustration, which shows about 4800 times transfer enhancement and an improved device performance in up-conversions.

This study also explored hot carrier absorber candidates in the lead-halide perovskite family ( $\text{APbX}_3$ ) using ultrafast optical characterization and first-principle calculations. A stronger phonon bottleneck effect was shown in hybrid perovskites than in their inorganic counterparts to prolong the carrier cooling period. At least a 10 times slower carrier-phonon relaxation rate was observed in  $\text{FAPbI}_3$  comparing to the cesium-based inorganic system. The up-conversion of low-energy phonons has been proposed to be responsible for the bottleneck effect, which also suggests a general way for achieving long-lived hot carriers in materials.

Declaration relating to disposition of project thesis/dissertation

I hereby grant to the University of New South Wales or its agents the right to archive and to make available my thesis or dissertation in whole or in part in the University libraries in all forms of media, now or here after known, subject to the provisions of the Copyright Act 1968. I retain all property rights, such as patent rights. I also retain the right to use in future works (such as articles or books) all or part of this thesis or dissertation.

I also authorise University Microfilms to use the 350 word abstract of my thesis in Dissertation Abstracts (theses only).

.....

The University recognises that there may be exceptional circumstances requiring restrictions on copying or conditions on use. Requests for restriction for a period of up to 2 years must be made in writing. Requests for a longer period of restriction may be considered in exceptional circumstances and require the approval of the Dean of Graduate Research.

FOR OFFICE USE ONLY

Date of completion of requirements for Award:

**ORIGINALITY STATEMENT**

'I hereby declare that this submission is my own work and to the best of my knowledge it contains no materials previously published or written by another person, or substantial proportions of material which have been accepted for the award of any other degree or diploma at UNSW or any other educational institution, except where due acknowledgement is made in the thesis. Any contribution made to the research by others, with whom I have worked at UNSW or elsewhere, is explicitly acknowledged in the thesis. I also declare that the intellectual content of this thesis is the product of my own work, except to the extent that assistance from others in the project's design and conception or in style, presentation and linguistic expression is acknowledged.'

Signed .....

Date .....

**COPYRIGHT STATEMENT**

'I hereby grant the University of New South Wales or its agents the right to archive and to make available my thesis or dissertation in whole or part in the University libraries in all forms of media, now or here after known, subject to the provisions of the Copyright Act 1968. I retain all proprietary rights, such as patent rights. I also retain the right to use in future works (such as articles or books) all or part of this thesis or dissertation.

I also authorise University Microfilms to use the 350 word abstract of my thesis in Dissertation Abstract International (this is applicable to doctoral theses only).

I have either used no substantial portions of copyright material in my thesis or I have obtained permission to use copyright material; where permission has not been granted I have applied/will apply for a partial restriction of the digital copy of my thesis or dissertation.'

Signed .....

Date .....

**AUTHENTICITY STATEMENT**

'I certify that the Library deposit digital copy is a direct equivalent of the final officially approved version of my thesis. No emendation of content has occurred and if there are any minor variations in formatting, they are the result of the conversion to digital format.'

Signed .....

Date .....



# Abstract

The design and operating principles of the optical hot carrier solar cell (OHCSC) have been investigated in this thesis. An OHCSC integrates a hot carrier absorber and a conventional solar cell using a photonic structure called the optical contact, which enhances the carrier hot-luminescence transfer rate at the bandgap frequency of the solar cell to reduce the thermalization losses during photovoltaic conversion. Such an optically-integrated system has the physical features of both a hot carrier solar cell and a spectrum up/down converter. Therefore, it is a valuable general method to explore spectrum management for solar cells.

One goal of this study was to establish a comprehensive understanding of the device characteristics in both thermal equilibrium (detailed-balance) and non-equilibrium (relaxation-time-approximation) steady states. These demonstrate the general efficiency enhancement conditions for the optically-integrated system and particular dependencies of its operating voltage on the luminescence yield. The device performance relies on the slow carrier cooling rate in the absorber and the large enough luminescence enhancement ratio of the optical contact, which is on the order of  $\sim 1$  ns and  $\sim 1000$  x for the up-converter while  $\sim 500$  ps and  $\sim 100$  x for the down-converter.

The second aspect was to develop a theoretical framework for the analysis of the optical contacts. Using the electromagnetic Green's functions constructed by the quasi-normal modes, the photon transfer spectrum function can quantify the coupling rate more accurately, especially for the near-field coupling. The hot-luminescence transfer has been investigated in detail using a plasmonic core-shell nanowire illustration, which shows about 4800 times transfer enhancement and an improved device performance in up-conversions.

This study also explored hot carrier absorber candidates in the lead-halide perovskite family ( $\text{APbX}_3$ ) using ultrafast optical characterization and first-principle calculations. A stronger phonon bottleneck effect was shown in hybrid perovskites than in their inorganic counterparts to prolong the carrier cooling period. At least a 10 times slower carrier-phonon relaxation rate was observed in  $\text{FAPbI}_3$  comparing to the cesium-based inorganic

---

system. The up-conversion of low-energy phonons has been proposed to be responsible for the bottleneck effect, which also suggests a general way for achieving long-lived hot carriers in materials.

# Acknowledgments

Thanks to the scholarship received from the Chinese Scholarship Council (CSC) and UNSW to support my overseas study. I would never have been able to finish this thesis without the aid and support of the following people.

First and most, I would like to thank my supervisors Prof. Gavin Conibeer, Dr. Robert Patterson, Dr. Xiaoming Wen, Dr. Santosh Shrestha, and Dr. Shujuan Huang who shared their knowledge and experience in both of the science and career with me. I want to offer my special thanks to Dr. Robert Patterson who has made lots of inspiring suggestions in my early stage of PhD and continuous support over the past four years. I would also like to thank Dr. Xiaoming Wen again for giving me the opportunity to join in the project of hot carriers in lead-halide perovskites.

I am grateful to some talented collaborators. Discussions with Dr. Yu Feng about the theoretical modeling of device operation and optics have been illuminating. Dr. Hongze Xia made his enormous contributions to the first-principle calculations of photon band structure. Dr. Xi Dai showed his knowledge of nanofabrication who also introduced me visit The Max Planck Institute for the Science of Light. Special thanks to Dr. Rongchun Ge at the Nanyang Technological University for the guidance and discussions about the quasi-normal mode theory, and to the team led by Prof. Tak W. Kee at the University of Adelaide for the support and discussion of transient absorption measurement. Also, thanks Dr. Dingding Ren at the Norwegian University of Science and Technology for the invitation to their exciting research of the nanowire laser and Dr. Michael Latzel at the MPI for his warm reception when I stayed in German.

I am indebted to many of my colleagues and friends, Mr. Zhilong Zhang, Mr. Weijian Chen, Mr. Bo Wang, Mr. Yuan Lin, Dr. Qingyuan He, and Dr. Haiyang Liu, who encourage and inspire me. There is no doubt that the friendship with them is another precious wealth of my harvest in Sydney.

I extend the profound gratitude to my families for their selfless and continuous support,

---

especially to my grandmother who raised me up, taught me the truth of life, and enlighten my curiosity to the natural science. Finally, to my girlfriend Elva Guo, thank you so much for all your love and accompany.

# Publication list

## Academic Journals

### First Authors

- (1) **Yang, J.**; Wen, X.; Xia, H.; Sheng, R.; Ma, Q.; Kim, J.; Tapping, P.; Harada, T.; Kee, T. W.; Huang, F.; Cheng, Y.-B.; Green, M.; Ho-Baillie, A.; Huang, S.; Shrestha, S.; Patterson, R.; Conibeer, G. Acoustic-Optical Phonon Up-Conversion and Hot-Phonon Bottleneck in Lead-Halide Perovskites. *Nat. Commun.* **2017**, *8*, 14120.
- (2) **Yang, J.**; Ge, R.; Zhang, Z.; Chen, W.; Wang, B.; Feng, Y.; Huang, S.; Shrestha, S.; Patterson, R.; Conibeer, G. Theoretical Investigation of Carrier Transfer by an Optical Contacting Scheme for Optoelectronic Application. *J. Appl. Phys.* **2016**, *119* (15), 153102.
- (3) **Yang, J.**; Patterson, R.; Feng, Y.; Shrestha, S.; Huang, S.; Conibeer, G. Investigation of the Working Principle in an Optically Coupled Hot-Carrier Solar Cell Using the Relaxation-Time Model. *Phys. Rev. Appl.* **2015**, *3* (4), 44006.

### Co-authors

- (4) Zhang, Z.; Chen, Z.; Zhang, J.; Chen, W.; **Yang, J.**; Wen, X.; Wang, B.; Kobamoto, N.; Yuan, L.; Stride, J. A.; others. Significant Improvement in the Performance of PbSe Quantum Dot Solar Cell by Introducing a CsPbBr<sub>3</sub> Perovskite Colloidal Nanocrystal Back Layer. *Adv. Energy Mater.* **2017**, *7* (5).
- (5) Wang, B.; Xia, H.; Zhang, Z.; **Yang, J.**; Patterson, R.; Huang, S.; Shrestha, S.; Conibeer, G. Ab Initio Calculation of Halide Ligand Passivation on PbSe Quantum Dot Facets. *RSC Adv.* **2016**, *6* (106), 104699–104707.
- (6) Heilmann, M.; Munshi, A. M.; Sarau, G.; Göbelt, M.; Tessarek, C.; Fauske, V. T.; van Helvoort, A. T. J.; **Yang, J.**; Latzel, M.; Hoffmann, B.; others. Vertically Oriented Growth of GaN Nanorods on Si Using Graphene as an Atomically Thin Buffer Layer. *Nano Lett.* **2016**, *16* (6), 3524–3532.
- (7) Chen, W.; Wen, X.; Latzel, M.; Heilmann, M.; **Yang, J.**; Dai, X.; Huang, S.; Shrestha, S.; Patterson, R.; Christiansen, S.; others. Nanoscale Characterization of Carrier Dynamic and Surface Passivation in InGaN/GaN Multiple Quantum Wells on GaN Nanorods. *ACS Appl. Mater. & Interfaces* **2016**, *8* (46), 31887–31893.
- (8) Zhang, Z.; **Yang, J.**; Wen, X.; Yuan, L.; Shrestha, S.; Stride, J. A.; Conibeer, G. J.; Patterson, R. J.; Huang, S. Effect of Halide Treatments on PbSe Quantum Dot

---

Thin Films: Stability, Hot Carrier Lifetime, and Application to Photovoltaics. *J. Phys. Chem. C* **2015**, *119* (42), 24149–24155.

## Conferences

### First Author

(9) **Yang, J.**; Chen, W.; Wang, B.; Zhang, Z.; Huang, S.; Shrestha, S.; Wen, X.; Patterson, R.; Conibeer, G. Selective Optical Contacting for Solar Spectrum Management. In *Proc. of SPIE Vol.*; **2017**; Vol. 10099, pp 1009911–1009917. (Poster Presentation)

(10) **Yang, J.**; Feng, Y.; Patterson, R.; Huang, S.; Shrestha, S.; Conibeer, G. Theoretical Investigation of Plasmon Enhanced Optically-Coupled Hot Carrier Extraction. In *Photovoltaic Specialist Conference (PVSC), 2015 IEEE 42nd*; **2015**; pp 1–4. (Oral Presentation)

### Co-author

(11) Chen, W.; Wen, X.; Latzel, M.; **Yang, J.**; Huang, S.; Shrestha, S.; Patterson, R.; Christiansen, S.; Conibeer, G. Nanoscale Characterization of GaN/InGaN Multiple Quantum Well on GaN Nanorods by Photoluminescence Spectroscopy. In *Proc. of SPIE Vol.*; **2017**; Vol. 10104, p 101040U–1.

(12) Dai, X.; Wen, X.; Latzel, M.; Heilmann, M.; Appelt, C.; Feng, Y.; **Yang, J.**; Chen, W.; Huang, S.; Shrestha, S.; others. Fabrication and Optical Characterisation of InGaN/GaN Nanorods. In *SPIE Micro + Nano Materials, Devices, and Applications*; **2015**; p 96680F–96680F.

(13) Conibeer, G.; Shrestha, S.; Huang, S.; Patterson, R.; Xia, H.; Feng, Y.; Zhang, P.; Gupta, N.; Smyth, S.; Liao, Y.; Lin, S.; Wang, P.; Dai, X.; Chung, S.; **Yang, J.**; Zhang, Y. Hot Carrier Solar Cell Absorbers: Investigation of Carrier Cooling Properties of Candidate Materials. In *SPIE Optics + Photonics for Sustainable Energy*; **2015**; p 956207.

## Under Preparation

(1) Ren, D; Ahtapodov, L; Nilsen, J.; **Yang, J.**; Gustafsson, A.; Hub, J.; Conibeer, G.; Helvoort, A.; Fimland, B.; Wenman, H. Single-mode Near-infrared Lasing in a GaAsSb/GaAs Nanowire Superlattice at Room Temperature, submitted to *Nature Communications*, arXiv:1708.06971(2017)

# The particular contributions of this thesis

**Contribution 1:** The potential and feasibility of the optical hot carrier solar cell are examined in a more practical consideration with detailed numerical examples and material characterizations. A more general concept of optically-coupled energy-selective spectrum conversion system has been developed whose operating characteristics and design principles are analyzed.

**Contribution 2:** The non-equilibrium steady state of the hot carrier luminescence converter is investigated using the relaxation-time-approximation model. It predicts a more reasonable device performance beyond the framework of detailed-balance.

**Contribution 3:** A complete theoretical framework has been developed to analyze the carrier hot-luminescence transfer through the optical energy selective contact and its applications in photovoltaics. Based on the Green's function method, the developed model illustrates the photonic dynamics of hot-luminescence transfer on a device level more accurately.

**Contribution 4:** More systematic characterizations and analyses have been done on the hot carrier dynamics in the lead-halide perovskites. The up-conversion of low energy acoustic phonons are proposed to explain the significant power-dependent phonon bottleneck effect observed in these materials.

---

# Abbreviations and notations

## Abbreviations

AI	Auger-recombination/Impact-ionization
DFT	density functional theory
DOS	density of states
EL	electroluminescence
ESC	energy selective contacts
FDT	fluctuation dissipation theorem
FDTD	finite-difference time-domain
HCA	hot carrier absorber
HCSC	hot carrier solar cell
LDOS	local density of optical states
MEG	multiple exciton generation
OESC	optical energy selective contact
OHSC	optical hot carrier solar cell
PCE	power conversion efficiency
PL	photoluminescence
PV	photovoltaic
QNM	quasi-normal mode
RTA	relaxation-time approximation
RTD	resonant tunneling diode
SPPs	surface plasmon polaritons
TA	transient absorption
WGM	whispering-gallery-mode

---

## Notation

$Q$	quality factor of resonance defined as $\omega_0/\Delta\omega$
$R_c$	optical concentration ratio of a solar cell
$X$	generalized optical étendue
$\Omega$	optical étendue
$\chi(\omega)$	photon transfer spectrum
$\dot{N}$	photon flux
$\dot{Q}$	optical power flux
$\mathbf{E}$	electric field with polarization component $E_a$
$\mathbf{G}(\mathbf{r}, \mathbf{r}_0; \omega)$	dyadic Green's function with polarization component $G_{ab}$
$\mathbf{p}(\mathbf{r}_0; \omega)$	density of radiative dipole moment with polarization component $p_a$
$\tau_x$	relaxation time of process $x$
$\tilde{\mathbf{f}}_\mu(\mathbf{r}; \omega_\mu)$	quasi-normal mode with modal index $\mu$ and real resonant frequency $\omega_\mu$
$\tilde{n}=n_r+i\kappa$	complex refractive index of material equals to $n_r + i\kappa$
$a$	optical absorptivity/emissivity (between 0 and 1)
$g_J$	gain ratio of short-circuit current density
$g_V$	gain ratio of open-circuit voltage
$g_\eta$	gain ratio of device power conversion efficiency
$m_e^*, m_h^*$	effective mass of electrons and holes
$n(\epsilon_e, t), p(\epsilon_h, t)$	electron's and hole's density on energy level $\epsilon$ at time delay $t$
$t$	time delay of a certain process
$\epsilon_e, \epsilon_h$	electronic energy level of electrons and holes respectively
$\epsilon=\epsilon'+i\epsilon''$	complex dielectric function

# Contents

<b>Abstract</b>	<b>v</b>
<b>Acknowledgments</b>	<b>vii</b>
<b>Publication list</b>	<b>ix</b>
<b>The particular contributions of this thesis</b>	<b>xi</b>
<b>Abbreviations and notations</b>	<b>xiii</b>
<b>1 Introduction</b>	<b>1</b>
1.1 General introduction of third generation photovoltaics . . . . .	1
1.2 Hot carrier solar cell and photonic engineering . . . . .	2
1.3 Thesis overview . . . . .	3
1.3.1 Brief summary of main chapters . . . . .	4
<b>2 Literature Review</b>	<b>7</b>
2.1 Background of hot carrier solar cell . . . . .	7
2.1.1 Energy losses in photovoltaic energy conversion . . . . .	7
2.1.2 Reducing thermalization losses by spectrum conversion . . . . .	8
2.1.3 Challenges in the hot carrier solar cell . . . . .	10
2.1.4 The possibility of hot carrier extraction via optical coupling . . . . .	11
2.2 Photonic engineering of semiconductor luminescence . . . . .	13
2.2.1 Fluorescence enhancement near metal nano-particles . . . . .	13
2.2.2 Purcell effects in the nano-structure . . . . .	14
2.2.3 Optical energy transformation via near-field coupling . . . . .	15
2.3 Brief introduction to methodology . . . . .	16
2.3.1 Theoretical basis of spontaneous emission . . . . .	16
2.3.2 Numerical modeling using finite-difference time-domain method . . . . .	17
2.3.3 Hot carrier detection using ultrafast transient absorption . . . . .	19
2.4 Summary and conclusions . . . . .	20
<b>3 Global Understanding of Optical Hot Carrier Solar Cell</b>	<b>21</b>
3.1 Introduction of optical hot carrier solar cell: in a perspective of spectrum conversion . . . . .	21
3.2 A practical condition in efficiency enhancement . . . . .	23
3.3 Photonic engineering in spectrum conversion system . . . . .	27
3.3.1 Photocurrent gain via optical energy selective contact . . . . .	30
3.3.2 Effect of frequency filter . . . . .	33
3.3.3 Influences on the open-circuit voltage and device efficiency . . . . .	34
3.4 Understanding luminescence transfer . . . . .	38

---

3.4.1	Internal luminescence and light extraction . . . . .	38
3.4.2	Increasing the luminescence transfer rate by photonic engineering . . . . .	39
3.5	Thermodynamic limit of spectrum conversion . . . . .	41
3.6	Conclusion . . . . .	42
<b>4</b>	<b>Investigation of Hot-luminescence Conversion using Relaxation-Time Approximation Model</b>	<b>43</b>
4.1	Introduction . . . . .	43
4.2	Relaxation-time-approximation model . . . . .	44
4.2.1	Relaxation approximation of carrier scattering . . . . .	45
4.2.2	Optical interaction with surroundings . . . . .	46
4.2.3	Estimation of device performance . . . . .	48
4.3	A case study for a down-conversion system . . . . .	48
4.3.1	Device model configuration . . . . .	48
4.3.2	Conversion efficiency and photon gain . . . . .	50
4.3.3	Effect of non-ideal carrier refilling . . . . .	54
4.3.4	Operation of PV cell . . . . .	55
4.4	Discussion . . . . .	56
4.4.1	Understanding the luminescence emission in the RTA . . . . .	56
4.4.2	Design requirements of the OHCSC . . . . .	57
4.4.3	Summary of dynamic features of device operation . . . . .	60
4.5	Conclusion . . . . .	61
<b>5</b>	<b>Optical Energy Selective Contact via Near-field Coupling</b>	<b>63</b>
5.1	Introduction . . . . .	63
5.2	Theoretical model of luminescence transfer . . . . .	65
5.2.1	Green's function evaluation using quasi-normal mode method . . . . .	66
5.2.2	Dipole density evaluation via fluctuation-dissipation theorem . . . . .	67
5.2.3	Luminescence transfer spectrum . . . . .	68
5.3	Optical contacting by a plasmonic core-shell nanowire . . . . .	70
5.3.1	Whispering-gallery mode of plasmonic nanowire . . . . .	71
5.3.2	Photon transfer spectra . . . . .	74
5.3.3	Carrier temperature dependent luminescence transfer . . . . .	76
5.3.4	Photovoltaic efficiency with hot-luminescence up-conversion . . . . .	78
5.4	Discussion . . . . .	81
5.5	Conclusions . . . . .	83
<b>6</b>	<b>Hot Carrier Dynamics in Lead-halide Perovskites</b>	<b>85</b>
6.1	Introduction: Lead-halide perovskites in photovoltaics . . . . .	86
6.2	Power dependent carrier cooling dynamics . . . . .	87
6.2.1	TA spectra of lead-halide perovskites . . . . .	87
6.2.2	Carrier temperature fitting . . . . .	89
6.2.3	Discussion on carrier temperature decay in lead-halide perovskites . . . . .	91
6.3	Phonon relaxation and bottleneck effect . . . . .	94
6.3.1	Review of carrier-phonon dynamics in semiconductors . . . . .	94
6.3.2	Phonon band structures of lead-halide perovskites . . . . .	95
6.3.3	Possibility of phonon up-conversion . . . . .	97
6.3.4	Hot phonon relaxation in lead-halide perovskites . . . . .	98
6.4	Discussion . . . . .	103
6.4.1	Proposed phonon dynamics in lead-halide perovskites . . . . .	103
6.4.2	Further discussions about phonon dynamics . . . . .	104

---

6.5	Conclusion . . . . .	105
<b>7</b>	<b>Conclusions</b>	<b>107</b>
7.1	Summaries of the thesis . . . . .	107
7.2	Future work . . . . .	110
	<b>Bibliography</b>	<b>111</b>
	<b>Appendices</b>	<b>125</b>
	<b>Appendix A Quasi-normal mode method</b>	<b>125</b>
A.1	Symbolic and formula conventions of electromagnetics . . . . .	125
A.2	Quasi-normal mode . . . . .	125
	<b>Appendix B LDOS and photon transfer spectrum</b>	<b>127</b>
	<b>Appendix C Methods of transient absorption characterization of lead-halide perovskites</b>	<b>129</b>
C.1	Sample preparation . . . . .	129
C.2	Ultrafast transient absorption . . . . .	131
C.3	Carrier injection level estimation . . . . .	132
C.4	Calculation of phonon band structure . . . . .	132
	<b>Appendix D Sensitivity and stability analysis of carrier temperature fitting in lead-halide perovskites</b>	<b>135</b>

---

# List of Figures

1.1	Overview of third-generation photovoltaics . . . . .	2
2.1	Energy losses during photovoltaic conversion . . . . .	8
2.2	Schematic illustration of electronic spectrum conversions. . . . .	9
2.3	Recent progress in the study of hot carrier solar cells . . . . .	11
2.4	The prototype of the optical hot carrier solar cell . . . . .	12
2.5	Purcell enhancements in nano-cavities . . . . .	14
2.6	Radiative transfer in a near-field coupling . . . . .	16
2.7	Schematic illustration of Yee's grid in FDTD method . . . . .	18
2.8	Carrier dynamics investigated by transient absorption spectroscopy . . . . .	19
3.1	Schematic demonstration of a general spectrum conversion system. . . . .	25
3.2	An example of a back-side up-converter device with optical enhancement. . . . .	29
3.3	The gain ratio of short-circuit current density in the up-conversion configuration. . . . .	31
3.4	The gain ratio of short-circuit current density in the down-conversion configuration. . . . .	32
3.5	Effects of an ideal frequency filter around the coupling frequency. . . . .	34
3.6	Carrier temperature and working voltage in a back-side up-converter. . . . .	36
3.7	Representative PCE enhancement $g_\eta$ ratio evaluated from two legendary configurations . . . . .	37
3.8	Luminescence transfer in the far-field coupling and near-field coupling . . . . .	39
4.1	Schematic illustration of multiple carrier evolution mechanisms in the optical hot carrier solar cell. . . . .	45
4.2	Overall conversion efficiency of the OHSCS under different bandgaps. . . . .	51
4.3	Dependence of photon gain ratio on the converter's bandgap. . . . .	52
4.4	The photon gain ratio under different emission enhancements and AI rates. . . . .	53
4.5	I-V curves of the down-conversion OHSCS under 1000-suns. . . . .	55
4.6	The gain ratio of conversion efficiency $g_\eta$ modeled by the RTA model with different carrier thermalization lifetime. . . . .	58
5.1	Schematic illustration of the optical contacting and theoretical framework . . . . .	65
5.2	A plasmonic core-shell nanowire structure acting as an OESC device . . . . .	70
5.3	Normalized mode profile of the $m = 1$ WGM used as the optical coupling channel. . . . .	72
5.4	The enhancement of in-plane LDOS by the WGM . . . . .	73
5.5	Photon transfer spectra in the cross sectional plane of the core-shell plasmonic nanowire. . . . .	75
5.6	Transferred photocurrent and power of hot-luminescence. . . . .	77
5.7	Normalized local power absorption and photocurrent spectra . . . . .	78

---

5.8	Device performance of the core-shell nanowire model examined by the detailed-balance model. . . . .	80
6.1	Transient absorption spectra of the FAPbI <sub>3</sub> sample. . . . .	88
6.2	TA spectrum pumped at 400 nm in the FAPbI <sub>3</sub> sample with different fluences	88
6.3	TA spectrum pumped at 400 nm in different samples . . . . .	89
6.4	High-energy tails on the normalized bleaching spectra of FAPbI <sub>3</sub> . . . . .	90
6.5	Time dependent carrier temperature in different samples and fluence . . . .	91
6.6	Phonon band structure and projected phonon density of states (DOS) in lead-halid perovskites(low energy) . . . . .	96
6.7	Phonon band structure and projected phonon DOS in lead-halid perovskites(high energy) . . . . .	97
6.8	Phonon dynamics in lead-halide perovskites . . . . .	99
6.9	LO phonon emission lifetime $\tau_{\text{ave}}$ versus carrier temperature $T_c$ . . . . .	101
6.10	LO phonon emission lifetime $\tau_{\text{ave}}$ varying with time delay $t$ . . . . .	102
6.11	Proposed phonon dynamics in the FAPbI <sub>3</sub> . . . . .	104
D.1	Averaged carrier temperature fitting results with different tail length $L$ . .	136
D.2	Statistical distribution of $S_R(t)$ to the carrier temperature fitted in lead-halide perovskites . . . . .	137
D.3	Statistical distribution of the normalized fitting standard error for the lead-halide perovskites . . . . .	138

# List of Tables

4.1	Generalized optical étendues $X$ and other optical parameters in the front-side down-conversion system with a planar geometry . . . . .	49
4.2	Electronic parameters used in the front-side down-conversion system . . . . .	50
4.3	Electronic parameters used in the modelings of Figure 4.6 . . . . .	59
C.1	Lattice constants used for phonon band structure calculation in DFT calculations . . . . .	133



# Chapter 1

## Introduction

An overview of the thesis presents in this opening chapter, which shows the motivations, contributions, and structural summaries of the thesis work.

### 1.1 General introduction of third generation photovoltaics

The increasing demand for clean and renewable energy is one of the challenges faced by human society in the 21<sup>st</sup> century. Among all the state-of-the-art technologies in renewable energy, the market share of photovoltaics (PV) has the fastest growth rate in the past ten years according to the latest report released by the International Renewable Energy Agency (IRENA) in 2017 [1]. Such a burst of growth relies on the rapid decrease in the levelized cost of energy (LCOE) of photovoltaics, which is where the story of third-generation photovoltaics (third-gen PV) begins.

The original concept of third-gen PV refers to the low-cost and high-efficiency solar cell with a unit watt price below 0.50 US\$/W [2, 3], comparing to the first-generation technique by silicon wafer and second-generation by thin-film as shown in Figure 1.1. In general, there are two unique characteristics of the third-gen PV which are a power conversion efficiency (PCE) higher than the single-junction limit examined by Shockley et al. [4] and also a quite low device cost per unit area. Both aspects cannot be achieved without an in-depth exploring in the fundamental physics behind the photovoltaic conversion. By addressing the intrinsic energy losses in a single junction solar cell, several novel device concepts have been proposed including 1) Tandem or multi-color cells; 2) Intermediate-band cells; 3) Multiple carrier excitations; 4) Spectrum up/down conversions; 5) Hot carrier solar cells [3]. Nearly all these concepts intend to improve the energy utilization efficiency of the broadband solar spectrum.

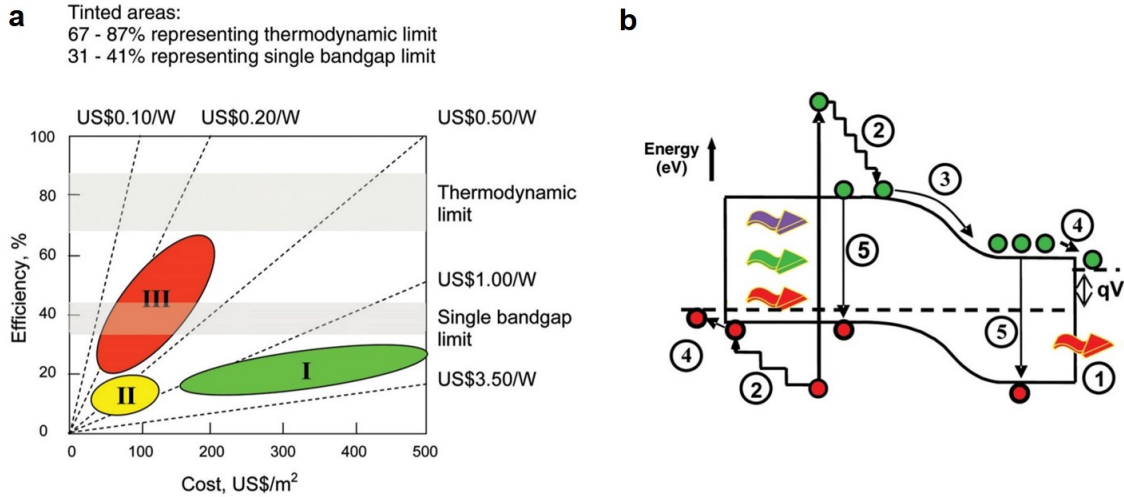


Figure 1.1: Overview of third-generation photovoltaics. (a) Efficiency and cost projections for first- (I), second- (II), and third-generation (III) PV technologies (wafer-based, thin films, and advanced thin films, respectively); (b) Loss processes in a standard solar cell: ① nonabsorption of below-bandgap photons; ② lattice thermalization loss; ③ and ④ junction and contact voltage losses; ⑤ recombination loss (radiative recombination is unavoidable) [3].

After about ten years<sup>1</sup> since the first emergence of the third-gen PV concept, the price limit of US\$0.50/W has been met by a huge cost decrease of silicon solar cells in about 2013 which continually falls to about US\$0.30/W in 2015 [5]. However, the study of breaking the single-junction limit without complex device architecture is still ongoing. Exploring novel physical mechanisms and new kind of conversion materials have become the forefront of research in photovoltaics today.

## 1.2 Hot carrier solar cell and photonic engineering

Among the third-gen PV concepts listed above, the hot carrier solar cell (HCSC) is different from others evidently in both of the device realization and operation.

The idea of HCSC originates from the thermodynamic insight of the photovoltaic mechanism in a semiconductor material [6, 7]. The photogenerated charge carriers release part of their kinetic energy as the electrochemical potential by intraband relaxation. However, this process is usually accompanied by significant non-ideal dissipations in conventional semiconductors, in particular for those high energy hot carriers (process ② in Figure 1.1(b)). Instead, by narrowing the energy bandwidth before and after the hot carrier relaxation, a higher voltage is achievable from a semiconductor device with the same electronic bandgap. Therefore, how to obviate non-ideal hot carrier relaxation and how to

<sup>1</sup>Multijunction cells were conceived in 1953 and first implemented in the 80's

export hot carriers via a narrow-band energy channel constitutes the two primary aspects of a HCSC.

The HCSC also has a close correlation with the spectrum up/down conversions. The essential methodology of spectrum conversion emphasizes the importance of a narrow band emission as well, where the host photovoltaic material reabsorbs the converted luminescence on its band edge referring to the monochromatic operation of a solar cell. Similar arguments in thermodynamics for the HCSC can be paraphrased here to explain a higher power efficiency achieved by the spectrum conversion system.

Recently, an optical coupling method was proposed by Farrell et al. [8] to export hot carriers as quasi-monochromatic hot-luminescence and then to pump a conventional solar cell with a matched bandgap. Such an optical hot carrier solar cell (OHCSC) combines the concept of the HCSC and spectrum up/down conversion directly. The prototype study showed an encouraging device performance, which is valuable for further development as a general spectrum management method for photovoltaics.

One fundamental aspect of the OHCSC is using photonic engineering to manage the luminescence transfer of hot carriers at selected photon energies. This is referred to as an optical energy selective contact (OESC). In contrast with common fluorescence, carrier thermalization usually occurs on much shorter timescales than the radiative recombination. A large enough optical enhancement is then necessary to improve the yield of carrier hot-luminescence with satisfactory monochromaticity. On the other hand, studying hot carrier generation in materials is important in order to gain further understanding of the carrier relaxation dynamics. It may be useful in investigating photovoltaics with higher efficiencies. These two areas comprise the major research topics of this thesis.

### 1.3 Thesis overview

This thesis investigates the potential and feasibility of the OHCSC in a more practical consideration with detailed numerical examples and material characterizations. It provides physical insights into the operating and design principles of the device. The OESC introduces a significant optical coupling between the solar cell and the hot carrier absorber, leading to a series of unique characteristics in such an all optically-integrated system.

This thesis focuses on the theoretical understanding of the device physics. In particular, analytical tools are developed to quantify the design and behavior of the OESC on a device level. Material characterization of ultrafast carrier dynamics is also involved in this

project suggesting an unusual mechanism to obtain long-lived hot carrier populations in semiconductor materials.

### 1.3.1 Brief summary of main chapters

**Chapter 2** is a systematic literature review of the background knowledge to explore the OHCS. It starts with the general background of spectrum management for photovoltaics in both of the optical and electronic ways. The following part shows the recent progress in the area of spontaneous emission control and near-field coupling, which is very encouraging for the implementation of the OESC in practice. The primary study tools in the theoretical, numerical, and experimental aspects are then discussed in the last part.

**Chapter 3** investigates the most general and global working principles of the OHCS within the traditional framework of detailed-balance and thermo-equilibrium. The major contributions include:

- 1) It analyzes the generality of the OHCS, which concludes the revealed device properties is also applicable to the conventional spectrum up/down conversion systems.

- 2) It shows the general necessary condition to increase the power conversion efficiency of the OHCS.

- 3) It reveals several unique working principles of the OHCS with an efficient OESC, especially those concerning the interaction between the yield of hot-luminescence in the hot carrier absorber and the working voltage of the integrated solar cell.

**Chapter 4** further investigates the device working principles beyond the framework of detailed-balance using the relaxation-time-approximation. The main contributions include:

- 1) It considers the device behavior in a non-equilibrium steady state and shows more reasonable spectrum conversion dynamics obeying the laws of thermodynamics;

- 2) Non-ideal energy losses have been well considered which predict the device performance based on more reasonable grounds. It also suggests more stringent design requirements in both of the optical enhancement and hot carrier lifetime.

- 3) A complete physical picture of the device operation is summarized at the end of this chapter.

**Chapter 5** explores the optical enhancement in luminescence transfer using rigorous electromagnetic theories to answer the requirements of optical enhancement asked by Chapter 4. The main contributions are:

1) A complete theoretical framework to analyze the luminescence transfer is developed based on the electromagnetic Green's function and fluctuation-dissipation theorem. The photon transfer spectrum is proposed as the figure-of-merit to characterize the effectiveness of photonic engineering to improve the intensity and monochromaticity of the carrier hot-luminescence.

2) In particular, quasi-normal mode method is used to describe a more accurate photonic dynamics in this energy transfer problem.

3) A plasmonic core-shell nanowire model is examined as the near-field OESC to embody the theoretical tools developed before, showing encouraging optical enhancement result. A comprehensive study of hot-luminescence transfer is also performed, ending with an investigation of the modified device performance.

**Chapter 6** investigates the hot carrier dynamics in lead-halide perovskites, which is proposed to be a novel candidate material in the hot carrier engineering recently with superb luminescence properties. This gives a better understanding of the hot phonon bottleneck effect observed in these kinds of materials. It will be helpful to develop the general method to achieve long-lived hot carriers for photovoltaics discussed in Chapter 4. The main contributions include

1) A systematic study of hot carrier cooling is performed on four kinds of lead-halide perovskites with different lattice composition using the transient absorption spectrum.

2) With the help of first-principle calculations, phonon relaxation is compared and analyzed among the four kinds of lead-halide perovskites.

3) The acoustics-to-optical up-conversion of the low energy phonons is proposed to explain the observed power-dependent phonon bottleneck effect occurring from several tens to thousands of picoseconds after the excitation.

**Chapter 7** concludes the main results achieved in previous chapters and also proposes several new study directions for the future.



## Chapter 2

# Literature Review

This chapter reviews and summarizes the research background, the theoretical basis, and the relevant methodologies of this thesis. The first part introduces the essential energy losses in the conventional single junction solar cell which encourage the exploration of solar spectrum management. The progress and challenges in the hot carrier solar cell (HCSC) are discussed subsequently as a representative third-generation photovoltaic (PV) concept to improve utilization of the broadband solar spectrum. Photonic engineering relevant to the optical energy selective contact (OESC) is also reviewed, which is followed by a summary of the theoretical and experimental tools used in this study.

### 2.1 Background of hot carrier solar cell

#### 2.1.1 Energy losses in photovoltaic energy conversion

The PV device converts the electromagnetic energy as a two-stage thermal engine. The first stage is light harvesting, where the incident radiation is absorbed by the active material and creates excited entities such as free electron-hole pairs. The second phase establishes the electrochemical potential inside the semiconductor accomplished by the relaxation of those photogenerated carriers [9].

Similar to the energy conversion in a thermal engine, the “cooling” is a necessary process to extract entropy free work between hot and cold thermal reservoirs but is also the stage at which additional massive energy losses can occur. In a conventional bulk semiconductor, photogenerated carriers dissipate their kinetic energy irreversibly through electron-phonon interactions and relax to the band edge within picoseconds after above-band-edge excitations [10]. Since much of the available energy is converted into lattice

heat, the cooling efficiency of hot carriers is far below the Carnot limit <sup>1</sup>. It is known as the intrinsic “above-bandgap” spectrum loss in a single junction solar cell. In addition, the radiation capture ability is restricted by the absorption bandgap of the active material, resulting in “below-bandgap” spectrum losses.

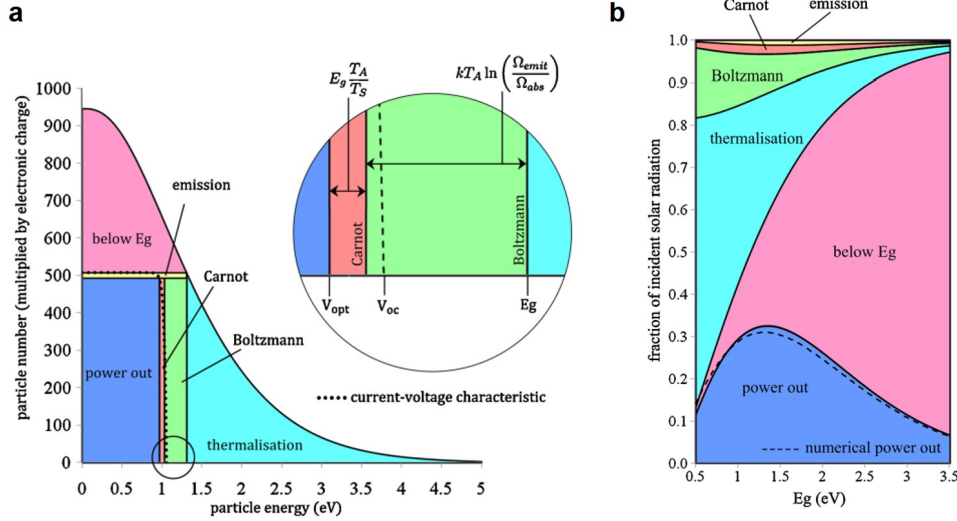


Figure 2.1: Energy losses during photovoltaic conversion. (a) Energy partition in a photovoltaic device with a bandgap of 1.31 eV shown in a pseudo voltage-current diagram. (b) Energy partition of energy losses in photovoltaic devices with bandgap. For cells at the optimum bandgap (1-1.5 eV), the thermalization contributes about 20% to 40% of energy loss [11].

Hirst et al. have made a comprehensive study to analyze the breakdown of energy losses in a PV device, as shown in Figure 2.1. Both the above- and below-bandgap mechanisms contribute about 30% of energy losses each in a single junction device with a bandgap about 1.5 eV, the following 30% of energy then correspond to the well-known single-junction limit of power conversion efficiency (PCE) in the one-sun condition [4].

### 2.1.2 Reducing thermalization losses by spectrum conversion

The method to obviate both the above- and below-bandgap spectrum losses aims for a monochromatic operation of the PV cell. The monochromatic operation denotes the case in which the frequency of excitation radiation matches the bandgap of the PV cell [9, 12]. It is the reason that spectrum conversion is so attractive to the photovoltaic community [13, 14].

The spectrum conversion refers to the technique of tuning the effective frequency of the incident radiation. Conventionally, frequency conversion is achieved using optoelec-

<sup>1</sup>The overall device efficiency is also limited by the light harvesting ability, like that indicated by the blackbody limit written as  $(1 - T_c^4/T_s^4)(1 - T_A/T_c)$ , where  $T_s$ ,  $T_c$ , and  $T_A$  is the temperature of the sun, converter(carrier), and ambient environment.

tronic effects of functional materials. These materials can emit luminescence at different frequencies compared to the absorbed spectrum accompanied by redistributions of radiative entities among their energy levels. Popular material families include rare-earth ions [15–18], transition metal ions [17, 19], and quantum nano-materials [15, 20–24].

Apart from the optical method above, specially designed electronic devices can also improve the spectrum utilization. Typical concepts are the well-known HCSC [6] and multiple exciton generation (MEG) [25] solar cells in third-generation photovoltaics, as shown in Figure 2.2. In these devices, energy re-distribution is realized via electronic scatterings of charge carriers without luminescence. Also, carriers will be extracted as electrical current directly through a narrow energy bandwidth to limit the creation of entropy [7]. The energy selection may not be apparent in the MEG solar cell since the newly created charge carriers have settled at the material’s band edge which can be extracted by the conventional metal contact normally. However, it still needs to block the direct output of hot carriers in principle to maximize the down-conversion yield.

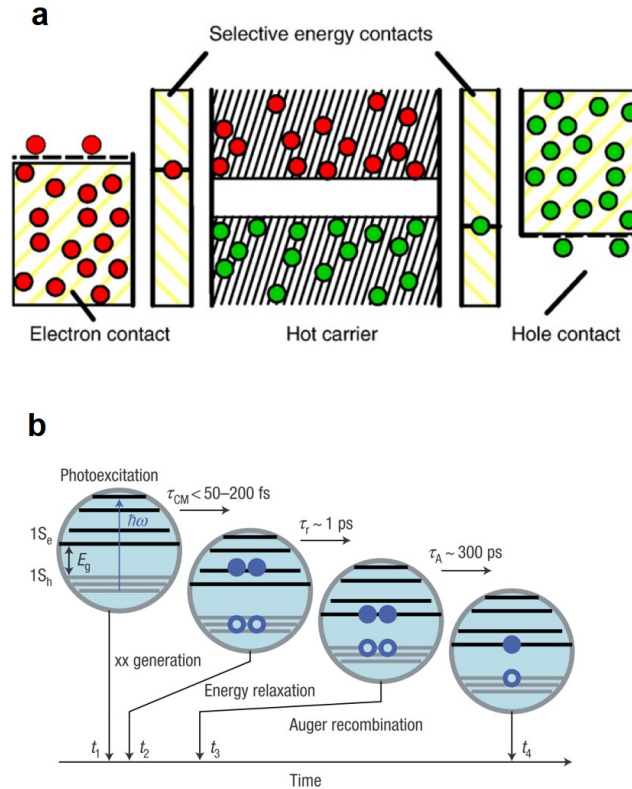


Figure 2.2: Schematic illustration of electronic spectrum conversions. (a) Hot carrier solar cell [26]; (b) MEG processes in nano-material [27].

### 2.1.3 Challenges in the hot carrier solar cell

The essential components of a HCSC are the hot carrier absorber (HCA) and energy selective contacts (ESC). The HCA has unique phononic properties and therefore can prolong the carrier cooling lifetime. Those hot carriers will then be extracted through the ESC by performing energy selection [7], where ideal carrier coolings can happen and a higher electrochemical potential will be established, as shown in Figure 2.2(a).

A great deal of theoretical modeling has been carried out for device performance by different groups [28–31]. Most of this modeling show encouraging conversion efficiencies by employing an ideal HCA and ESC. In recent years, more detailed physical processes have been considered in the modeling along with realistic material parameters, especially for the particle dynamics in HCA [32–34]. These more precise models require a much longer carrier cooling lifetime, which should be around nanoseconds at least. It also found that carrier refilling rate within the extraction window via carrier normalization will also affect the device current in practice [34, 35].

Exploring the suitable HCA material relies mainly on the theoretical modeling of phonon's properties. The density functional theory (DFT) plus perturbation treatment (also known as the DFPT) is a sophisticated and widely used approach to calculating the lattice vibration properties [36–39]. The phonon bottleneck effect was believed to prolong the carrier cooling lifetime [26]. In the traditional understanding, candidate materials should have a large phononic bandgap and narrow electronic bandgap [10]. It predicted that the large phononic bandgap could reduce the rate of hot-phonons' relaxation and so do the overall energy dissipation rate of the carrier-phonon system. Several materials were tested as HCA, such as InP [40], InN [41, 42], InGaAs/GaAsP quantum wells [43] and InGaN quantum wells [44] etc. The longest observed cooling time is around  $30 \sim 100$  ps in bulk materials.

Besides, nano-structured materials show a longer thermalization time due to the strong spatial confinement and energy discretization [45]. A cooling lifetime up to nanoseconds has been reported in quantum dots [46, 47]. However, the quantum/spatial confinement of these nano-materials restricts their electrical conductivity fundamentally, raising disadvantages in their electronic application. Most recently, significant hot phonon bottleneck effects were also reported in lead-halide perovskites. As a promising material in conventional PV devices, lead-halide perovskites exhibit evident power-dependent carrier cooling rates with a thermalization lifetime reaching to several hundred picoseconds [48], shown in

Figure 2.3(a). The likelihood of a reduced carrier-phonon coupling in this kind of materials due to polaron screening was also reported by Zhu et al. [49, 50]. Several mechanisms have been suggested for the hot carrier dynamics on sub-picoseconds after the excitation [50–52], however, a comprehensive understanding of the phonon bottleneck effect in these materials occurring on the subsequent timescales (up to thousand picoseconds) is still lacking.

On the other hand, the resonant tunneling diode (RTD) structure was used to act as the electronic ESC [53], where the resonant tunneling energy level provides energy selection of carrier transport. One of the successful experimental demonstration of ESC in recent was from Liao et al. [54] as shown in Figure 2.3(b), where a peak-to-valley current ratio of 8 and a full width at half maximum of 30 mV are realized using germanium nano-crystal at room temperature, known the best performance among RTDs based on annealed nano-crystals. However, due to the inelastic tunneling, non-zero recombination and the finite but a non-zero width of the extraction window, the ESC will suffer from severe energy losses in practice [55–57]. Electronic engineering of ESC is still challenging to date.

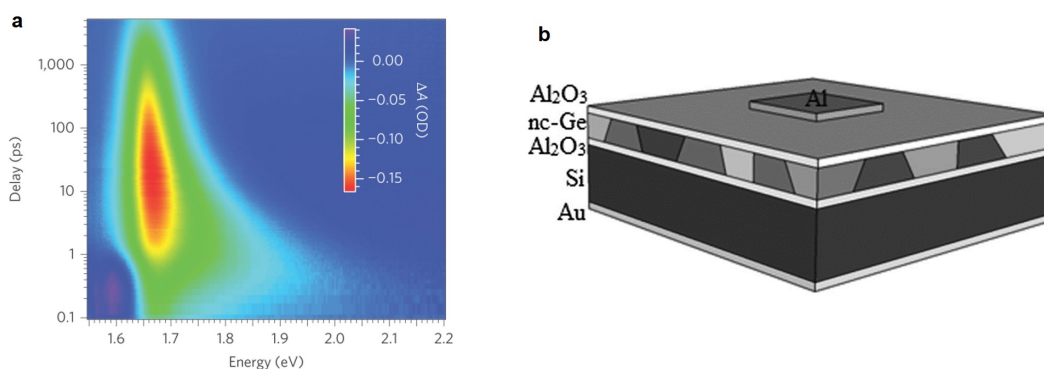


Figure 2.3: Recent progress in the study of hot carrier solar cells. (a) Hot carrier dynamics in lead-halide perovskites[48].; (b) Schematic of nano-crystal germanium resonant-tunneling-diode structures [54].

#### 2.1.4 The possibility of hot carrier extraction via optical coupling

Optical extraction of hot carriers was introduced in 2011 by Farrell et al. [8] as an alternative to electronic ESC, shown in Figure 2.4. In this original concept, the electronic ESC was replaced by an artificial photonic structure which transfers carrier hot-luminescence with a frequency selection. The luminescence is absorbed by another conventional single junction solar cell with a matched bandgap. The rapid hot carrier luminescence, efficient photon transfer, and quasi-monochromatic coupling were emphasized in this concept. In general, the optical energy selection, known as the OESC, would also be easier to fabricate

and control based on sophisticated photonic engineering techniques than their electronic counterpart. The first prediction gave a very encouraging result for the device performance by ignoring the thermalization losses in the hot carrier absorber.

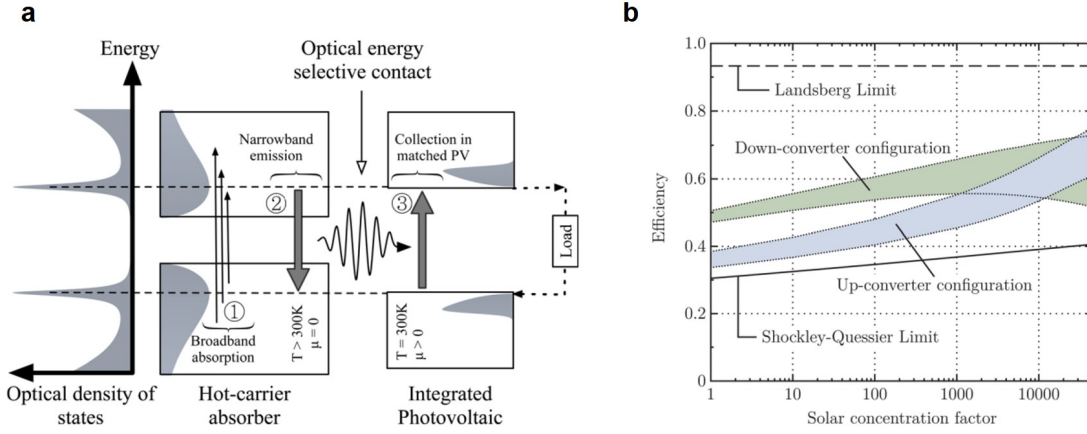


Figure 2.4: The prototype of the optical hot carrier solar cell [8]. (a) Schematic illustration of device concept and energy configurations; (b) Efficiency prediction of the optical hot carrier solar cell with an ideal hot carrier absorber.

In summary, the value of such an OESC concept include the following four topics: First, the OESC avoids electrical conduction which is more compatible with nano-structured hot carrier materials. These materials show a longer hot carrier lifetime but a poor electrical conductivity. The electrical isolation between the HCA and solar cell also allows a further electronic optimization for each part; Second, the OESC is suitable for both the conventional hot carrier (above band edge) and MEG (at the band edge) schemes by tuning the photon coupling energy. It therefore can act as a general carrier extraction method in spectrum management for photovoltaics; Third, the photovoltaic conversion of hot carriers occurs in a well-developed conventional solar cell in this device which ensures a high conversion efficiency; And fourth, energy selection from the optical spectrum is easier to achieve than its electronic counterpart based on state-of-art techniques because of the longer characteristic wavelength of photons.

However, comprehensive development of this prototype concept still lacks, especially in the quantitative analysis of luminescence coupling in a detailed device structure. Device design and working principles also need further exploration with more practical considerations. In particular, there is no specific instance of the photonic engineering to enhance the carrier hot-luminescence emission and enact frequency selection. The influence of hot carrier thermalization should also be examined carefully. Both aspects are essential to build a high-efficiency optical hot carrier solar cell (OHCSC) with OESC. These questions

will be investigated systematically in the following chapters of this thesis.

## 2.2 Photonic engineering of semiconductor luminescence

Fast luminescence emission is one of the critical requirement for the OESC approach. This section discusses the conventional implementation to modify the rate and yield of photon luminescence.

The property of optical emission is tunable by changing the local density of optical states (LDOS) of the medium, as was first identified by Purcell in 1946 [58]. The Purcell factor  $F_p$ , indicating the ratio of LDOS enlargement by a certain optical mode, is written as

$$F_p = \frac{3}{4\pi} \left( \frac{\lambda}{n_r} \right)^3 \frac{Q}{V_{\text{eff}}} \quad (2.1)$$

, where  $n_r$  is the relative refractive index of the active material,  $\lambda$  the resonant wavelength in free space,  $Q$  is the quality factor of the optical mode indicating its lifetime and bandwidth, and  $V_{\text{eff}}$  is the effective mode volume. The mode volume shows the degree of field confinement. For an ideal normal mode, mode volume is given as Eq (2.2)

$$V_{\text{eff}} = \frac{\int_V n_r^2 |\mathbf{E}|^2 d\mathbf{r}^3}{\max(n_r^2 |\mathbf{E}|^2)} \quad (2.2)$$

### 2.2.1 Fluorescence enhancement near metal nano-particles

The metal nano-particles are widely used as a near-field structure to enhance optical absorptions and emissions<sup>2</sup> because of the field enhancements around them.

When the fluorophores are in the proximity of a metal nano-particle, both absorption and emission enhancement can be observed where the metal particle acts as an optical antenna and facilitates the radiative coupling with free space [59]. The enlarged LDOS near metal particles also accelerates the radiative rate of fluorophores and increases their luminescence quantum yield in principle when competing with non-radiative decay channels [60]. However, metal also absorbs part of the optical energy, especially when the surface plasmon cannot couple to the far-field radiation efficiently [61]. Typically, this phenomenon is named as luminescence quenching of excited entities. Therefore, an optimal distance between the metal nanoparticle and fluorophore exists to maximize the

---

<sup>2</sup>it is the spontaneous emission in the fluorescence applications

far-field fluorescence enhancement [62].

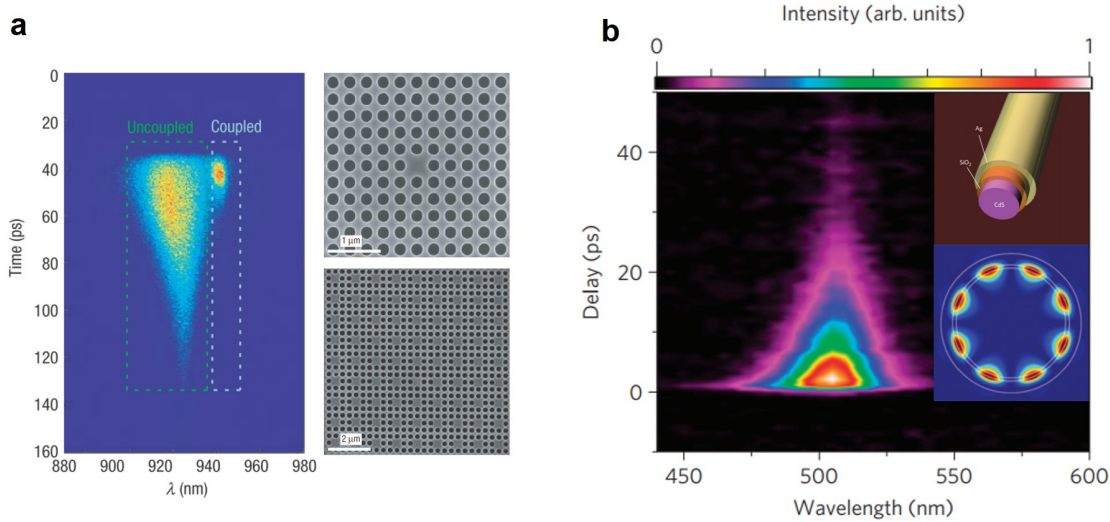


Figure 2.5: Purcell enhancements in nano-cavities show a faster transient time-resolve photoluminescence. (a) Square-type photonic crystal cavity [63]; (b) CdS-SiO<sub>2</sub>-Ag plasmonic core-shell nanowire[64].

## 2.2.2 Purcell effects in the nano-structure

Nano-cavity structures have been widely investigated in the field of quantum electrodynamics to modify the photon emission process. Since only a certain number of optical modes can be supported inside the cavity with finite bandwidths, LDOS can be enlarged evidently around the resonant frequencies so does the spontaneous emission rate of the coupled emitter inside [65].

The photonic crystal cavity is the typical structure that has been widely investigated in recent years, as shown in Figure 2.5(a). A two- or three-dimensional photonic crystal can be fabricated based on the E-beam lithography or self-assembled growth, where an artificial defect presents into a periodic array to form a local cavity [63, 66, 67]. As a result, defect states are introduced inside the photonic bandgap [68, 69]. The Purcell factor in such a cavity can reach several tens to hundreds of times. The primary challenge for the dielectric cavity is a lack of sufficient spatial confinement of the fields leading to a relatively large mode volume, even though its quality factor can be as large as several hundreds of thousands. Recently, Shugayev et al. achieved an emission enhancement factor of 2000 in a multilayer dielectric core-shell structure by using Mie resonance [70], which offers a new way to design high-enhancement-ratio dielectric cavity structure that do not require metals.

The surface plasmon polaritons (SPPs) have been investigated to provide stronger field

confinement in the nano-cavity. The standing wave modes of SPPs on metallic materials can be excited around the cavity structure, such as the quasi-two-dimensional metal disk sandwiched between dielectric layers [71] and the surface plasmonic whispering-gallery-mode (WGM) cavity [72]. The mode volume of SPPs can be 100 times smaller than that of the dielectric cavity, which is able to provide a Purcell factor over 1000 with a quality factor below than 50. The WGM of plasmonic core-shell nanowires also showed remarkable carrier hot-luminescence enhancements in recent [64, 73], as shown in Figure 2.5(b). Both direct and indirect bandgap semiconductors have been tested as the emitter, where the Purcell factor was reported to be about 1000 to 3000 times.

In addition to the cavity structure discussed above, the waveguide can also show a strong modulation on LDOS. One typical example is the slot waveguide which uses a low-refractive-index slot region in a waveguide to increase the local field intensity [74]. The waveguide design is adaptable to large-area implementation which is preferred for photovoltaics. However, the enhanced luminescence is coupled into the guided mode which propagates along a particular direction unless the cut-off condition is met. It raises a new challenge for efficient luminescence collection in the secondary solar cell. Besides, the enhancement factor of the guided modes would typically be smaller than that of cavity modes. For example in the slot waveguide the enhancement factor can be several tens to hundreds of times [75–77].

To simplify the analysis in this thesis without losing generality, the SPPs cavity will be considered first as an example in Chapter 5 to embody the OESC. It focuses on the development of the theoretical framework and exploration of the general working and design principles. Dielectric cavities and waveguides are considered as promising future work. Some initial results for the planar dielectric cavity are mentioned in Chapter 7.

### 2.2.3 Optical energy transformation via near-field coupling

After the luminescence emission from the spectrum converter, how to collect them again efficiently by a conventional solar cell is another challenge for the OESC concept.

In a conventional far-field configuration, the upper limit of radiation rate is constrained by the LDOS in the free-space known as the Stefan-Boltzmann limit [78]. When the interfaces of the photon emitter and receiver are close enough, photon tunneling can occur improving the energy transfer rate significantly [78–80]. It is a result of LDOS enhancement by utilizing the evanescent surface modes.

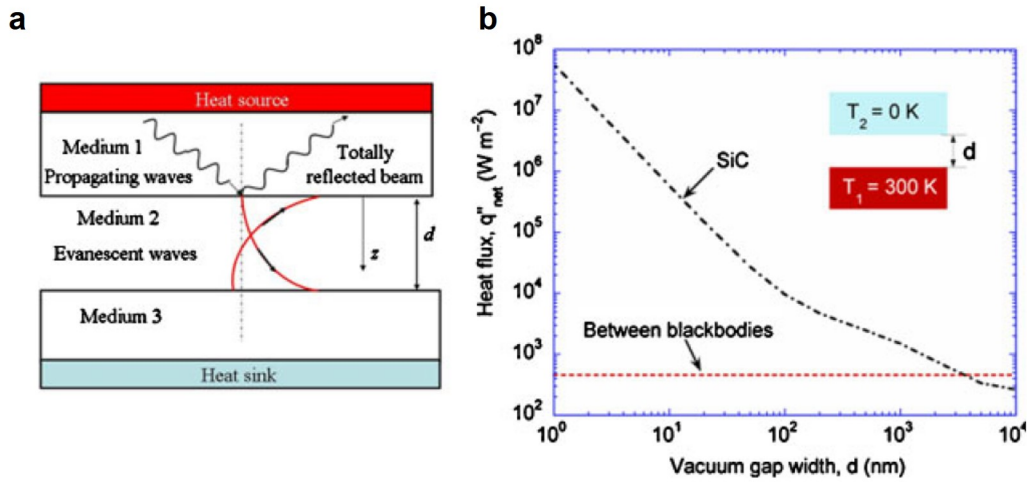


Figure 2.6: Radiative transfer in a near-field coupling. (a) Schematic illustration of the concept of evanescent waves and photon tunneling and (b) radiative heat transfer between two SiC plates maintained at 300 and 0 K. The energy transfer between two blackbodies has also been shown for reference [78].

One particular example of near-field coupling is using SPPs. By reversing the conventional design principles of SPPs waveguides [81], the semiconductor thin-film can absorb the SPPs directly with a relatively high efficiency. It has been widely used in the SPP-based light trapping structures for the ultra-thin solar cell [82–84]. Efficient absorptions of SPPs depends on two conditions. First, it requires an adequate absorption coefficient of the semiconductor absorber because of the relatively small penetration depth of SPPs into the active region [81]. Second, the dielectric constant of each component needs to be carefully chosen to further increase the field intensity of SPPs into the targeted components [84, 85].

## 2.3 Brief introduction to methodology

This section summarizes the general background of the methodologies for optical modeling and characterization employed in this thesis given in order of their appearance. More detail will be presented in each chapter and appendix.

### 2.3.1 Theoretical basis of spontaneous emission

Photon luminescence comes from the spontaneous emission, whose rate  $\gamma_{\text{spon}}$  of an excited quantum state is proportional to the LDOS as described by the well-known Fermi's Golden Rule [65]. For a simple two-level system, where the final electronic state is well defined, the transition rate is proportional to the final photonic density of state, shown as

$$\gamma_{\text{spon}} = \frac{2\omega}{3\hbar\epsilon_0} |\mathbf{p}|^2 \rho_{\text{ph}}(\mathbf{r}; \omega) \quad (2.3)$$

, where  $\hbar$  is the reduced Planck constant,  $\epsilon_0$  is the permittivity in vacuum, and  $|\mathbf{p}|^2$  is the intensity of dipole moment in the electric dipole approximation. The LDOS  $\rho_{\text{ph}}(\mathbf{r}; \omega)$  shows the available optical modal number at the place  $\mathbf{r}$  and frequency  $\omega$  in a particular photonic environment. In a three-dimensional free space with a background refractive index of  $n_{\text{B}}$ ,  $\rho_{\text{ph}}$  given as

$$\rho_{\text{ph}}(\omega) = \frac{\omega^2 n_{\text{B}}^3}{\pi^2 c^3} \quad (2.4)$$

A powerful theoretical tool to examine the LDOS analytically is the electromagnetic Green's function  $\mathbf{G}(\mathbf{r}, \mathbf{r}'; \omega)$  of the optical modes. It is understood as the correlation function between the triggered electromagnetic fields at position  $\mathbf{r}$  and the excitation source at position  $\mathbf{r}'$  [86–88]. Particularly, the local Green's function relates to the LDOS via the following equation [65, 89].

$$\rho_{\text{ph}}(\mathbf{r}, \omega) = \frac{6\omega}{\pi c^2} [\mathbf{n} \cdot \text{Im} \{ \mathbf{G}(\mathbf{r}, \mathbf{r}; \omega) \} \cdot \mathbf{n}] \quad (2.5)$$

Because of the essential role of the Green's function in photonic dynamics, Chapter 5 will use it to quantify the photon flux in the OESC. However, it is challenging to evaluate the Green's function correctly. In particular, the energy transfer problem in OHCS is non-Hermitian since the optical fields dissipate continually by either local absorptions or far-field emission. No normal modes exist in this circumstance, the classical mode expansion analysis [65] and Purcell's formula (Eq. (2.1)) [90, 91] fail as well. Instead, this thesis will use the numerical quasi-normal mode (QNM) method developed recently [92, 93] to calculate an accurate and self-consistent Green's function. More details about the electromagnetic Green's function and QNM will be given in Chapter 5 and Appendix A.

### 2.3.2 Numerical modeling using finite-difference time-domain method

Chapter 5 applies the finite-difference time-domain (FDTD) method to simulate the optical process numerically. The FDTD method models the electrodynamics in time-domain [94]. In contrast to the frequency-domain method in which only eigenmodes are often solved from the master Maxwell's equation, the FDTD method calculates the propagation of field across a finite-difference grid in space, named Yee's grid as shown in Figure 2.7.

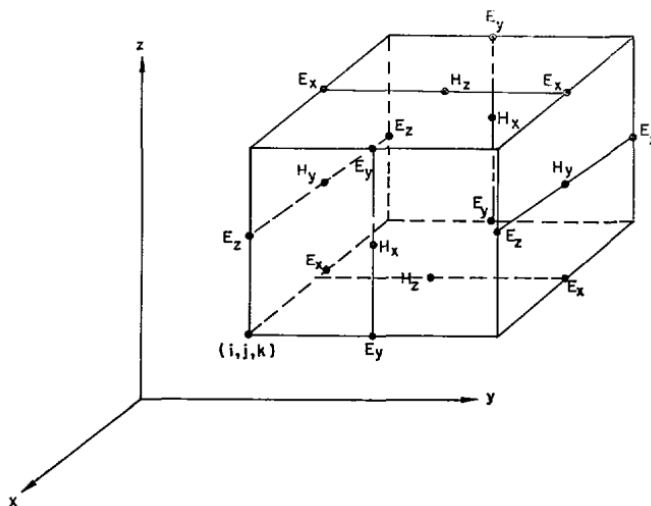


Figure 2.7: Schematic illustration of Yee's grid in FDTD method [94].

In this method, mutual-coupled electric and magnetic field vector components distribute at different locations in the Yee's cell in order to ease the numerical differentials with a second-order accuracy. The modeling starts with a field pulse injected by a source in the simulation domain. Typical sources include dipole and plane-wave types. Afterwards, the algorithm updates electric and magnetic fields on each grid point in a leapfrog manner according to Maxwell's equations with time-domain iterations. The iteration ends if desired transient or steady-state field behavior has been reached. The edges of the simulation domain will provide appropriate boundary conditions to model the out-going radiation and scatterings of the fields. Time variations of the field will be recorded which are then converted as the frequency-domain data for subsequent manipulation and analysis.

The FDTD method has a particular advantage in the research of local field enhancement. By monitoring the actual emission power  $P_{\text{FDTD}}$  from a dipole source in the simulation, the local Purcell factor can be examined simply as  $F_p|_{\text{FDTD}} = P_{\text{FDTD}}/P_0$  where  $P_0$  is the dipole power in a homogeneous environment [95]. Since the finite-difference grid introduces spatial average naturally, the FDTD method has excellent numerical stability and accuracy in the local field problem even in an absorbing medium in which the analytical formula of LDOS is divergent [96]. Therefore, the above method has been widely used in previous studies to verify the calculation of Purcell factor [90, 92, 93, 97, 98] and will also be employed in this thesis. All the FDTD simulations presented in this thesis are based on the commercial package *FDTD Solutions* from Lumerical Solutions Inc. [99].

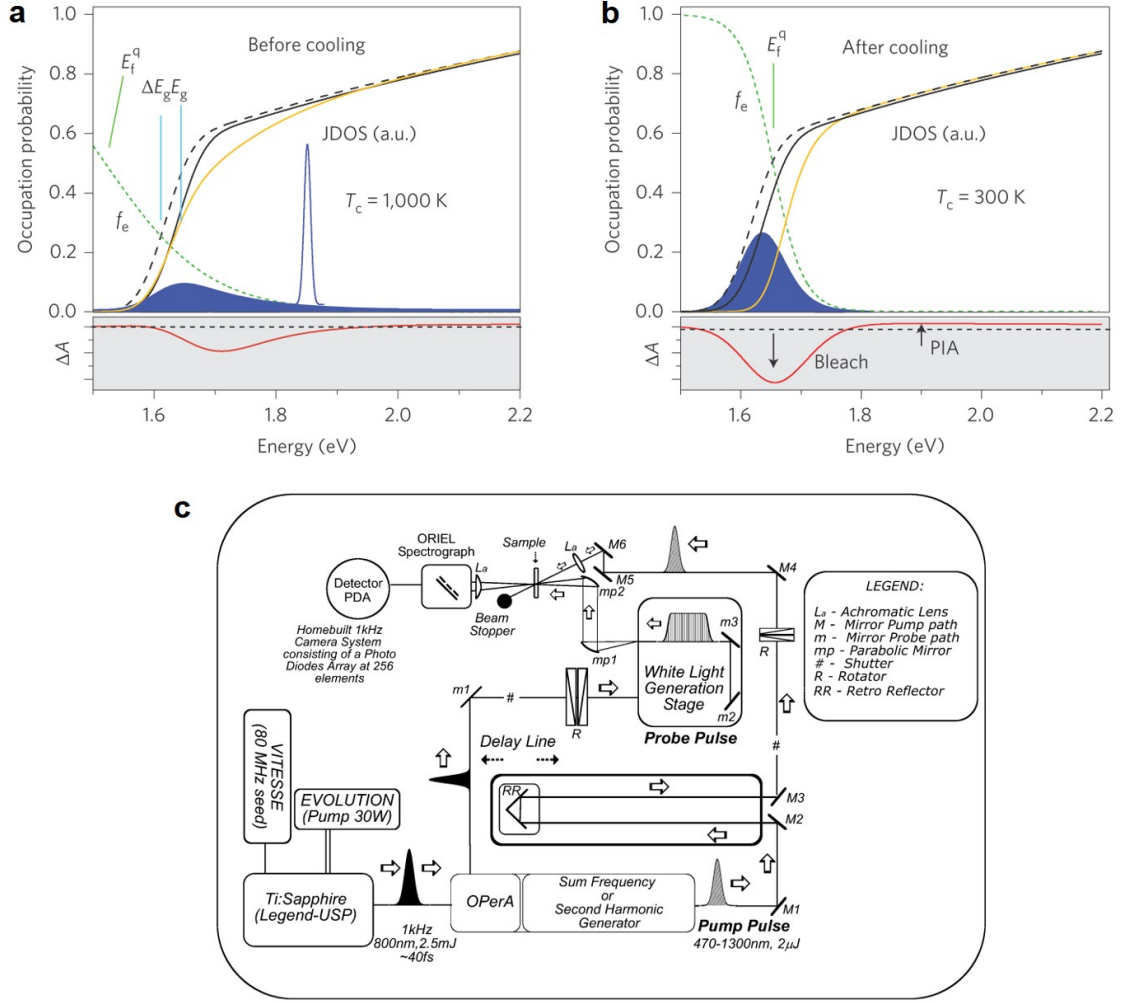


Figure 2.8: Carrier dynamics investigated by transient absorption spectroscopy. (a) Photo-excited carrier population in the semiconductor material before thermalization occurs; (b) Photo-excited carrier population after thermalization. The red curve in the bottom sub-panel shows the corresponding TA spectrum [48]. (c) Schematic representation of an experimental ultrafast transient absorption setup [100].

### 2.3.3 Hot carrier detection using ultrafast transient absorption

To explore new candidate materials with a long carrier thermalization lifetime, transient absorption (TA) was used to investigate the hot carrier dynamics in semiconductor materials as shown in Figure 2.8 [100, 101]. The essence of the TA technique relates to the state availability for optical transitions in the material. By comparing the time-dependent transmission spectrum  $T(\omega)$  of a probe beam to its background reference  $T_0(\omega)$  across the sample after an optical pump (pump-probe technique), the information of state occupation is visible via the real-time optical density at different frequencies  $\Delta OD(\omega, t) = \log(T_0(\omega)/T(\omega))$ , as shown in Figure 2.8(a)(b). Significant development has been carried out to estimate the transient carrier temperature, thermalization lifetime and effective phonon emission lifetime by analyzing the TA spectrum of the material, especially

in the study of HCSC [48, 102–105].

In the experimental aspect, Figure 2.8(c) illustrates a typical setup of TA spectrometer. In general, femtosecond laser pulses consist of a mode-locked oscillator (Ti:sapphire in Figure 2.8(c)) that seeded a regenerative amplifier. These seed pulses are then split into two sub-beams to trigger a frequency-tunable narrow-bandwidth pump beamline (using nonlinear optical crystal, such as BBO) and another white light continuum probe beamline (using a delay stage for example). Finally, the optical transmission of the probe beam after the sample is detected by a polychromatic-CCD at a series of time-delays  $t$  following the exposure of pump beam at  $t = 0$ .

This method is used in Chapter 6 to investigate the hot carrier dynamics in lead-halide perovskites.

## 2.4 Summary and conclusions

In this chapter, the background knowledge needed to understand this thesis has been summarized. The concepts and reasons for spectrum conversion in photovoltaics have been presented. The OHCSC connects the optical and electronic types of spectrum conversion. Further development of this concept can be beneficial in both areas.

## Chapter 3

# Global Understanding of Optical Hot Carrier Solar Cell

The general working principles of the optical hot carrier solar cell (OHCSC) is discussed in this chapter, which can be understood as an optically-integrated spectrum conversion system added on a conventional photovoltaic (PV) solar cell. Section 2 discusses the general condition to improve the energy efficiency for this type of device, where a net gain in the photocurrent for the same solar cell is recognized as the minimum requirement after applying spectrum converters. Section 3 presents the device performance with an optical energy selective contact to transfer the carrier hot-luminescence. Without loss of generality, the thermalization losses in the hot carrier absorber are ignored here whose impact will be fully addressed in the next chapter. The feedback electroluminescence from the PV cell shows a significant impact on the conversion yield of the hot carrier luminescence and therefore the output electrical power of the overall device. The photonic engineering methods used to enhance the luminescence transfer will also be discussed in section 4. Finally, section 5 addresses the thermodynamic limit in spectrum conversion of the non-equilibrium steady state.

### **3.1 Introduction of optical hot carrier solar cell: in a perspective of spectrum conversion**

The OHCSC uses the carrier hot-luminescence to drive a conventional frequency-matched PV cell through an optical energy selective contact (OESC) [8] (see Figure 2.4). In this concept, the semiconductor hot carrier absorber (HCA) works as a spectrum up/down

converter which realizes energy redistribution and spectrum conversion by electronic scatterings of charge carriers, such as using the Auger-recombination/Impact-ionization (AI) process. It then results in “photon fusion” (Auger, up-conversion) and “photon splitting”(impact ionization, down-conversion) subsequently in the carrier luminescence via radiative recombination.

It is worth noting that spectrum conversions often require long hot carrier lifetimes. In the up-conversion, the Auger-excited high energy carrier needs to be extracted before its non-radiative intraband relaxation. Similarly, a photogenerated hot carrier has to perform a faster impact ionization to avoid thermalization losses. In fact, the hot carrier understanding is also applicable to the spectrum up/down conversion from a thermodynamic point of view. The non-radiative relaxation of high energy dipoles, or high energy intermediate transition states in general, needs to be suppressed as well in the latter, leading to a “hot” (broadband) distribution of excited entities in a thermal-equilibrium (open-circuit) state. This principle is also valid for the down-conversion (quantum-cutting effect [17, 21, 106]) and multiple exciton generation (MEG) [27, 107, 108]. The unique feature of these cases is that carriers/photons are extracted on a lower energy level so that the electrochemical equilibrium of the system shifts toward particle multiplication in a steady state. Therefore, the carrier hot-luminescence phenomenon can be understood thermodynamically as a general spectrum up/down conversions. The study outcomes of OHCS can also be used in the general optically-integrated spectrum conversion system.

There are three further considerations:

First, the above consideration addresses the similarities between the hot carrier and up/down conversions only in steady state thermodynamics, rather than indicating that hot carriers are the required physical mechanism in both cases. It emphasizes the value of comparing them to each other in research methodologies and outcomes especially for the OHCS. For example, virtual transitions that are usually involved in the up/down conversion is a different mechanism to that in conventional hot carrier dynamics. However, no essential difference exists in their thermodynamic descriptions when in an equilibrium steady state, where the Bose-Einstein statistics can apply to both cases to characterize broadband carrier pairs or photons. Such a description has widely been used in previous analyses [8, 13, 29, 109–111]. Even in a non-equilibrium steady state, the difference in their transient mechanism may vary the final distribution functions in general, however, their steady state operations still have similar properties.

Second, it is noted that researchers analyze the up/down-conversion process by assign-

ing an ambient temperature to the dipole population usually on all energy levels, such as 300 K, to distinguish from the conventional hot carrier dynamics. However, it must be accompanied with non-uniform chemical potentials among these levels at the same time to enable the spectrum conversion [13, 14, 112], which still corresponds to a “hot” (broader) carrier population eventually. In fact, there is an arbitrary assignment of the chemical potential and ensemble-averaged temperature to describe the same carrier occupation probability on each energy level in thermodynamics, at least in the mathematical description [113].

Third, conventional up/down-converters have discrete energy levels typically and therefore step-like conversion yield respect to the photon energy. Instead, continuous band structure and output spectrum usually exist in the hot carrier scenario [8, 29, 34], where carrier up/down transitions can occur at the same time and multiple-carrier scattering is allowed in principle. Such a continuous conversion has already been observed in the MEG process [107, 114]. It will not cause essential thermodynamic differences of the OHCS to the general spectrum conversion systems.

Apart from the above considerations, the OHCS also emphasizes the strong optical enhancement with a narrow bandwidth energy selection to conduct the carrier luminescence, which is known as the OESC. The optical enhancement increases the photon transfer rate and therefore improve the yield of the carrier hot-luminescence; on the other hand, energy selection by photonic engineering is necessary to reduce the carrier thermalization losses in the secondary PV cell with a matched bandgap. It is noted that such an energy selection can be imposed by the discrete optoelectronic energy levels in a spectrum converter usually. With a deep photonic engineering, the OESC introduces a significant mutual coupling between the hot carrier absorber (spectrum converter) and the PV cell. It leads to a series of unique device operating characteristics which will be discussed in the following thesis.

### 3.2 A practical condition in efficiency enhancement

With the general understanding of the OHCS and spectrum conversion above, this section will discuss the requirements to achieve efficiency improvement in a practical situation. Different to the limit efficiency widely being discussed in previous studies, this section addresses the general efficiency enhancement condition with a fixed solar cell (same bandgap) when adding an extra spectrum converters.

Throughout the thesis, a traditional semiconductor solar cell based on an ideal charge separation mechanism is considered, referred to as the PV cell or PV component hereafter. The electrical properties of the cell follow the standard Shockley-Queisser formula [115] with an ideality factor of 1 and without any parasitic resistances. Only radiative recombination occurs which is estimated by the generalized Planck equation [9, 13] at room temperature  $T_{\text{rt}} = 300$  K and chemical potential  $qV$ , where  $q$  is the elemental charge and  $V$  is the bias voltage. Also, without losing generality, the hot carrier absorber only has a single continuous energy band, which supports a hot carrier population with a temperature  $T_c > 300$  K inside. The physical temperature, or lattice temperature, of the hot carrier absorber (spectrum converter) is always at 300 K. The radiation energy  $\dot{Q}(X, T, \mu)$  and photon flux  $\dot{N}(X, T, \mu)$  for both the converter and PV cell in an equilibrium state are given as [9, 13].

$$\begin{cases} \dot{N}(X, T, \mu) = \frac{1}{4\pi^3 \hbar^3 c^2} \int_0^\infty X(\omega) \hbar^2 \omega^2 \left[ \exp\left(\frac{\hbar\omega - \mu}{k_B T}\right) - 1 \right]^{-1} d\hbar\omega \\ \dot{Q}(X, T, \mu) = \frac{1}{4\pi^3 \hbar^3 c^2} \int_0^\infty X(\omega) \hbar^3 \omega^3 \left[ \exp\left(\frac{\hbar\omega - \mu}{k_B T}\right) - 1 \right]^{-1} d\hbar\omega \end{cases} \quad (3.1)$$

Here  $T$  is the ensemble-averaged temperature of the excited entities while  $\mu$  is their chemical potential,  $\hbar$  is the reduced Planck constant,  $c$  is the speed of light in vacuum,  $k_B$  is the Boltzmann's constant,  $\omega$  is optical frequency. Since the generalized optical étendue  $X(\omega) = \Omega \cdot a(\omega)$  combines both the optical étendue  $\Omega$  and frequency dependent absorptivity/emissivity  $a(\omega)$  (between 0 and 1), the integral over frequency is always from zero to infinity.

Figure 3.1 shows the general energy flows, specific instances of the planar-tandem architecture, and the definitions of up/down conversion configuration of the OHCSC [8]. All the energy flows are labeled in the form of “emitter-receiver” in the subscript, where the sun, free-space, PV cell and converter are abbreviated as “s”, “f”, “p” and “c” respectively<sup>1</sup>. The total input power from the sun  $\dot{Q}_s(R_c f_s, T_{\text{sun}}, 0)$  has a blackbody spectrum with  $T_s = 5760$  K and chemical potential of zero.  $R_c$  is the optical concentration factor and  $f_s = 6.8 \times 10^{-5}$  is the solid angle factor for the sun observed on the Earth's surface [115]. Part of  $\dot{Q}_s$  is absorbed by the PV cell directly while the converter capture other parts. This process can be characterized by the absorptance  $a_p(\omega)$  of the PV cell and  $a_c(\omega)$  of the converter, respectively.

Here, we consider the following five energy channels of the spectrum converter:

---

<sup>1</sup>For example,  $\dot{Q}_{s-c}$  means the transferred power flux from the sun to the converter.

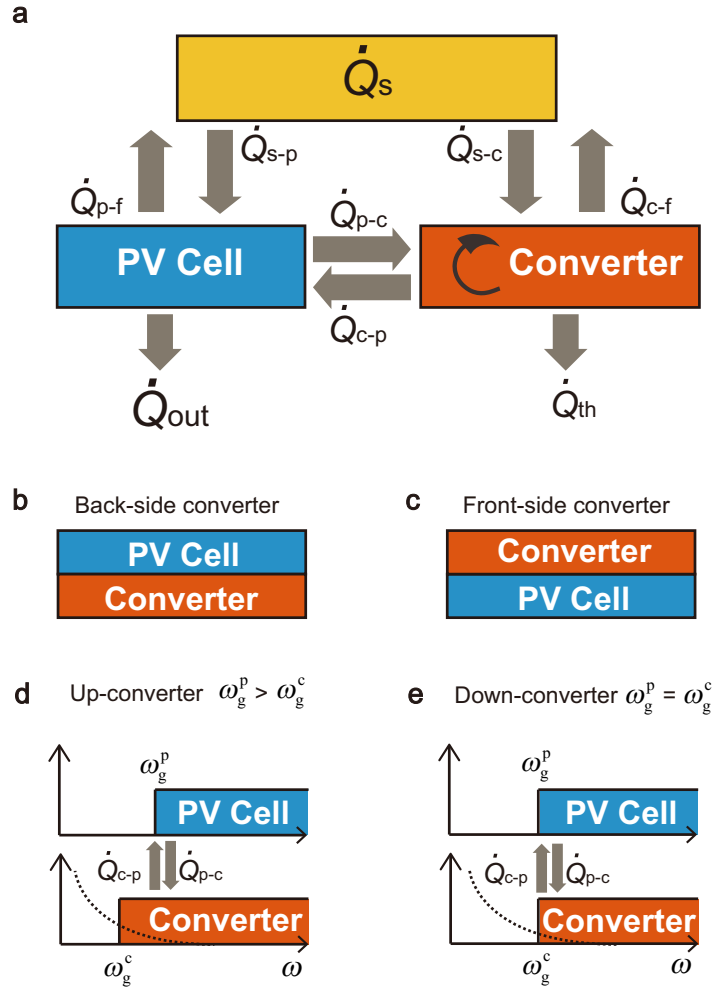


Figure 3.1: Schematic demonstration of a general spectrum conversion system. (a) General energy flow diagram of an OHCS and also of a spectrum up/down conversion system; (b) and (c) Planar-tandem realization of the back-side and front-side converter, respectively; (d) and (e) Definitions of the up- and down-conversion configuration of the OHCS respect to the photon frequency  $\omega$ . The blue block denotes the PV cell's energy band above its bandgap  $\omega_g^p$  while the orange one is for the converter above the bandgap  $\omega_g^c$ . According to Ref. [8], the up-converter has a smaller bandgap than that of the PV cell while the down-converter always has the same one. The dotted lines overlaid on the converter's energy bands denote the distribution probability of radiative dipoles inside which quickly decreases at a higher energy.

1. Incident light from the sun  $\dot{Q}_{s-c}(R_c f_s a_c, T_s, 0)$ ;
2. Luminescence emission to the free-space  $\dot{Q}_{c-f}(\Omega_c a_c, T_c, \mu_c)$  ;
3. Luminescence absorption from the PV cell  $\dot{Q}_{p-c}(X, T_{rt}, qV)$ ;
4. Luminescence emission to the PV cell  $\dot{Q}_{c-p}(X, T_c, \mu_c)$ ;
5. Non-radiative relaxation of excited entities, such as thermalization  $\dot{Q}_{th}$ .

Particular optical étendue  $\Omega_c$  and absorptivity  $a_c$  of the converter are considered in  $\dot{Q}_{c-f}$  which could be different to their intrinsic values <sup>2</sup> ( $\Omega_c^0, a_c^0$ ) due to the optical influences from the PV cell. The mutual coupling factor  $X$  in fluxes  $\dot{Q}_{p-c}$  and  $\dot{Q}_{c-p}$  can, therefore,

<sup>2</sup>when the converter stand alone

be represented as  $X = a_p^0 a_c^0 \Omega$  in general, where all the effects from photonic engineering are included in the same optical étendue  $\Omega$  from both sides. Importantly,  $\dot{Q}_{p-c}$  and  $\dot{Q}_{c-p}$  only occur around the bandgap of the PV cell with a narrow bandwidth, as shown in Figure 3.1(d) and (e). The working state of the converter and the yield of the luminescence are then determined by the energy conservation equation Eq. (3.2) in a steady state [8].

$$\begin{aligned} \dot{Q}_{s-c}(R_c f_s a_c, T_s, 0) + \dot{Q}_{p-c}(X, T_{rt}, 0) \\ - \dot{Q}_{c-f}(\Omega_c a_c, T_c, \mu_c) - \dot{Q}_{c-p}(X, T_c, \mu_c) - \dot{Q}_{th} = 0 \end{aligned} \quad (3.2)$$

In order to determine the conditions for increasing the overall power conversion efficiency (PCE), it is necessary to emphasize again that the PV cell works conventionally here at its intrinsic bandgap with the radiative recombination loss  $\dot{Q}_{p-f}$  as labeled in Figure 3.1(a). Due to an invariant total input power from the sun  $\dot{Q}_s(R_c f_s, T_s, 0)$ , a higher PCE  $\eta = \dot{Q}_{out}/\dot{Q}_s$  means a larger output electrical power  $\dot{Q}_{out}$  from the PV cell. It must come from a larger input photocurrent or a smaller recombination loss of the cell. Eq. (3.3) and Eq. (3.4) list the short-circuit current density  $J_{sc}$  and dark saturation current density  $J_0$  of the cell before and after applying the spectrum converter, please note the difference in the absorptivity used in these equations.

$$\left\{ \begin{array}{l} J_{sc} = q \left[ \dot{N}_{c-p}(X, T_c, \mu_c) + \dot{N}_{s-p}(R_c f_s a_p, T_s, 0) - \dot{N}_{p-f}(R_c f_s a_p, T_{rt}, 0) - \dot{N}_{p-c}(X, T_{rt}, 0) \right] \\ \quad \approx q \left[ \dot{N}_{s-p}(R_c f_s a_p, T_s, 0) + \dot{N}_{c-p}(X, T_c, \mu_c) \right] \quad ; \text{ with the converter} \\ J_{sc}' = q \left[ \dot{N}_{s-p}(R_c f_s a_p^0, T_s, 0) - \dot{N}_{p-f}(R_c f_s a_p^0, T_{rt}, 0) \right] \\ \quad \approx q \left[ \dot{N}_{s-p}(R_c f_s a_p^0, T_s, 0) \right] \quad ; \text{ w/o the converter} \end{array} \right. \quad (3.3)$$

$$\left\{ \begin{array}{l} J_0 = q \left[ \dot{N}_{p-f}(\Omega_p a_p, T_{rt}, 0) + \dot{N}_{p-c}(X, T_{rt}, 0) \right] \quad ; \text{ with the converter} \\ J_0' = q \left[ \dot{N}_{p-f}(\Omega_p a_p^0, T_{rt}, 0) \right] \quad ; \text{ w/o the converter} \end{array} \right. \quad (3.4)$$

Since an effective optical coupling between the cell and converter is imposed by the OESC, typically the flux  $\dot{N}_{p-c}(X, T_{rt}, 0)$ , that is the recombination luminescence from the cell to the converter, will be a nontrivial number in Eq. (3.4) above. Therefore, it is reasonable to predict a similar or even larger  $J_0$  when the converter presents nearby, although the emissivity  $a_p$  and  $a_p^0$  may be different in both cases. Then, a preliminary condition of PCE improvement for an OHCS should be a larger short-circuit current of

the cell.

$$J_{sc} > J_{sc}' \quad (3.5)$$

Further discussion of Eq. (3.5) follows: First, this condition is defined at the short-circuit condition ( $V = 0$ ) of the solar cell rather than the open-circuit condition usually used in the thermal-equilibrium analysis, like that of Ruppel and Würfel's method [111, 116] to predict the limit efficiency of the device. It is the minimum necessary criteria to have a better device performance; therefore it is more instructive in a practical device design. Second, this condition could be applied to all the spectrum conversion systems and in both the up/down-conversion configurations in Figure 3.1, since it is derived from the general operating principle of a conventional solar cell. This condition also implies the importance and necessity of photon management in an optically-integrated spectrum conversion system. Of course, as identified by Eq. (3.4), the dark saturation current of the cell may also increase significantly by the OESC, therefore Eq. (3.5) is a necessary but not sufficient condition to ensure a larger PCE. The detailed variations of the output voltage and overall efficiency will be discussed later.

### 3.3 Photonic engineering in spectrum conversion system

The significance of photonic engineering in a spectrum conversion system will be examined in this section. It will show that in some cases the photonic enhancement is the only method to satisfy Eq. (3.5) which also allows a more flexible design of the spectrum conversion system in other situations.

Photon management in the spectrum conversion has been addressed before by Trupke et al. [13], where high index materials were suggested to prevent the luminescence escaping to the outer space. With the recent progress in nano-optics, photonic engineering could further benefit the spectrum conversion system in the following aspects: 1) increasing the transfer rate of optical energy; 2) increasing the internal quantum yield of the spectrum conversion; 3) enforcing a quasi-monochromatic coupling of the luminescence at the desired energy level.

The first benefit above comes from increased emissivity and absorptivity of both the luminescent converter and the PV cell respectively, which typically relates to the enhancement of electromagnetic fields in the structures. The second aspect refers to the fact

that multiple carrier transitions happen simultaneously in the converter, the luminescence yield is therefore determined by the radiation rate of excited entities compared to other non-radiative processes [59, 117–119]. In the OHCS, the dominate non-radiative loss mechanism is carrier thermalizations occurring in several hundred to thousand picoseconds typically. Optical energy selection relies on the photonic resonance. In the perspective of Eq. (3.5), a monochromatic coupling close to the band edge of the PV cell allows the maximum photon multiplication in an ideal case. It therefore results in the maximum photocurrent increase in principle since the photon transfer occurs at the lowest available energy.

A series of numerical examples are given below to illustrate the influence of photonic engineering in the OHCS. For simplicity, a planar geometry of both the PV cell and hot carrier spectrum converter are used here with a maximum optical étendue of  $\pi$  into a hemisphere as shown in Figure 3.1(b) and (c).

The device performance is estimated using the standard detailed-balance model in the following discussions. Only the thermal equilibrium state under a 1-sun condition,  $R_c = 1$ , is considered here unless otherwise specified. The yield of carrier hot-luminescence is determined by solving the hot carrier temperature  $T_c$  from the energy conservation equation Eq. (3.2), where the non-radiative spectrum losses or the thermalization of hot carriers is ignored ( $\dot{Q}_{th} = 0$ ). A zero chemical potential is always kept inside the converter, which corresponds to an ultrafast AI process occurring in a semiconductor material and maximizes the freedom of carrier conversions [7, 8]. Section 5 will show that this assumption is also compatible to the thermodynamic directionality to drive a spontaneous spectrum conversion.

The intrinsic absorptivity  $a_{p/c}^0(\omega)$  of both the PV cell and spectrum converter have a Heaviside step-like profile below and above their bandgap frequencies  $\omega_g^p$  and  $\omega_g^c$  respectively, as shown in Figure 3.1(d) and (e). The uniform above-bandgap absorptance has a value of 1 or 0.5 in these components, representing an ideally full absorption and a semi-transparent device respectively. The semi-transparent situation is much common in practice, especially in a nano-structured device.

For the photon fluxes associated with the external environment, the actual absorption and emission of the two components may be affected by the optical couplings with each other. One of the typical examples is the mutual shading in a thick tandem structure. Without losing generality, here use the shading effect to simulate the incident energy partition between the PV cell and spectrum converter. In the back-side converter as

shown in Figure 3.1(b),  $a_p = a_p^0$ ,  $a_c = (1 - a_p^0)a_c^0$ . Instead,  $a_p = (1 - a_c^0)a_p^0$ ,  $a_c = a_c^0$  for the front-side converter in Figure 3.1(c). All detailed optical interferences and surface reflections are ignored here. Also, no far-field radiation leaves from the back-side of the device either emitted by the PV cell or by the spectrum converter. These assumptions will not affect the general discussion below.

The mutual photon fluxes between the PV cell and spectrum converter is modified by some artificial photonic effects given as  $\dot{N}(X = \pi a_p^0 a_c^0 F_0, T, \mu)$ , where  $F_0$  is a general optical enhancement factor. The frequency of transferred luminescence is around the bandgap energy (frequency) of the PV cell  $\omega_g^p$  with a bandwidth assumed to be  $\Delta\omega = \omega_g^p/30$ . The coefficient 30 here corresponds to the lifetime and resonant intensity of the optical mode, known as the quality factor  $Q$ , whose value is accessible by common photonic structures without difficulty [63, 64, 67, 73]. A rectangular profile on  $F_0(\omega)$ , and therefore on the mutual photon flux  $\dot{N}_{c-p}$  and  $\dot{N}_{p-c}(\omega)$  (labeled in Figure 3.1), is assumed whose value is larger than one only when between  $\omega_g^p \sim \omega_g^p + \Delta\omega$ .

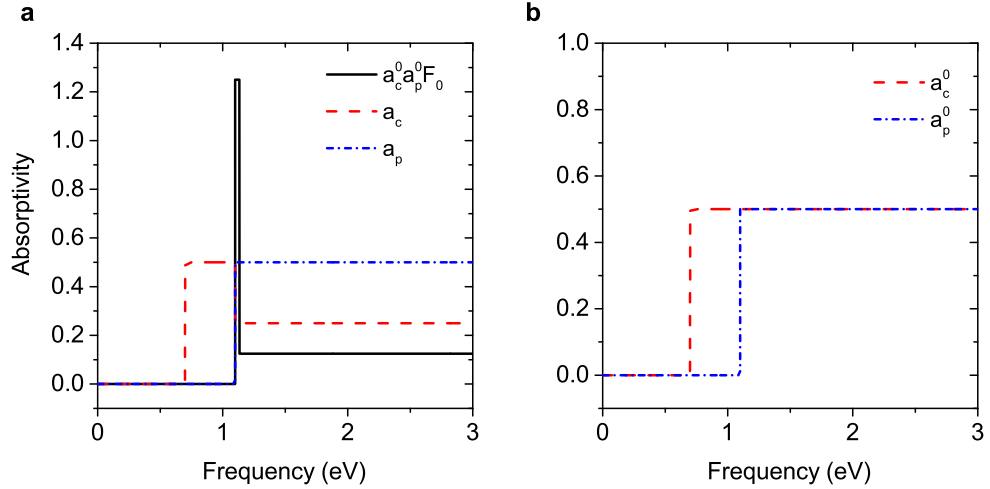


Figure 3.2: An example of a back-side up-converter device with optical enhancement. The bandgaps of the converter  $\omega_g^c$  and PV cell  $\omega_g^p$  are 0.7 eV and 1.1 eV respectively. The intrinsic above-bandgap absorptance of both components is 0.5 with a step-like profile as shown in (b), while the actual absorptance of the far-field incident light will also be affected by the mutual shading between different components as shown in (a). Five times optical enhancement  $F_0$  is applied near the  $\omega_g^p$  with a bandwidth of  $\omega_g^p/30$  to modify the luminescence transfer between the PV cell and spectrum converter.

Figure 3.2 shows an optical configuration as a representative demonstration for the above parameters. In this example, the bandgap of the PV cell and converter are  $\omega_g^p=1.1$  eV and  $\omega_g^c=0.7$  eV, respectively; the intrinsic absorptance of both components are 0.5 above their bandgaps. When placing the converter at the back-side of the PV cell, the actual absorptance and also emissivity of the converter is 0.25 when  $\omega > \omega_g^p$  while is still 0.5 when  $\omega_g^c < \omega < \omega_g^p$ . The optical enhancement ratio  $F_0$  is five within the coupling window

$$\omega_g^p \sim \omega_g^p + \Delta\omega.$$

With the above optical configuration, the gain ratio of short-circuit current density  $g_J$  defined as  $J_{sc}/J_{sc}'$  will then be examined first under different optical enhancement ratios. The impact on the open-circuit voltage  $g_V = V_{oc}/V_{oc}'$  and the overall behavior of the PCE  $g_\eta = \eta/\eta'$  will also be discussed in turn. All the reference variables here with a prime sign denote those from the PV cell when it works alone with the intrinsic absorptance  $a_p^0(\omega)$  to the incident sunlight.

### 3.3.1 Photocurrent gain via optical energy selective contact

Figure 3.3 and Figure 3.4 show the gain ratio of short-circuit current density  $g_J$  in both an up- and down-conversion systems with different configurations. In the up-conversion case, the bandgap of the PV cell is fixed at  $\omega_g^p = 1.1$  eV while the bandgap of converter varies in  $\omega_g^c \in [0.5 \text{ eV}, 1.1 \text{ eV}]$ . In contrast, both of the two bandgap energies varies simultaneously  $\omega_g^p = \omega_g^c \in [0.5 \text{ eV}, 1.1 \text{ eV}]$  in the down-conversion. The energy 1.1 eV chosen here refers to the popular bandgaps in photovoltaics, such as that of the monocrystalline silicon. The optical enhancement ratio within the selection window is  $F_0 \in [1, 5000]$ . The same color bar is used in both of Figure 3.3 and Figure 3.4 to show a global comparison in different scenarios.

In principle, the up-conversion configuration allows both the front-side and back-side converters due to a lower bandgap energy of the converter as shown in Figure 3.1. Since the back-side converter works more like an additional contributor to the PV cell without introducing shading losses, it can always provide a net current gain ( $g_J > 1$ ) for the cell as shown in Figure 3.3(a) and (b). Instead, a front-side converter may reduce the overall photon currents ( $g_J < 1$ ) in three possible ways if no adequate optical enhancement presents in Figure 3.3(c) and (d): 1) reducing the direct absorption of the PV cell to sunlight (shading effect); 2) emission back to the air from the front-side surface (reciprocal effect); 3) mismatch of the emission/reabsorption profiles between the converter and PV cell due to  $\omega_g^p \neq \omega_g^c$  (escape effect). For example, on the point  $(\omega_c, F) = (0.5, 1)$  in Figure 3.3(c),  $g_J \approx 9 \times 10^{-4}$  with  $\dot{N}_{c-f}/\dot{N}_{c-p}$  equals about 4333, meaning almost all the hot-luminescence is emitted from the top front surface and hence back to the free-space (via  $\dot{N}_{c-f}$  in Figure 3.1(a)).

The luminescence flux  $\dot{N}_{c-p}$  to the cell is a product of the transfer velocity and spatial density of photons around the extraction energy level  $\omega_g^p$ . A higher photon current gain is

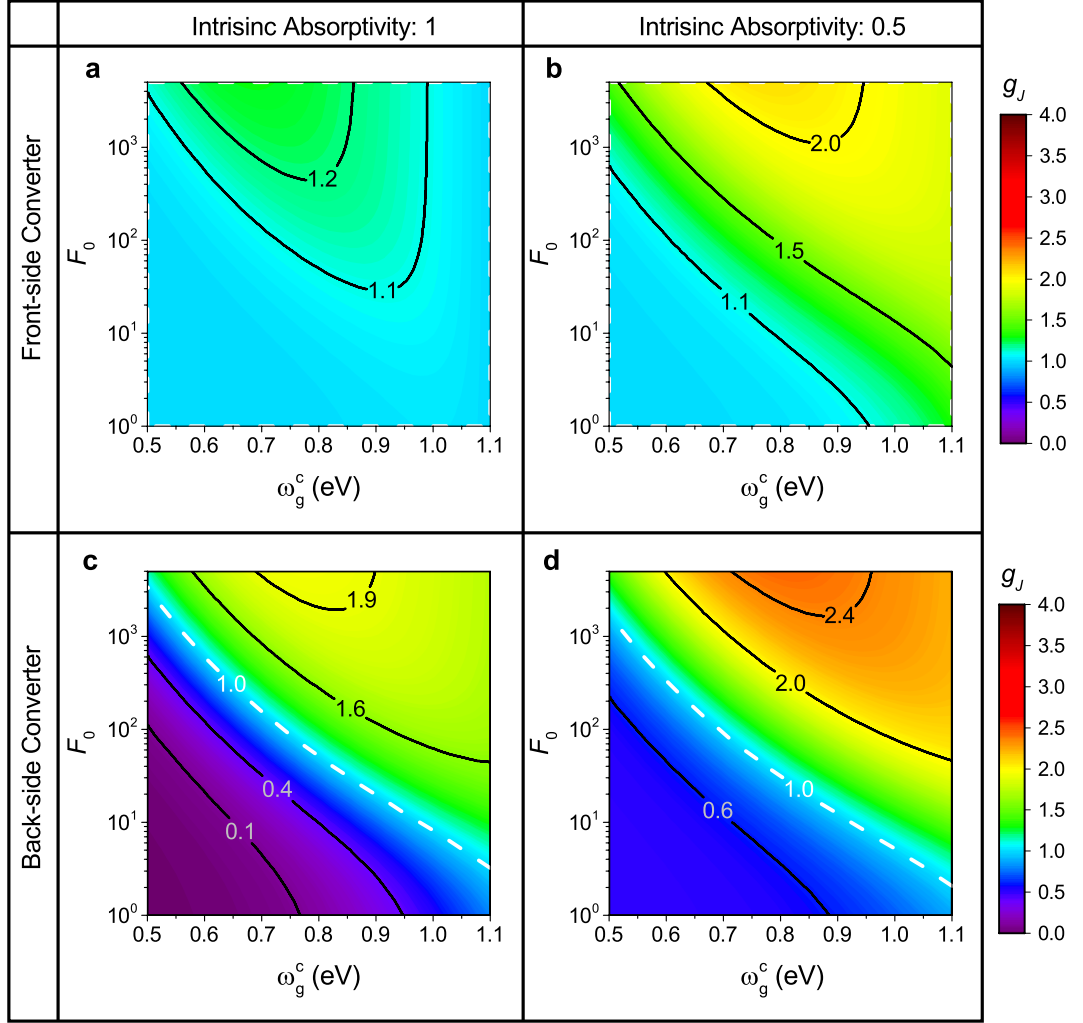


Figure 3.3: The gain ratio of short-circuit current density in the up-conversion configuration. (a) and (b) back-side up-converter with intrinsic above-bandgap absorptivities of both components equal to 1 and 0.5, respectively; (c) and (d) front-side up-converter with intrinsic above-bandgap absorptivities of both components equal to 1 and 0.5, respectively

always available by increasing the optical enhancement factor  $F_0$  according to Figure 3.3, which elevates the transfer rate of a single photon. On the other hand, a smaller energy difference of  $\omega_g^p - \omega_g^c$  will enlarge the up-conversion yield of hot-luminescence around  $\omega_g^p$  considering a Bose-Einstein's distribution of radiative dipoles exists above  $\omega_g^c$  in the converter.

However, a larger  $\omega_g^c$  will reduce the available solar spectrum to the converter  $\dot{Q}_{s-c}$  and therefore the ensemble-averaged carrier temperature  $T_c$  according to Eq. (3.2). It leads to a lower yield of carrier hot-luminescence at  $\omega_g^p$ . The divergence in the total excitation power also explains the lowest achievable maximum  $g_J$  shown in Figure 3.3(a) compared to other cases, since  $\dot{Q}_{s-c}$  is non-zero only when  $\omega \in [\omega_g^c, 1.1 \text{ eV})$  in that configuration. It strongly limits the hot carrier temperature and the dipole occupations at higher energy

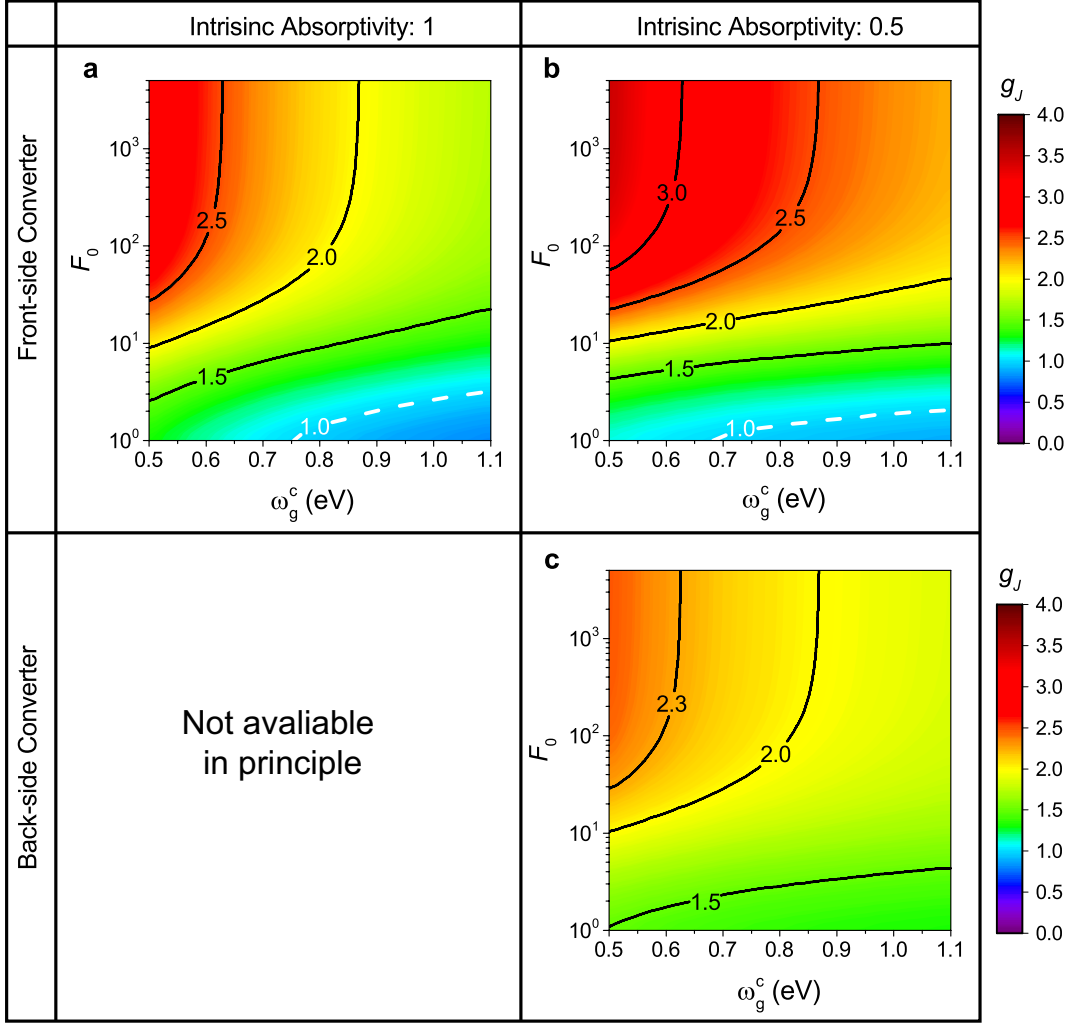


Figure 3.4: The gain ratio of short-circuit current density in the down-conversion configuration. (a) and (b) front-side down-converter with intrinsic above-bandgap absorptivities of both components equal to 1 and 0.5, respectively; (c) back-side down-converter with intrinsic above-bandgap absorptivities of both components equal 0.5. The back-side converter down-converter is not available in principle when the solar cell has an ideal absorption at the front side.

levels. Therefore, receiving a larger excitation becomes the particular advantage of the front-side converter for the OHCS<sup>3</sup>. Then, it has to introduce a sufficiently large optical enhancement to realize the potential, as shown in Figure 3.3(c) and (d).

Overall, with the trade-off between the excitation power and conversion yield mentioned above, a maximum  $g_J$  appears around  $\omega_g^c \approx 0.7 \sim 0.8$  eV in the four cases of Figure 3.3 with the highest value of  $F_0$ . Strictly speaking, in the front-side converter and semi-transparent cases above, the photon (carrier) down-conversion can also contribute to the final yield of carrier hot-luminescence since the emission frequency  $\omega_g^D$  may be lower than the average frequency of the absorbed incident spectrum<sup>4</sup>. The down-conversion can

<sup>3</sup>The poor blue response of a conventional solar cell can be another advantage of the front-end converter, however, since the ideal cell is assumed, it is not included here.

<sup>4</sup>Again, the definition of an up-converter in Ref. [8] is followed in this thesis, which simply means

happen here due to the continuous conversion yield in the hot carrier absorber and efficient AI process occurring reciprocally. However, it would not affect the general conclusions to improve the conversion yield discussed above.

Quite similar effects can be seen in the down-conversion configuration as shown in Figure 3.4. In this case, a back-side down-conversion converter is not available in principle when  $a_p = 1$ . Due to a better matching between the emission and reabsorption profiles ( $\omega_g^p = \omega_g^c$ ) and typically higher  $\dot{Q}_{s-c}$ , the average  $g_J$  are larger than the up-conversion configurations. The highest photon current gain still appears in the front-side converter, reaching about 3.46 as shown in 3.3(b). It is important to emphasize that the results in Figure 3.3 are irrelevant to the PCE optimization over the bandgap energy  $\omega_g^p$ , which also depends on the trade-off with the open-circuit voltage. Instead, it only shows whether the precondition Eq. (3.5) is fulfilled or not. Interestingly, it is still possible to lose photon current in a front-side down-converter if no optical enhancement exists in the internal luminescence transfer, as shown in Figure 3.3(a) and (b). The front-side radiation escape and insufficient conversion yield are the main reasons here.

### 3.3.2 Effect of frequency filter

An ideal monochromatic optical coupling requires all the transferred luminescence out of the extraction window to be zero. As the problem faced by the electronic energy selective contacts (ESC) [57], a rigorous energy selection is better in principle to convert the spectrum, which however leads to a higher current resistance in turn. It, therefore, requires an even larger  $F_0$  to compensate the optical resistance given by an ideal frequency filter.

By modifying the non-ideal rectangular profile of  $a_p^0 a_c^0 F_0$  in  $\dot{N}_{c-p}$  and  $\dot{N}_{p-c}$  from the previous models (see Figure 3.2), Figure 5 shows the results when an ideal frequency filter is applied into the OHCSC. A front-side spectrum converter is considered there since the far-field radiation from the top surface makes it more sensitive to the photon losses. Here use  $\omega_g^c = 0.7$  eV,  $\omega_g^p = 1.1$  eV in the up-conversion case and  $\omega_g^c = \omega_g^p = 0.7$  eV in the down-conversion case here as examples. The results show evident photon losses when the ideal filter is applied and  $F_0$  is below 50, especially in the down-conversion. When  $F_0$  is close to 5000, the gain ratio with a perfect filter does show a larger than its counterpart but the increment is just of the order of  $\times 10^{-5}$  in all cases.

---

$\omega_g^c < \omega_g^p$  as shown in Figure 3.1.

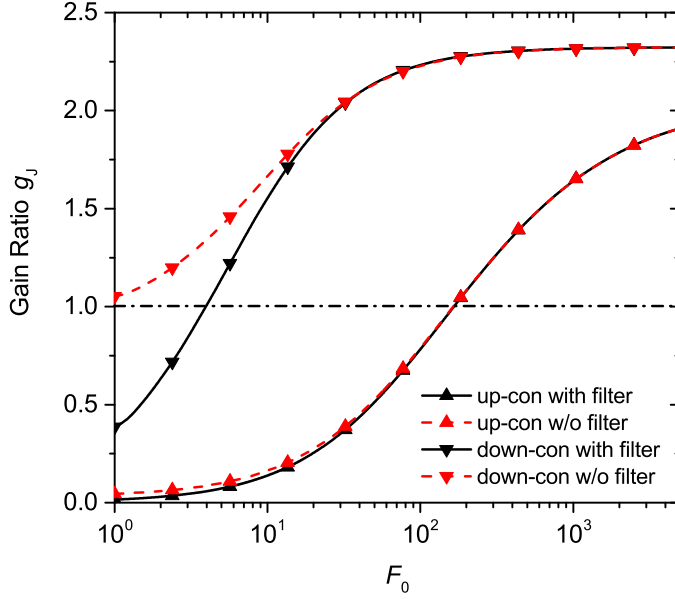


Figure 3.5: Effects of an ideal frequency filter around the coupling frequency. With the presence of the ideal filter, the transfer spectrum of luminescence will be zero outside the energy range  $\omega_g^p \sim \omega_g^p + \Delta\omega$ . A front-side converter with  $\omega_g^c = 0.7$  eV is used in both of the up- ( $\omega_g^p = 1.1$  eV) and down-conversion ( $\omega_g^p = 0.7$  eV) configurations to show the differences. Both components have ideal absorptions here ( $a = 1$ ).

### 3.3.3 Influences on the open-circuit voltage and device efficiency

The analytical formula of  $V_{oc} \approx k_B T_{rt}/q \cdot \ln(J_{sc}/J_0)$  for the PV cell can be derived from Eq. (3.3) and Eq. (3.4), as given below

$$\begin{cases} V_{oc} \approx \frac{k_B T_{rt}}{q} \cdot \ln \left[ \frac{\dot{N}_{s-p}(R_c f_s a_p, T_s, 0) + \dot{N}_{c-p}(\pi a_p^0 a_c^0 F_0, T_c, 0)}{\dot{N}_{p-f}(\pi a_p, T_{rt}, 0) + \dot{N}_{p-c}(\pi a_p^0 a_c^0 F_0, T_{rt}, 0)} \right] & ; \text{ with the converter} \\ V_{oc}' \approx \frac{k_B T_{rt}}{q} \cdot \ln \left[ \frac{\dot{N}_{s-p}(R_c f_s, T_s, 0)}{\dot{N}_{p-f}(\pi, T_{rt}, 0)} \right] & ; \text{ w/o the converter} \end{cases} \quad (3.6)$$

$$V_{oc} \approx \begin{cases} \frac{k_B T_{rt}}{q} \cdot \ln \left[ \frac{\dot{N}_{s-p}(R_c f_s, T_s, 0)}{\dot{N}_{p-f}(\pi, T_{rt}, 0)} \right] = V_{oc}', F_0 \rightarrow 0 \\ \frac{k_B T_{rt}}{q} \cdot \ln \left[ \frac{\dot{N}_{c-p}(\pi, T_c, 0)}{\dot{N}_{p-c}(\pi, T_{rt}, 0)} \right], F_0 \rightarrow \infty \end{cases} \quad (3.7)$$

Since a step-like absorptance is considered in this modeling with a uniform above bandgap value, the intrinsic absorptivity  $a_p^0$  is then canceled in both the top and bottom row of  $V_{oc}'$  in Eq. (3.6). It is necessary to emphasize again that the far-field emission only occurs at the front surface of the device in this modeling, where the emission cross-section in a unit étendue is fully reciprocal with the absorption for far-field radiation,

and therefore the open-circuit voltage  $V_{oc}'$  is irrelative to the absorptivity  $a_p^0$ . When the converters appear, additional two fluxes  $\dot{N}_{c-p}$  and  $\dot{N}_{p-c}$  arise as well in the  $V_{oc}$ .

Two limiting situations are considered first. If there is no additional optical enhancement at all with  $F_0 = 0$  but only shading from the converter, the  $V_{oc}$  is equal to  $V_{oc}'$  ( $a_p$  cancels out). If there is an ultra-strong coupling with  $F_0 \rightarrow \infty$ ,  $V_{oc}$  is then determined by the steady state carrier temperature  $T_c$  in the spectrum converter, as shown in Eq. (3.7). Again, the same factor  $a_p^0 a_c^0 F_0$  is also canceled in the second case of Eq. (3.7). Since the carrier temperature cannot be larger than  $T_s$  in general, it results in a voltage loss of the cell  $g_V = V_{oc}/V_{oc}' < 1$ . In between the above two situations,  $V_{oc}$  is an increasing function of  $F_0$  if  $T_c$  is invariant.

However,  $T_c$  is not a fixed number in the practical situation and is determined by Eq. (3.2) in each specific steady state and therefore varies along with  $F_0$ . Actually that  $T_c$  will be a decreasing function of  $F_0$  as shown in Figure 3.6(a), since the carrier hot-luminescence emission/extraction is an “energy loss” process for the converter which can down-shift the steady state temperature of the dipole population (red curve in Figure 3.6(a)). As a consequence, the pseudo- $V_{oc}$ , evaluated by the formula  $V_{oc} \approx k_B T_{rt}/q \cdot \ln(J_{sc}/J_0)$  at the short-circuit condition of the PV cell, also decreases with rising  $F_0$  (blue curve in Figure 3.6(a)).

When the cell is working with a positive bias voltage ( $V > 0$ ), the feedback electroluminescence (EL) from the cell will also influence Eq. (3.2), further shifting the steady state temperature  $T_c$ . The effect of the feedback EL may be ignored in the previous analysis of the spectrum conversion system [110] but must be taken into account when a strong optical coupling appears.

On the one hand,  $T_c$  will increase under a larger bias voltage (black line in Figure 3.6(b)), since the feedback EL from the PV cell is an “energy gain” process of the converter. It, therefore, up-shifts  $T_c$  and also enlarges the transferred luminescence  $\dot{N}_{c-p}$  when pushing up the working voltage of the cell. A direct inference here is that a “voltage-dependent open-circuit voltage” must exist in the device. This means that the actual  $V_{oc}$ , as well as the maximum power point ( $V_{MPP}$ ), of the PV cell is higher than the pseudo value estimated at the short-circuit condition, since the actual input photon currents become greater along with the bias voltage ( $\dot{N}_{c-p}|_{V>0} > \dot{N}_{c-p}|_{V=0}$ , added with a constant  $\dot{N}_{s-p}$ ). This phenomenon is presented in Figure 6(a), where the blue dashed line and blue solid line are the pseudo and actual gain ratios of open-circuit voltage  $g_V$ , respectively. It suggests that the divergence between these two values will even increase with  $F_0$ . In

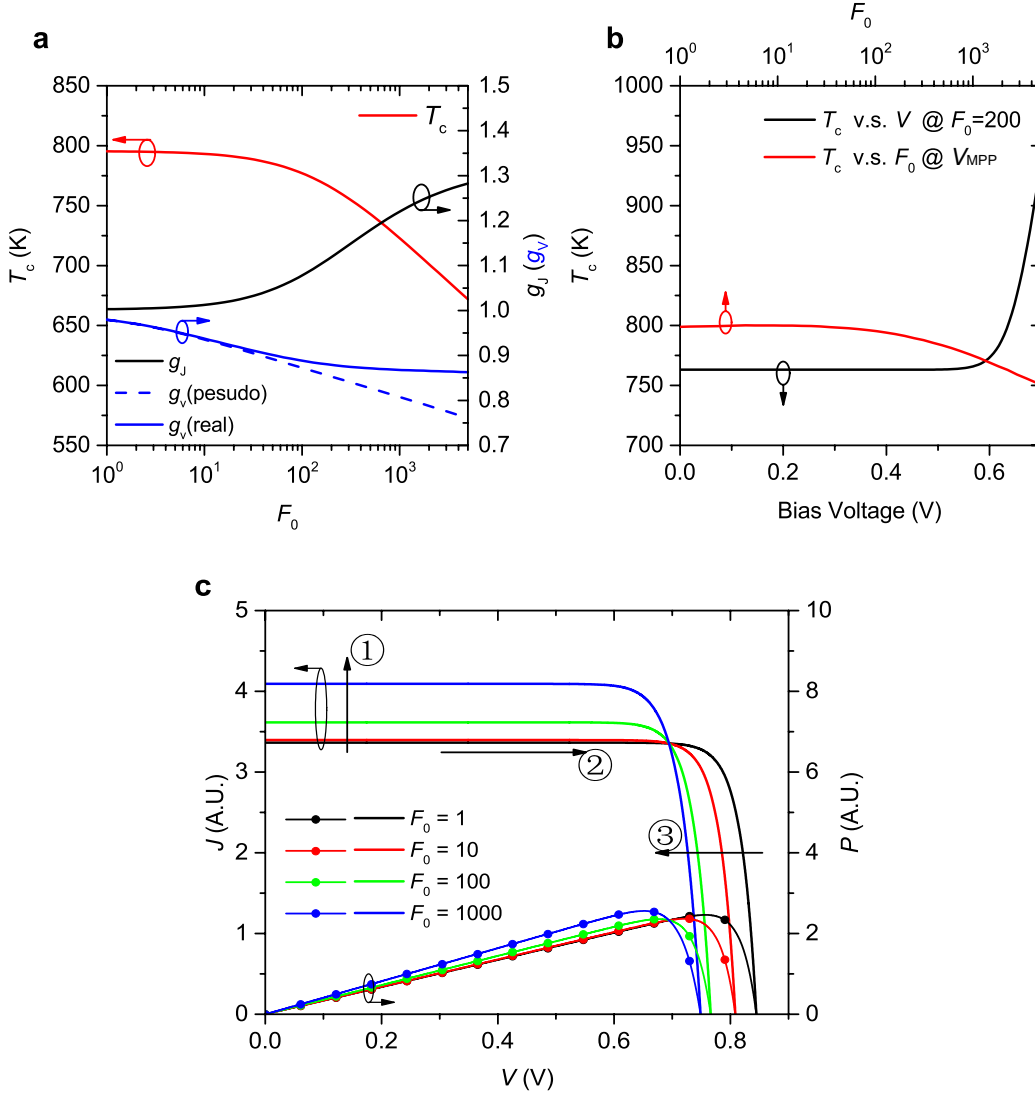


Figure 3.6: Carrier temperature and working voltage in a back-side up-converter. The bandgap of converter and PV cell are 0.7 eV and 1.1 eV respectively. The intrinsic above-bandgap absorptance is 1 in both components. (a) Steady hot carrier temperature  $T_c$ , with  $V = 0$ , gain ratio of the short-circuit current density  $g_j$ , gain ratio of the open-circuit voltage  $g_v$  under different optical enhancement ratios. The pseudo open-circuit voltage is that estimated at the short-circuit condition, which is different to the actual values of the cell. (b) Black line: Steady hot carrier temperature  $T_c$  solved under different bias voltages  $V$  of the PV cell with a fixed  $F_0 = 200$  ( $T_c$  v.s.  $V$  @  $F_0 = 200$ ); Red line: Steady hot carrier temperature  $T_c$  solved at the maximum power point ( $V_{\text{mpp}}$ ) of the PV cell with different  $F_0$  ( $T_c$  v.s.  $V$  @  $V_{\text{mpp}}$ ). (c) The complete J-V and P-V curves of the device under different optical enhancement ratios. The major variation mechanisms of the J-V property are labeled as: 1) Optical enhancement increases  $J_{\text{sc}}$ ; 2) “Voltage dependent open-circuit voltage”; 3)  $T_c$  decrease along with larger  $F_0$ .

the view of cell operations, this phenomenon comes from the fact that a good spectrum converter without non-radiative losses ( $\dot{Q}_{\text{th}} \rightarrow 0$ ) could restore parts of the EL back to the cell, especially when the internal luminescence transfer is more efficient than the outgoing radiation ( $F_0 \gg 1, \dot{N}_{\text{c-p}} \gg \dot{N}_{\text{c-s}}$ ). As a consequence, it quenches the far-field radiative recombination losses of the PV cell effectively and elevates the  $V_{\text{oc}}$ . Importantly, Eq. (3.6) is still valid here to calculate the actual  $V_{\text{oc}}$  if a correct  $T_c$  is used in the formula.

On the other hand, the carrier temperature  $T_c$  and also the luminescence flux  $\dot{N}_{c-p}(T_c)$  at the maximum power point ( $V_{MPP}$ ) are still (almost always) reducing versus  $F_0$  (red curve in Figure 6(b)). Therefore, a similar decreasing tendency also exists for the real characteristic voltages ( $V_{oc}, V_{MPP}$ ) of the cell, like that of the pseudo- $V_{oc}$  discussed above. It is confirmed in the complete J-V and P-V curves in Figure 3.6(c).

In summary, the characteristic voltages and also the electrical power of the PV cell show a complex variation dependence on different mechanisms. Figure 6(c) labels the major three mechanisms have been discussed above: 1) Optical enhancement increases  $J_{sc}$ ; 2) “Voltage dependent open-circuit voltage”; 3)  $T_c$  decreases along with larger  $F_0$ . These observations also suggest the essential aspect of Eq. (3.5) that is the conversion yield of hot-luminescence current determines the actual performance of the device, whose intensity is also tunable using photonic engineering.

As a corollary to the above observations, in a rigorous consideration, it is possible to gain a final efficiency enhancement in the device even if the condition of Eq. (3.5) is not met at  $V = 0$ , since the phenomenon of “voltage-dependent open-circuit voltage” can still push the  $V_{MPP}$  up a little bit. However, such a critical situation has almost no practical significance. Therefore, we still conclude that Eq. (3.5) is a prerequisite for obtaining PCE enhancements in practice.

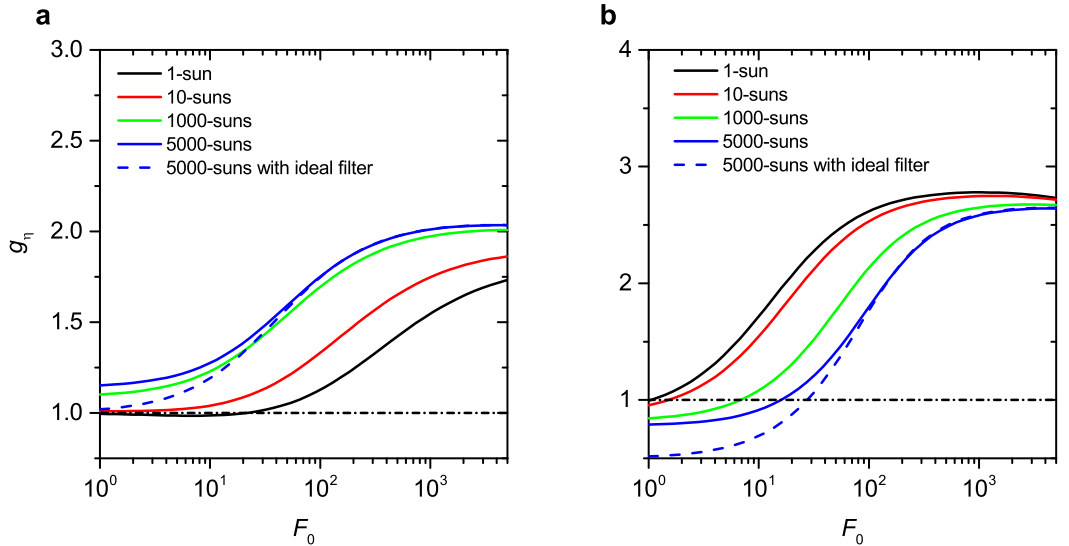


Figure 3.7: Representative PCE enhancement  $g_n$  ratio evaluated from two legendary configurations: (a) back-side up-converter. The bandgap of the converter and PV cell are 0.7 eV and 1.1 eV respectively; (b) front-side down-converter. The bandgaps of both the converter and PV cell are 0.7 eV. The intrinsic above-bandgap absorptance is 0.5 in both components and all cases.

With this understanding above, the overall PCE enhancement ratios  $g_n = \eta/\eta'$  are given below in two representative situations (compared to the regular detailed-balance

results  $\eta'$  with the same bandgap and optical concentration  $R_c$ ). Two specific configurations are presented here, a back-side up-converter with  $\omega_g^c = 0.7 \text{ eV}$  and  $\omega_g^p = 1.1 \text{ eV}$  and a front-side down-converter with  $\omega_g^c = \omega_g^p = 0.7 \text{ eV}$ . An intrinsic above-bandgap absorptance of 0.5 applies to all components. In particular, the effect of an ideal frequency filter is also given in the 5000-suns case, where an inadequate  $g_\eta$  is observed again when the  $F_0$  is below about 50 times.

### 3.4 Understanding luminescence transfer

The basis of luminescence emission and the methodology of optical enhancement will be discussed in this section. It summarizes the typical strategies and design principles of luminescence management.

#### 3.4.1 Internal luminescence and light extraction

In a thermal-equilibrium state, the photoluminescence (PL) flux of semiconductors is given by the van Roosbroek–Shockley relation as shown below

$$\dot{Q}_{\text{PL}}(\omega) = \alpha(\omega) \frac{\omega^2 n_c^3}{\pi^2 c^3} \cdot f_{\text{ph}} \cdot \frac{c}{n_c} \cdot \hbar\omega \quad (3.8)$$

In the above equation, the first term  $\alpha(\omega)$  is the photon emissivity. It is the absorption coefficient of the material when discussing the local PL density inside the material while becomes the integrated absorptance  $a(\omega)$  over the whole emitter in a collective emission scenario [120]. The second term is the local density of optical states (LDOS) of the converter with a refractive index of  $n_c$ . To simplify the discussion, the anisotropy of the photonic environment is ignored here. The third term  $f_{\text{ph}}$  is the photon occupation function while the fourth term above is the photon propagation speed inside the medium. The corresponding far-field luminescence needs to consider an additional extraction efficiency  $\eta_{\text{ext}}$ , which bridges the divergence of the LDOS between the luminescence emitter and the propagation medium [115]. For a thick planar geometry, the  $\eta_{\text{ext}}$  can be approximated as  $n_m^2/4n_c^2$  which is just the reciprocal of the Yablonovitch limit of light trapping [121, 122] when the refractive index of the outer medium is  $n_m$ . Therefore, the far-field PL flux is

$$\begin{aligned} \dot{Q}_{\text{PL}}(\omega) \cdot \eta_{\text{ext}} &= a(\omega) \cdot \frac{\omega^2 n_m^2}{4\pi^2 c^2} \cdot f_{\text{ph}} \cdot \hbar\omega \quad [d\omega] \\ &= a(\omega) \cdot \frac{2\pi n_m^2 \epsilon_{\text{ph}}^2}{h^3 c^2} \cdot f_{\text{ph}} \cdot \epsilon_{\text{ph}} \quad [d\epsilon_{\text{ph}}] \end{aligned} \quad (3.9)$$

The above equation recovers the Eq. (3.1) in a planar geometry, where  $\epsilon_{\text{ph}}$  is the single photon energy.

### 3.4.2 Increasing the luminescence transfer rate by photonic engineering

According to Eq. (3.9), the transfer rate of luminescence through a photonic environment depends on both the LDOS and coupling efficiency.

In the far-field coupling configuration as shown in Figure. 3.8(a), the PL intensity can typically be increased by using a coupling layer and antenna system. Nano-photonics allows a deeper engineering on the local electric fields. As a consequence, the transition period of radiative dipoles can also become shorter, which therefore increases the quantum yield of the emitter substantially. Therefore, the overall luminescence leaving a spectrum converter to the far-field can be written as

$$\dot{Q}_{\text{c-p}} |_{\text{far}}(\omega) = F_{\text{f}} \frac{\omega^2 n_{\text{m}}^2}{4\pi^2 c^2} \cdot f_{\text{ph}} \cdot \hbar\omega \quad (3.10)$$

, where factor  $F_{\text{f}}$  includes additional optical benefits from both the coupling efficiency and photon yield enhancement. The intrinsic emissivity of the converter and also the absorptivity of the PV cell are assigned as one.

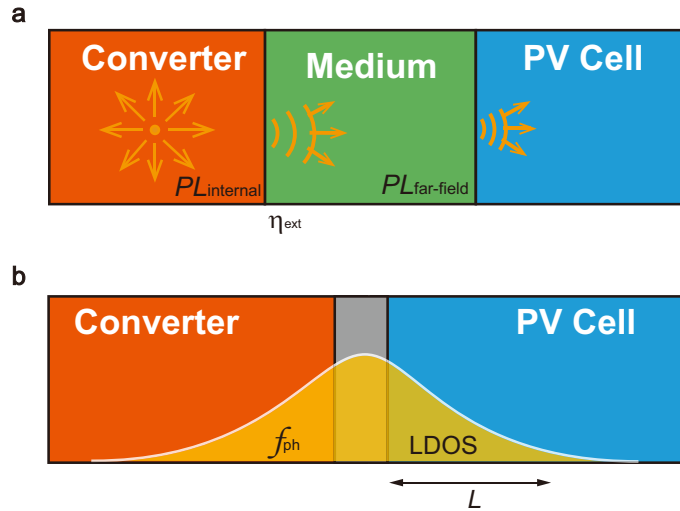


Figure 3.8: Luminescence transfer in (a) far-field coupling via propagating mode,  $\eta_{\text{ext}}$  is the luminescence extraction efficiency; (b) near-field coupling via localized mode, the local absorption of the PV cell depends on the photon occupation function  $f_{\text{ph}}$  and the LDOS of the cell within a mode penetration length  $L$ .

It is noted that the outgoing coupling efficiency of propagating modes can never be greater than 1. Besides, the local field enhancement conflicts with a larger far-field radiation efficiency in principle. Hence, near-field reabsorption can better utilize the enlarged

LDOS in the structure in principle. Let's consider such an instance, where the luminescence emitter and PV cell are coupled by the same cavity resonant mode in the near-field as shown in Figure 3.8(b). Then the localized evanescent field is able to penetrate directly into the PV cell and deliver electromagnetic power. By assuming the intrinsic emissivity equal to one, the transferred optical power in an equilibrium state can be approximated as [123]

$$\dot{Q}_{\text{c-p}}|_{\text{near}}(\omega) = F_n \frac{\omega^2 n_p^3}{\pi^2 c^3} \cdot f_{\text{ph}} \cdot \hbar\omega \cdot \omega \cdot \varepsilon_p''(\omega) \cdot L \quad (3.11)$$

In the above equation,  $F_n \frac{\omega^2 n_p^3}{\pi^2 c^3}$  is the LDOS of the PV cell (refractive index  $n_p$ ) modulated by the cavity mode with an enhancement factor  $F_n$ ,  $f_{\text{ph}}$  is the photon occupation function determined by the emitter,  $\omega \cdot \varepsilon_p''(\omega)$  is known as the optical conductivity of the material where  $\varepsilon_p''(\omega)$  is the imaginary part of the PV cell's dielectric function. A field penetration depth  $L$  into the PV cell is added in Eq. (3.11) to convert the photon density into a flux which is determined by the optical mode and photonic structure.

A very general comparison between the far- and near-field luminescence transfers is given below. Supposing all the far-field radiation  $\dot{Q}_{\text{c-p}}|_{\text{far}}$  could be reabsorbed by a thick PV cell via air, while all the local fields  $\dot{Q}_{\text{c-p}}|_{\text{near}}$  are absorbed within its penetration length, the ratio between the far- and near-field optical power will be

$$\frac{\dot{Q}_{\text{c-p}}|_{\text{near}}(\omega)}{\dot{Q}_{\text{c-p}}|_{\text{far}}(\omega)} = \frac{F_n}{F_f} \cdot \left[ 8\pi n_p^2 \cdot \varepsilon_p''(\omega) \cdot \frac{n_p L}{\lambda} \right] \quad (3.12)$$

In the above equation, the factor  $n_p L / \lambda$  is approximated to be the normalized expansion length of the resonant mode inside the PV cell. For the present resonant cavities in nano-optics, a typical mode volume is around  $0.1(\lambda/n)^3$  in the dielectric photonic cavities [63, 67, 124] and  $0.001(\lambda/n)^3$  in the plasmonic cavities [71, 125, 126], leading to  $L \approx 0.3(\lambda/n)$  on average. If it is further supposed that a typical PV cell has a refractive index 3.5 and band edge  $\varepsilon_p''$  around 0.1, then the factor  $8\pi n_p^2 \cdot \varepsilon_p''(\omega) \cdot \frac{n_p L}{\lambda}$  in Eq. (3.12) can reach to about 9.2. It means that the far-field enhancement factor  $F_f$  has to be around 10 times of the  $F_n$  to transfer the same amount of optical energy, providing the propagating modes could be fully absorbed within a device length of  $n_p L / \lambda$ .

In practices, the far-field coupling requires a sufficiently large optical thickness of the PV cell to absorb the luminescence near the bandgap entirely. It, therefore, shows obvious disadvantage on the nano-structured solar cell. Instead, the near-field coupling scheme introduces field localization in principle, which is typically comparable or even smaller

than the nano-size of the device. Hence, it can maximize the luminescence collection efficiency in a natural way. Of course, the near-field coupling scheme also has systematic energy losses during the luminescence transfer. Typical examples include the inevitable radiation escaping to the far-field and parasitic absorption by the photonic structures. These effects will be discussed in detail in Chapter 5.

### 3.5 Thermodynamic limit of spectrum conversion

All the above discussions have addressed the influence of the optical enhancement to a spectrum conversion system, which increases the coupling efficiency of the electromagnetic energy. It is based on a precondition that the spectrum conversion occurs spontaneously and continuously inside the spectrum. This section discusses the thermodynamic requirement of spectrum conversion.

Apart from a sufficiently long non-radiative relaxation lifetime of the excited entities, a non-equilibrium carrier population must also be kept in the material to force a spontaneous conversion process which is asked by the second law of thermodynamics [112]. This non-equilibrium distribution requires

$$\begin{aligned} \mu(\omega) &\geq \mu_0 \frac{\omega}{\omega_0} \\ f_{\text{ph}}(\omega; T_c, \mu) &\geq \left[ \left( f_{\text{ph}}(\omega_0; T_c, \mu_0)^{-1} + 1 \right)^{\omega/\omega_0} - 1 \right]^{-1} \end{aligned} \quad (3.13)$$

, where  $\mu(\omega)$  is the chemical potential of photons at frequency  $\omega$  while  $\omega_0$  is the coupling frequency,  $T_c$  is the photon temperature in the converter,  $f_{\text{ph}}$  is the photon occupation function. Such a thermodynamic directionality makes a further limitation on the power conversion efficiency of the device. However, it will not affect the design principle of the photonic engineering to maximize the transfer rate of optical energy. In the previous sections, the chemical potential of dipoles inside the converter is assumed to be zero ( $\mu(\omega) = 0$ ) which is recognized as a critical condition to fulfill Eq. (3.13) for an arbitrary  $\omega_0$ . Complicated relaxation processes among different carrier scattering mechanisms have to be considered to understand the device performance in a non-equilibrium steady state, such as using the relaxation-time approximation (RTA) model discussed in the next chapter where the impact of carrier thermalization losses will also be fully addressed.

### 3.6 Conclusion

In this chapter, the general working principles of the optical hot carrier solar cell are discussed from a thermodynamic perspective. Exporting the carrier hot-luminescence at an arbitrary energy level to pump a conventional solar cell is recognized as a general representation of spectrum conversion processes both phenomenologically and thermodynamically. The gain of photon currents is then recognized as a general and minimum precondition to improving the PCE of the device, in both of the up- and down-conversion configurations. It hence requires photonic engineering to increase the luminescence transfer efficiency around the coupling frequencies, where the localized near-field coupling shows a greater potential. On the other hand, the output voltage and device efficiency are strongly affected by the thermodynamic state and conversion yield of the converter, where the feedback EL from the PV cell shows a significant impact in the deep coupling scenario. It results in a complex dependence of the device performance on both the optical enhancement ratio and also the working voltage itself known as the “voltage-dependent open-circuit voltage”. Importantly, all the above conclusions are also applicable to the conventional spectrum converters with photonic modifications.

## Chapter 4

# Investigation of Hot-luminescence Conversion using Relaxation-Time Approximation Model

This chapter further investigates the design and working principles of the optical hot carrier solar cell (OHCSC) using the relaxation-time approximation (RTA). By assigning practical relaxation lifetimes of carrier scattering, the RTA addresses the non-equilibrium steady state of the converter and takes the thermalization losses fully into account. It, therefore, can predict a more reasonable device performance and avoid the limitation imposed by the requirement of thermal-equilibrium added in the conventional detailed-balance model. This chapter is organized as follows. Section 4.1 shows the necessity and advantages of using the RTA model. Section 4.2 introduces the theoretical framework of the RTA modeling. A down-conversion system is systematically investigated in Section 4.3 as a numerical example. More detailed discussions and comments to understand the RTA model and the device design principle are given in Section 4.4. It compares the practical device performance and those ideal cases discussed in Chapter 3 to depict a comprehensive understanding of the OHCSC.

### 4.1 Introduction

The thermal-equilibrium of a carrier population is one of the classic approximations used in the photovoltaic analyses, especially in the estimation of limit efficiency [111, 116]. However, this approximation is rigorously exact only when the solar cell is in the open-

circuit condition with negligible non-radiative recombination. For a conventional solar cell under an arbitrary bias voltage  $V$ , the equilibrium approximation is still solid since the carrier population has quickly relaxed to the band edge at the ambient temperature (300 K) and background electrical potential ( $V$ ) within picoseconds. Fast elastic carrier-carrier scatterings also renormalize the carrier population continuously to the equilibrium distribution.

However, this approximation becomes questionable in the hot carrier scenario, especially when the non-radiative thermalization losses needs to be well considered. When the carrier cooling rate becomes slow and the luminescence transfer rate is enlarged, there has room for competition between multiple carrier dynamics. Hence, the final steady state of the carrier population could be strongly non-equilibrium, as suggested by Feng et al. [34]. As a consequence, electrons and holes may not follow the Fermi-Dirac distributions in the material so does the luminescence bias away from the Boss-Einstein statistics.

Also, the yield of carrier hot-luminescence heavily relies on the actual thermal-state of hot carriers in the converter, as concluded in the last chapter. When photonic engineering is applied along with the optical energy selective contact (OESC), significant optical enhancements will perturb the carrier population further. Therefore, recognizing the non-equilibrium steady state of the converter becomes vital to predict the device performance more accurately.

This chapter uses the RTA model [34] with experimentally available material parameters to examine the device performance. In the RTA model, we consider a particular distribution of charge carriers in the converter. The carrier dynamics caused by each mechanism is represented by a simple relaxation process to push the carrier gas towards to the corresponding thermal-equilibrium state. The final steady state is then determined by mutual competition between different evolution channels as they occur in practice. It, therefore, suggests practical working principles and design requirements of the OHSC.

## 4.2 Relaxation-time-approximation model

The modeling procedure of the RTA centers on the evaluation of carrier distributions in the spectrum converter  $n(\epsilon_e, t)$ ,  $p(\epsilon_h, t)$ , defined by energy states  $\epsilon_e$ ,  $\epsilon_h$  and time delay  $t$ . Symbol  $n$  and  $p$  are the volume densities of electrons and holes respectively, while  $\epsilon_e$ ,  $\epsilon_h$  are their electronic energy levels above each band edge. A non-equilibrium carrier distribution will naturally relax to a corresponding equilibrium state within a finite period after the

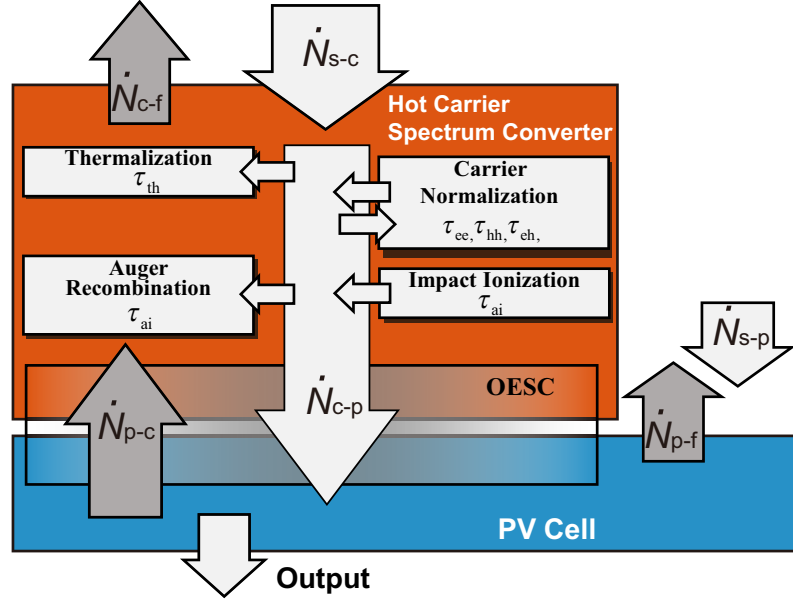


Figure 4.1: Schematic illustration of multiple carrier evolution mechanisms in the optical hot carrier solar cell.  $\dot{N}_{s-c}$  and  $\dot{N}_{c-f}$  denote the photon fluxes between the hot carrier converter and the external environment, while  $\dot{N}_{s-p}$  and  $\dot{N}_{p-f}$  are the external fluxes of the photovoltaic (PV) cell.  $\dot{N}_{p-c}$  and  $\dot{N}_{c-p}$  are the internal photon fluxes between the converter and PVs cell through an OESC structure. The final steady state and operating condition of the system are determined by real-time competitions between all these carrier dynamical processes in the converter.

perturbation disappears, as required by the second law of thermodynamics. Therefore, the dynamic variations of carrier population  $\Delta n(\epsilon, t)$  caused by a particular mechanism “ $x$ ” can be approximated by an exponential relaxation process characterized by a lifetime  $\tau_x$ . The total evolution rate of electrons in the converter  $dn(\epsilon_e, t)/dt$  can then be represented as

$$\begin{aligned} \frac{dn(\epsilon_e, t)}{dt} = & - \frac{n(\epsilon_e, t) - n_{eq_{ee}}(\epsilon_e)}{\tau_{ee}} - \frac{n(\epsilon_e, t) - n_{eq_{eh}}(\epsilon_e)}{\tau_{eh}} \\ & - \frac{n(\epsilon_e, t) - n_{eq_{th}}(\epsilon_e)}{\tau_{th}} - \frac{n(\epsilon_e, t) - n_{eq_{ai}}(\epsilon_e)}{\tau_{ai}} \\ & + \frac{\dot{N}_{s-c}(\epsilon_e) - \dot{N}_{c-f}(\epsilon_e, t)}{d} + \frac{\dot{N}_{p-c}(\epsilon_e) - \dot{N}_{c-p}(\epsilon_e, t)}{d} \end{aligned} \quad (4.1)$$

All the considered carrier dynamics in Eq. (4.1) are labeled in Figure 4.1. A similar equation also holds for the holes’ distribution  $p(\epsilon_h, t)$  in the converter. Detailed explanations of Eq. (4.1) are given in the following subsections.

#### 4.2.1 Relaxation approximation of carrier scattering

The first four terms on the right-hand-side (RHS) of Eq. (4.1) are the relaxation terms caused by carrier scatterings including: 1) elastic electron-electron scattering; 2) elastic

electron-hole scattering; 3) thermalization and 4) Auger-recombination/Impact-ionization (AI).

In those terms,  $n(\epsilon_e, t)$  is the real-time electron density at energy  $\epsilon_e$  which is compared with the equilibrium distributions  $n_{\text{eq-}x}(\epsilon_e)$  resulting from each relaxation process. The subscript “ $x$ ” here is written as “ee”, “eh”, “th” and “ai” in Eq. (4.1) to represent the above four kinds of carrier scattering respectively. The evolution rates of carrier density are then defined with the corresponding relaxation lifetimes  $\tau_{\text{ee}}$ ,  $\tau_{\text{eh}}$ ,  $\tau_{\text{th}}$ ,  $\tau_{\text{ai}}$  of each mechanism. In particular, the non-radiative carrier recombination is ignored here whose lifetime is typically much longer than that of the carrier scatterings considered here (see below) in a good spectrum converter.

The same methods used in Ref. [34] give those thermal-equilibrium distributions  $n_{\text{eq-}x}(\epsilon_e)$  from an arbitrary non-equilibrium state. For example, elastic electron-electron scattering will conserve both the total carrier energy and carrier number before and after the relaxation. These two equations can calculate the ensemble-averaged carrier temperature and the chemical potential for the corresponding equilibrium state, where carriers will follow a rigorous Fermi-Dirac distribution (two equations, two variables). Instead, carrier thermalization will only conserve the carrier number which gives the equilibrium chemical potential at 300 K. The AI process, including both the forward multiplication and reverse fusion, uses a single relaxation time  $\tau_{\text{ai}}$ . The overall effect of these two reciprocal processes in thermodynamics drives the electrochemical potential of electron-hole pairs towards zero [7].

### 4.2.2 Optical interaction with surroundings

The last two terms at the RHS of Eq. (4.1) are the photon fluxes  $\dot{N}$  associated with the spectrum converter. These fluxes are in the same symbolic system defined in Chapter 3, in which the subscript labels the direction in the way of “emitter-receiver” and “s”, “f”, “p”, “c” are shorthands for the sun, free-space, PV cell, and converter, respectively. With the notations used here, the fifth term in Eq. (4.1) is the net photon flux exchanged with the external environment at  $\epsilon_e$  while the final term is the net photon flux being exchanged with the PV cell. In particular,  $\dot{N}_{\text{p-c}}$  is the feedback electroluminescence (EL) from the PV cell, which is recognized to have significant impacts on the conversion process from the last chapter. The extra factor  $d$  in the denominator is the thickness of the converter, which converts the photon flux to the carrier density in a slab geometry. In details, these

photon fluxes are written as

$$\dot{N}_{s-c}(\epsilon_e) = \frac{2X_{s-c}}{h^3 c^2} \frac{\epsilon_{ph}^2}{\exp[\epsilon_{ph}/k_B T_s] - 1} \quad (4.2)$$

$$\dot{N}_{c-f}(\epsilon_e) = \frac{2X_{c-f}}{h^3 c^2} \frac{\epsilon_{ph}^2}{[\rho_e(\epsilon_e)/n(\epsilon_e) - 1] [\rho_h(\epsilon_h)/p(\epsilon_h) - 1]} \quad (4.3)$$

$$\dot{N}_{p-c}(\epsilon_e) = F_0(\epsilon_{ph}) \cdot \frac{2X_0}{h^3 c^2} \frac{\epsilon_{ph}^2}{\exp[(\epsilon_{ph} - qV)/k_B T_{rt}] - 1} \quad (4.4)$$

$$\dot{N}_{c-p}(\epsilon_e) = F_0(\epsilon_{ph}) \cdot \frac{2X_0}{h^3 c^2} \frac{\epsilon_{ph}^2}{[\rho_e(\epsilon_e)/n(\epsilon_e) - 1] [\rho_h(\epsilon_h)/p(\epsilon_h) - 1]} \quad (4.5)$$

$$\begin{cases} \epsilon_h = m_e^*/m_h^* \cdot \epsilon_e \\ \epsilon_{ph} = E_g^c + \epsilon_e + \epsilon_h \end{cases} \quad (4.6)$$

In particular, Eq. (4.2) ~ Eq. (4.5) are defined by the electron energy level above the band edge,  $\epsilon_e$ . The correspondence between the electron energy  $\epsilon_e$ , hole energy  $\epsilon_h$  and photon energy  $\epsilon_{ph}$  are given in Eq. (4.6), where  $E_g^c$  is the bandgap energy of the converter material. A parabolic band structure characterized by the electron and hole effective masses ( $m_e^*$ ,  $m_h^*$ ) is used here, and only the direct optical transition is considered. The symbol  $X_{s-c}$  and  $X_{c-f}$  above are the generalized étendues<sup>1</sup> between the sun (“s”) and converter (“c”), while  $X_0$  is the same generalized mutual étendue between the converter and PV cell. Since the generalized étendue includes collective absorptivity/emissivity of the component, therefore it also contains the information about the converter’s bandgap  $E_g^c$ . Function  $F_0$  above introduces the effect of photonic engineering. It is written as a multiple of the far-field radiation spectrum with a particular frequency dependent profile, like that defined in Chapter 3.

Instead of the standard Bose-Einstein factor used in Eq. (4.2) and Eq. (4.4), a generalized dipole occupation function  $\{[\rho_e(\epsilon_e)/n(\epsilon_e) - 1] [\rho_h(\epsilon_h)/p(\epsilon_h) - 1]\}^{-1}$  is used in Eq. (4.3) and Eq. (4.5) to describe the non-equilibrium luminescence from the converter [120], where  $\rho_e(\epsilon_e, m_e^*)$  and  $\rho_h(\epsilon_h, m_h^*)$  are the density of states for electrons and holes respectively estimated by the well-known parabolic dispersion relationship.

---

<sup>1</sup>Defined in Chapter 3

### 4.2.3 Estimation of device performance

The PV cell works normally on its intrinsic band edge at 300 K, where the regular detailed-balance framework examines the operation property. The solar spectrum absorbed directly by the PV cell and its EL returning to the free-space are given in Eq. (4.7) and Eq. (4.8), respectively.

$$\dot{N}_{s-p}(\epsilon_{ph}) = \frac{2X_{s-p}}{h^3 c^2} \frac{\epsilon_{ph}^2}{\exp[\epsilon_{ph}/k_B T_s] - 1} \quad (4.7)$$

$$\dot{N}_{p-f}(\epsilon_{ph}) = \frac{2X_{p-f}}{h^3 c^2} \frac{\epsilon_{ph}^2}{\exp[(\epsilon_{ph} - qV)/k_B T_{rt}] - 1} \quad (4.8)$$

The total photocurrent also includes those exchanged with the spectrum converter. By running integrals on the photon energy from zero to infinity, the power conversion efficiency (PCE) of the device is then estimated by Eq. (4.9) in a steady state.

$$\eta = \frac{qV \cdot (\dot{N}_{s-p} + \dot{N}_{c-p} - \dot{N}_{p-c} - \dot{N}_{p-f})}{P_{total}} \quad (4.9)$$

## 4.3 A case study for a down-conversion system

It is of interest to explore the down-conversion configuration further (see Figure 3.1 and Ref. [8]), where the absorber and PV cell share the same bandgap  $E_g^c$ . An ultra-high conversion efficiency has been predicted for this configuration [8], due to a higher ability to enforce photon multiplication as indicated in the last chapter.

Carrier multiplication relies on impact ionization in semiconductor materials. However, inevitably thermalization losses will reduce the amount of available energy for the down-conversion in a practical situation. The reciprocal Auger recombination will also consume newly created carriers at the band edge that might become photons flowing to the PV cell, which happens if the carrier extraction rate is not efficient. Hence, the actual working condition of the converter depends on the competition between carrier thermalization, AI and luminescence transfer (optical extraction).

### 4.3.1 Device model configuration

In this example, the legendary front-side down-converter with an ideal planar geometry (see Figure. 3.1) used in Ref. [8] and Chapter 3 will be investigated again. Similar to

the Chapter 3, the details of photonic engineering are ignored here to focus on the carrier dynamics revealed by the RTA model. The detailed photonic environment will be discussed in the next chapter. Consequently, a rectangular window function with particular amplitude and position will be used to describe the optical enhancement imposed by the OESC. Also, both the hot carrier converter and PV cell have an ideal absorptivity/emissivity with a step-like profile, the same one used before. In this configuration, the front converter will absorb all the incident sunlight ( $\dot{N}_{s-p} = 0$ ) and then emit carrier hot-luminescence to pump the back-side PV cell with a matched bandgap [8]. The thickness of the spectrum converter  $d$  is assumed to be 50 nm, a typical number used in previous work on hot carrier solar cells [32, 34, 57]. The optical concentration ratio to the incident sunlight  $R_c$  is set to 1000 times to ensure sufficient amount of hot carrier excitations when thermalization losses exist [29]. All the optical configurations of the system relating to Eq. (4.2) to Eq. (4.7) are summarized in Table 4.1.

Table 4.1: Generalized optical étendues  $X$  and other optical parameters in the front-side down-conversion system with a planar geometry

Name	Sun to converter	Sun to cell	Cell to converter
Symbol	$X_{s-c}$	$X_{s-p}$	$X_0$
Values	$R_c f_s$	0	$\pi$
Name	Converter to free-space	Cell to free-space	Converter to cell
Symbol	$X_{c-f}$	$X_{p-f}$	$X_0$
Values	$\pi$	0	$\pi$
Name	Concentration ratio	Converter thickness [32, 34, 57]	
Symbol	$R_c$	$d$	
Values	1000	50 nm	

The optical enhancement factor  $F_0(\epsilon_{ph})$  in Eq. (4.4) and Eq. (4.5) owns an ideal frequency filter, as shown in Eq. (4.10). The bandwidth of the extraction window is 0.02 eV (corresponding to a quality factor around 30 in the following modelings). To make a good comparison with the result in Ref. [8] and also be compatible with the previous chapter, the optical enhancement factor is further specified as a product based on the material's permittivity  $n_r^2$ , where  $n_r = 3.5$  is the refractive index of the PV cell. This value of  $n_r$  is close to that of both the silicon and GaAs among the interested frequencies below.

$$F_0(\epsilon_{ph}) = \begin{cases} F n_r^2, & E_g^c < \epsilon_{ph} < E_g^c + 0.02\text{eV} \\ 0, & \text{otherwise} \end{cases} \quad (4.10)$$

The electronic parameters are given in Table 4.2. The bandgap of the hot carrier absorber is tuned from 0.4 eV to 1 eV in the modeling. The effective masses of electron ( $m_e^*$ ) and hole ( $m_h^*$ ) are constant at  $0.05m_0$  and  $0.5m_0$  respectively ( $m_0$  is the electron rest mass). These bandgaps and effective masses are similar to many of the III-V hot carrier absorber materials that potentially could be used for hot carrier absorbers [127].

Table 4.2: Electronic parameters used in the front-side down-conversion system

Name	Bandgap of converter	Bandgap of PV cell
Symbol	$E_g^c$	$E_g^p$
Values	[0.4, 1] eV	Same as $E_g^c$
Name	Effective mass of electron	Effective mass of hole
Symbol	$m_e^*$	$m_h^*$
Values	$0.05m_0$	$0.5m_0$
Name	Thermalization lifetime	AI lifetime
Symbol	$\tau_{th}$	$\tau_{ai}$
Values	100 ps	Shown as a ratio of $\tau_{th}/\tau_{ai}$
Name	e-e/h-h scattering coefficient [34]	e-h scattering coefficient [34]
Values	$A = 5 \times 10^{-19}$ kg s/m <sup>3</sup>	$B = 5 \times 10^{12}$ s/m <sup>3</sup>

The hot carrier thermalization lifetime  $\tau_{th}$  for both the electron and hole is assumed to be 100 ps first unless otherwise specified, which is a typical number chosen for electronic hot carrier solar cells in the literature [29, 30, 32, 56]. The AI relaxation time  $\tau_{ai}$  is given as a ratio to  $\tau_{th}$  to reflect the competition between carrier multiplication and thermalization. The highest rate of AI process that will be considered is 200 fs which is a typical timescale for the multiple exciton generation (MEG) process in nano-materials [27, 128–130]. The density dependent elastic mutual scatterings of charge carriers (e-e, h-h, e-h) are considered to be moderate in the material [34], whose relaxation is determined by scattering coefficients via  $\tau_{ee} = A/m_e^*n$ ,  $\tau_{hh} = A/m_h^*n$ , and  $\tau_{eh} = B/n$ ,  $n$  is the density of electrons(holes). All these electronic parameters are also summarized in Table 4.2

The modeling is then initialized with an equilibrium carrier distribution in the hot carrier converter at 300 K. The steady carrier distributions are then solved according to Eq. (4.1).

### 4.3.2 Conversion efficiency and photon gain

The conversion efficiency as a function of the converter’s (PV cell’s) bandgap is given in Figure 4.2. The conversion efficiency calculated in this work is much smaller than the

previous estimations in Ref. [8] due to multiple energy losses. Figure 4.2 clearly shows that the conversion efficiency relies on both the efficient optical extraction and rapid AI processes. The highest efficiency, about 29%, occurs when the bandgap  $E_g^c$  is close to 0.7 eV and both the rate of optical extraction and AI process are at their maximum used in the modeling ( $F = 1000$  and  $\tau_{th}/\tau_{ai} = 500$  respectively). The inset in Figure 4.2 shows that the limiting conversion efficiency of the device occurs when the thermalization loss is tending to be ideally small, and the AI relaxation time  $\tau_{ai}$  is fixed at 200 fs. Significant improvements in device performances appear when the carrier thermalization time  $\tau_{th}$  is longer than nanoseconds, where an upper limit efficiency around 70% can be achieved recovering the prediction in Ref. [8] very well.

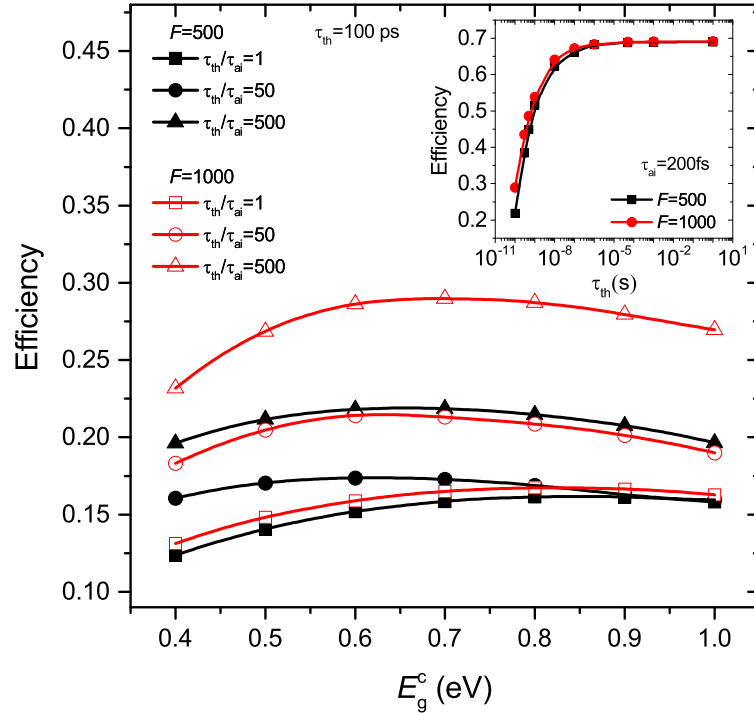


Figure 4.2: Overall conversion efficiency of the OHSC under different bandgaps.  $F$  is an optical emission enhancement factor introduced by the OESC. The carrier thermalization time  $\tau_{th}$  is constant at 100 ps while the relaxation time of AI processes  $\tau_{ai}$  is given as a ratio to  $\tau_{th}$ . The inset shows the efficiency when the thermalization time is sufficiently long and the AI relaxation lifetime is fixed at 200 fs. Over 60% conversion efficiency can be achieved when the thermalization time is similar to 10 ns.

As mentioned in Chapter 3, the general precondition of efficiency enhancement in spectrum conversion systems is an increase in the photocurrent, meaning  $g_J > 1$ . In this down-conversion configuration with ideal absorptions, this condition simply becomes a net gain in photon fluxes before and after the hot carrier spectrum converter ( $g_J \approx \dot{N}_{c-p}/\dot{N}_{s-c} > 1$ ). Figure (4.3) shows the photocurrent gain ratio  $g_J$  of this modeling under different conditions, where the PV cell is always kept in the short-circuit condition (bias

voltage  $V$  is 0 V).

The variation of  $g_J$  with the bandgap  $E_g^c$  shows two major features in Figure (4.3). On the one hand, with a fixed bandgap energy  $E_g^c$  both the fast AI processes and efficient optical extraction can enlarge the transferred photon flux from the converter to the PV cell. In addition to competing with the radiation from the top front-side, known as suppressing the “reciprocal losses” (see Chapter 3), larger  $\tau_{th}/\tau_{ai}$  and  $F$  also win over the thermalization and Auger recombination losses to some degree and improve the quantum yield of carrier hot-luminescence. On the other hand, for a constant rate of carrier multiplication and optical extraction, the bandgap of the converter will modify the maximum optical energy absorbed from the sun, leading to a higher carrier gain ratio when the bandgap is narrower. Similar to the MEG solar cell, a narrow-bandgap material will have a higher particle gain ratio but suffers from a smaller open-circuit voltage [131]. Therefore an optimized efficiency appears when varying the bandgap, as shown in Figure 4.2.

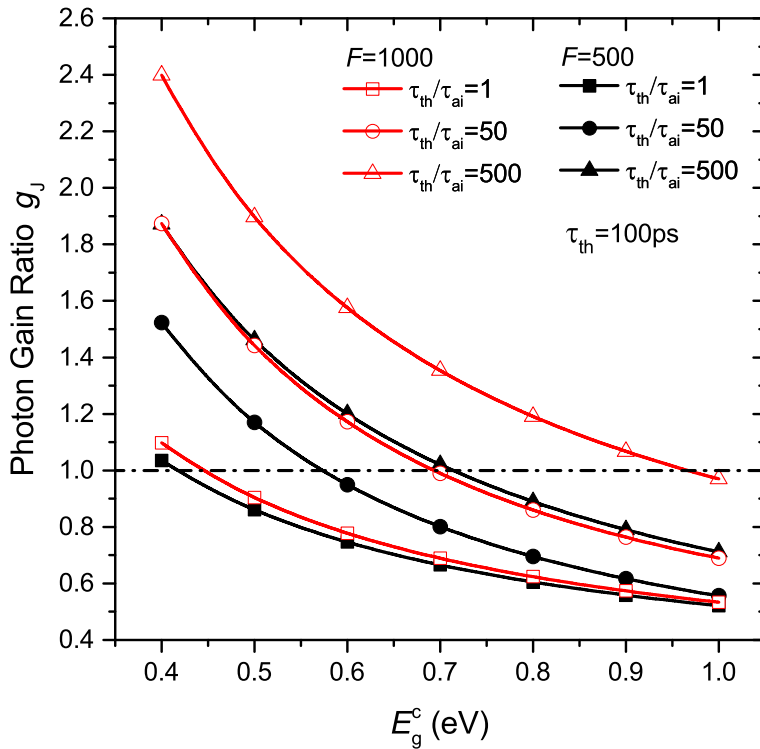


Figure 4.3: Dependence of photon gain ratio on the converter’s bandgap. With an increasing absorber bandgap  $E_g^c$ , the net photon gain reduces and eventually becomes smaller than 1 for all configurations.

A more detailed dependence of the photon gain ratio on both the rate of carrier multiplication and optical extraction is shown in Figure 4.4. The absorber’s bandgap is set at 0.7 eV in this case.

The rate of impact ionization should be comparable with that of thermalization in

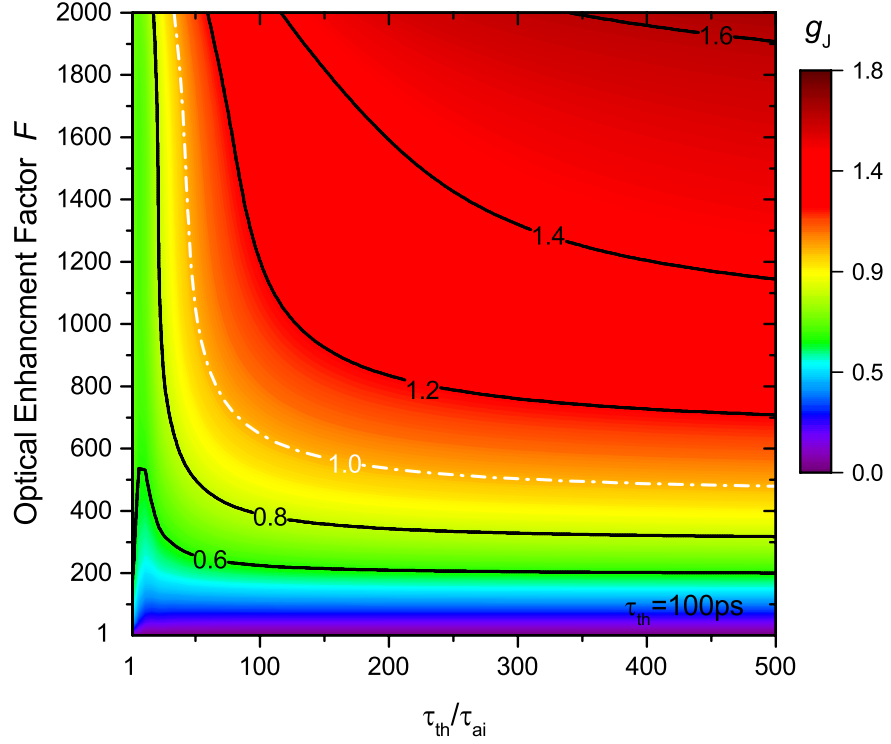


Figure 4.4: The photon gain ratio under different emission enhancements and AI rates. The lifetime of the AI  $\tau_{ai}$  process is presented as a ratio of thermalization time  $\tau_{th}$  of hot carriers. The bandgap is set at 0.7 eV and  $\tau_{th}$  is 100 ps. To get a net photon gain, the required emission enhancement  $F$  should be larger than about 500 and the AI process should be faster than carrier cooling by about 50 times at least.

order to take full advantage of the hot carriers energy. According to Figure 4.4, the ratio  $\tau_{th}/\tau_{ai}$  needs to be at least about 50 to ensure  $g_J > 1$  in this example.

In addition, an active optical enhancement is necessary to extract the carrier hot-luminescence energy in the desired way. It is noted that carriers created by impact ionization may be recombined via Auger recombination before a radiative recombination event. Therefore, only with an efficient carrier extraction can the impact ionization dominate over the Auger process in the final steady state and make the photon gain ratio larger than 1. Otherwise, Auger recombination will cause severe particle losses cooperating with the thermalization of high energy carriers. In this work, the required optical emission enhancement  $F$  must be larger than about 500 times. This is a major requirement for the design of OESC in this down-conversion device. Even when the impact ionization is not competitive with thermalization, for example  $\tau_{th}/\tau_{ai} < 50$ , a rapid optical extraction can also offset the energy loss amount of Auger recombination and thermalization. In the extreme, if optical extraction continuously depletes carriers at the band edge and carrier-carrier scattering is not quick enough to replenish them, more efficient carrier multiplication will be triggered to balance the thermal distribution of charge carriers. This

tendency can be seen in Figure 4.4 when  $F$  approaches 2000.

### 4.3.3 Effect of non-ideal carrier refilling

In most of the cases, a linear dependence between the optical enhancement  $F$  and photon gain ratio  $g_J$  does not exist due to corresponding changes in the thermal state of hot carriers ( $T$  and  $\mu$ ) in each specific steady state. For example, less than a factor of 3 in photocurrent gain is observed when  $F_0$  is varying between 1 and 5000 times in Figure 3.4 of Chapter 3. Another example is in Figure 4.3 above. When  $F$  is increased from 500 to 1000, the actual photon gain does not double but increases by a factor of 1.25 instead with  $\tau_{\text{th}}/\tau_{\text{ai}} = 500$  (triangle symbols in solid-black and empty-red). Only when the carrier occupation function is rigorously the same, is there a linear relationship between  $g_J$  and  $F_0$ .

Further non-linear factors arise when the carrier refilling rate in the extraction window ( $E_g^c < \epsilon_{\text{ph}} < E_g^c + 0.02\text{eV}$ ) is not ideal, such as the finite relaxation lifetimes  $\tau_{\text{ee}}$ ,  $\tau_{\text{hh}}$ ,  $\tau_{\text{eh}}$ ,  $\tau_{\text{ai}}$  used in this RTA model.

According to Eq. (4.3) and Eq. (4.5), we calculate the radiative recombination rate by considering the actual distribution of charge carriers which are established by the real-time competition between multiple dynamic processes. The increase of  $g_J$  with the factor  $\tau_{\text{th}}/\tau_{\text{ai}}$  in Figure 4.3 can also be understood as a result of faster refilling of band edge states via down-conversion. These states would otherwise be depleted continuously by the optical extraction ( $\dot{N}_{\text{c-p}}$ ). In turn, available photon densities in a steady state will be reduced under a large optical extraction rate if the carrier refilling is not fast enough. Since the actual photon emission will also affect the open-circuit voltage  $V_{\text{oc}}$  of the PV cell, a more complex non-linear dependence between the conversion efficiency and  $F$  appears in Figure 4.2

It also suggests the influence of the optical concentration ratio  $R_c$  further. Apart from the power dependent hot carrier dynamics mentioned in Ref. [29] and [8], and that discussed in Chapter 3, a larger incident photon flux can increase the carrier density in the converter and therefore leads to faster rates of e-e, h-h, and e-h carrier scattering in the RTA model [34]. As a result, carrier refillings within the extraction window will be more efficient.

#### 4.3.4 Operation of PV cell

By examining I-V curves of the PV cell in Figure 4.5, further insight into the impact of carrier dynamics on the device performance become visible.

When the AI process is more rapid (i.e., a larger ratio of  $\tau_{th}/\tau_{ai}$ ), the short-circuit current of the cell is significantly increased due to efficient carrier multiplication. However, a decrease in the PV cell's open-circuit voltage  $V_{oc}$  is also evident at the same time.

It is known that the transferred carrier hot-luminescence from the converter  $\dot{N}_{c-p}$  is the only input photocurrent to the PV cell. On the other hand, the intrinsic recombination loss of the PV cell is not changed when varying  $\tau_{th}/\tau_{ai}$  of the converter. Therefore, drops in the  $V_{oc}$  must suggest a decrease in the transferred luminescence which is caused by an enlarged particle loss in the converter.

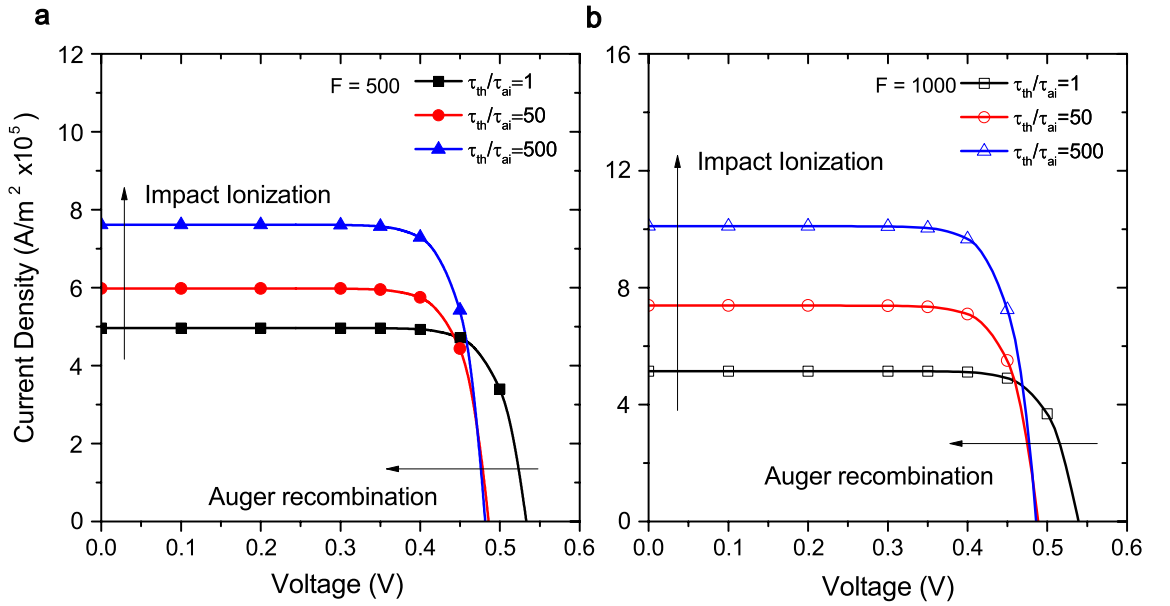


Figure 4.5: I-V curves of the down-conversion optical hot carrier solar cell under 1000-suns. The bandgap is 0.7eV. Two cases with an emission enhancement factor  $F$  of (a)500 times and (b) 1000 times are considered. Both figures show that a rapid AI process in the converter will increase the short-circuit current of the device but decrease the open-circuit voltage due to enlarged Auger recombination losses.

In this down-conversion device, the open-circuit state occurs when the feedback EL is equal to the input carrier hot-luminescence (i.e.,  $\dot{N}_{p-c} = \dot{N}_{c-p}$ ). In other words, the net photon exaction via the OESC becomes zero, which therefore increases the effective dwell time of carriers within the extraction window and also the amount of Auger recombination and thermalization. At the same time, escape radiation from coveter's front surface will increase as well. From the perspective of electrochemical reaction, increasing the residence time of band edge carriers always shifts the steady state of carrier population towards Auger recombination. Such a phenomenon is more evident when the AI processes are

efficient (a smaller  $\tau_{ai}$ ), as shown in Figure 4.5. It is worth noting that Auger recombination will not dissipate carrier energy when no thermalization occurs, like the situation discussed in Chapter 3. As a consequence, hot-luminescence yield will increase with the bias voltage so does the open-circuit voltage there. However, such a phenomenon of “voltage-dependent open-circuit voltage” (see Section 3.3.3) will be weakened in practice since the energy of feedback EL  $\dot{N}_{p-c}$  will partly be dissipated in the converter via carrier thermalizations, or non-radiative relaxations in general.

The above observations also explain another problem that appears in this particular study, that the overall device efficiencies given in Figure 4.1 (when thermalization losses exist) do not go beyond the corresponding single-junction limits under 1000-suns although net gains in photocurrent have been achieved in some cases as shown in Figure 4.3. As has been emphasized several times in Chapter 3,  $g_J > 1$  is a necessary but not sufficient condition to increase the PCE of the device; and the feedback EL from the PV cell is an important factor to be considered further. The enlarged particle losses in the converter near the open-circuit condition reduce the working voltage of the device considerably in this example, which therefore offsets the improvement of the PCE. On the other hand, it requires a larger optical enhancement by the OESC, a more efficient carrier refilling, and also a lower thermalization loss to increase the input photocurrent, and therefore the output power, of the cell.

## 4.4 Discussion

### 4.4.1 Understanding the luminescence emission in the RTA

In order to gain a better understanding, it is necessary to make further comments about the luminescence process in the RTA model.

The luminescence fluxes from the converter are described by Eq. (4.5) and Eq. (4.3). Although detailed parabolic electronic band structures are considered in the RTA model which is characterized by the effective masses of carriers  $m_e^*$ ,  $m_h^*$ , there has no information about the joint density of states (JDOS) or frequency dependent absorption coefficients included in the RTA model.

Actually, a macroscopic far-field luminescence formula is still used in the RTA modeling, which requires the photon occupation function  $f_{ph}$  and the local density of optical states (LDOS) only as shown in Eq. (3.9). The electronic density of states  $\rho_e$ ,  $\rho_h$  appearing in Eq. (4.5) and Eq. (4.3) are used to calculate the  $f_{ph}$ , written as

$$f_{\text{ph}} = \{[\rho_e(\epsilon_e)/n(\epsilon_e) - 1][\rho_h(\epsilon_h)/p(\epsilon_h) - 1]\}^{-1} \quad (4.11)$$

, which are irrelevant to the details of transition dynamics. Also, apart from the optical enhancement factor  $F_0$  introduced by the photonic engineering, Eq. (4.5) and Eq. (4.3) are based on the LDOS of free-space, read from  $\frac{2X_0}{h^3c^2}$ . The electronic band structures will affect the final luminescence yield only via the carrier scatterings and also the carrier occupation functions in the steady state.

Besides, the assumed ideal absorptance with a step-like profile does not contradict with the finite absorption coefficients associated with the detailed electronic band structures, at least in principle, since the optical paths for the absorption could be extended to infinity under perfect light trapping, and vice versa for the light extractions of emission. The above information is then included in the overall absorptivity/emissivity of the component.

#### 4.4.2 Design requirements of the OHCSC

It is interesting to compare the design requirements of OHCSC with and without the appearance of carrier thermalization losses. The major requirements have two aspects: 1) Fast spectrum conversion rate compared to the non-radiative losses; 2) sufficiently large optical enhancement to extract carrier hot-luminescence in time.

The first requirement could be met by choosing proper hot carrier absorber materials with long carrier cooling lifetime and fast impact ionization rate [10]. For the general spectrum conversion material, such as an ion-doped matrix, this requirement corresponds to reduction the non-radiative losses of high-energy dipoles and intermediate transition states. On the other hand, the second requirement above needs a well-designed OESC. According to the results in Figure 4.4, the required optical enhancement factor  $F$  is at least 500 in the example discussed in Section 4.3. However, such an enhancement factor is defined as a multiple of the material's permittivity  $n_r^2 = 12.25$  (see Eq. (4.10)). Hence, the corresponding enhancement factor  $F_0$  respecting to the far-field radiation spectrum is about 6000. This value is much larger than that predicted in Chapter 3 to obtain  $g_J > 1$  because of the large thermalization losses and non-ideal carrier refillings appearing in the RTA example.

The above result also illustrates that although an over-large optical enhancement may be detrimental to the device performance in principle, due to the risk of voltage drop concluded in Chapter 3, pursuing a larger optical enhancement is still the priority in

practice especially for the OHCSC. Instead, some particular spectrum conversion systems can already provide relatively satisfactory luminescence quantum yields based on state-of-the-art techniques [132–135], then the influence of voltage dropping mentioned above has to be carefully examined when performing photonic engineering.

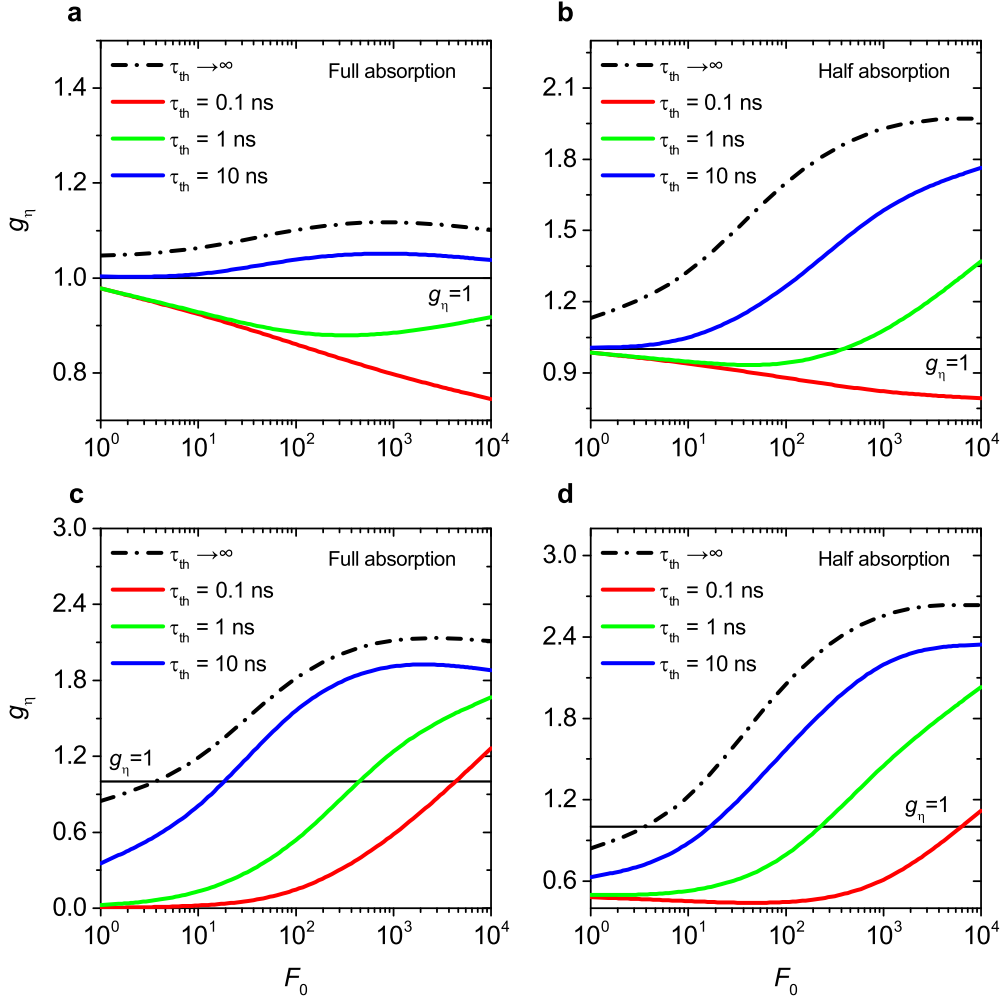


Figure 4.6: The gain ratio of conversion efficiency  $g_n$  modeled by the RTA model with different carrier thermalization lifetimes. The bandgap of spectrum converter is 0.7 eV, while the bandgap of the PV cell is 0.7 eV or 1 eV for down- and up-conversion respectively. (a) Back-side up-conversion with full absorption in each component; (b) Back-side up-conversion with half absorption in each component; (c) Front-side down-conversion with full absorption in each component; (d) Front-side down-conversion with half absorption in each component. The black dot-dash line in each sub-figure shows the results from the detailed-balance model when no thermalization losses occur and carrier refilling rates are ideal.

Figure 4.6 shows more details about the required hot carrier cooling lifetime and optical enhancement in the OHCSC to improve the PCE. The planar-tandem architecture considered in Table 4.1 is continued here. Modeling results from the detailed-balance model are also given as a reference in each case, where carrier populations have an infinitely long thermalization lifetime and ideal refilling rates.

Particularly, both the front-side down-converter (Figure 4.6(a),(b)) and back-side up-converter (Figure 4.6(c),(d)) configurations are modelled, in which the absorptivity of both the converter and PV cell are considered to be 1 (Figure 4.6(a),(c)) and 0.5 (Figure 4.6(b),(d)), respectively. The general optical enhancement ratio  $F_0$  defined in Eq. (4.5) and Eq. (4.4) is directly examined here, with the energy selection profile given in Eq. (4.12). It corresponds to a resonant quality factor of 30 and no frequency filter outside the extraction window, as that examined in Chapter 3. With the 0.7 eV bandgap of the converter  $E_g^c$  already discussed in the previous part of this chapter, the bandgap of the PV cell  $E_g^p$  is chosen to be 1 eV according to the optimization study of energy selective contacts (ESC) previously [136]. A symmetric electronic band structure is considered to improve the overlapping between the electron's and hole's distribution, where both the  $m_e^*$  and  $m_h^*$  are  $0.1m_0$ . To emphasize the impact of carrier thermalization, faster rates of carrier renormalization (ee, hh, eh scatterings) are used here to provide an ideal carrier refillings within the extraction window [34]. Table 4.3 summarizes the parameters used in this modeling.

Table 4.3: Electronic parameters used in the modelings of Figure 4.6

Name	Bandgap of converter	Bandgap of PV cell
Symbol	$E_g^c$	$E_g^p$
Values	0.7 eV	0.7 eV (down-conversion) 1 eV (up-conversion)
Name	Effective mass of electron	Effective mass of hole
Symbol	$m_e^*$	$m_h^*$
Values	$0.1m_0$	$0.1m_0$
Name	Thermalization lifetime	AI lifetime
Symbol	$\tau_{th}$	$\tau_{ai}$
Values	0.1 ns $\sim$ 10 ns	200 fs
Name	e-e/h-h scattering coefficient [34]	e-h scattering coefficient [34]
Values	$A = 5 \times 10^{-21}$ kg s/m <sup>3</sup>	$B = 5 \times 10^{10}$ s/m <sup>3</sup>

$$F_0(\epsilon_{ph}) = \begin{cases} F_0, & E_g^c < \epsilon_{ph} < E_g^c(1 + 1/30) \\ 1, & \epsilon_{ph} > E_g^c(1 + 1/30) \\ 0, & \text{otherwise} \end{cases} \quad (4.12)$$

Clearly, device performance shows evident drops in a more practical consideration shown in Figure 4.6. Roughly speaking, for a down-conversion system, it requires an optical enhancement ratio larger than hundreds of times and a carrier thermalization

lifetime longer than about 500 ps. On the other hand, the up-conversion systems typically require an even longer carrier thermalization lifetime (over nanoseconds) and stronger optical enhancements (over thousand times) to boost the PCE eventually.

### 4.4.3 Summary of dynamic features of device operation

As pointed out in Chapter 3, the optical hot carrier solar cell with OESC is a general representation of a spectrum conversion system with photonic engineering. Several unique features have been identified for this type of device, especially the variation of the working voltage. All these features mainly relate to the carrier dynamics in steady states and electrochemical equilibrium of the converter. The feedback EL from the PV cell also plays a significant role. A summary of some typical features of the OHCSC is given below.

1. After integrating with the hot carrier absorber (spectrum converter) via the OESC, the PV cell still works conventionally at its intrinsic bandgap. Increasing the photocurrent of the cell is a necessary but not sufficient condition to boost the overall PCE, which further asks a sufficiently large optical enhancement in the OESC and long enough carrier thermalization lifetime in the absorber. (Concluded from Chapter 3)

2. If the dipole occupation probability is invariant, the transferred carrier hot-luminescence to the PV cell and the open-circuit voltage of the device will increase with the optical enhancements. (Concluded from Chapter 3)

3. In practice, the steady state occupation probability of radiative dipoles will decrease with the optical enhancement ratio, especially when the carrier refilling is not fast enough. An over-large optical enhancement can be detrimental to the device performance by reducing its open-circuit voltage. (Concluded from Chapter 3 and Chapter 4)

4. When carrier thermalization becomes the dominant spectrum loss mechanism, such as  $\tau_{th} < 500$  ps, pursuing a sufficiently large optical enhancement becomes the priority to increase the luminescence yield whose negative impact in decreasing the voltage is typically negligible now. (Concluded from Chapter 4)

5. Notably, when the spectrum conversion is not ideal with a finite carrier transition rate (such as a large  $\tau_{ai}$ ), a fast luminescence extraction can further shift the electrochemical equilibrium and facilitate the spectrum conversion. (Concluded from Chapter 4)

6. The feedback EL from the PV cell contributes to the phenomenon of “voltage-dependent open-circuit voltage” evidently when the thermalization loss is negligible. This

effect indicates that the actual open-circuit voltage of the device will be larger than its pseudo value  $k_{\text{B}}T_{\text{rt}}/q \cdot \ln(J_{\text{sc}}/J_0)$  estimated at the short-circuit condition. (Concluded from Chapter 3)

7. However, if thermalization loss occurs and the spectrum conversion rate is finite, a strong feedback EL will also prolong the effective residence period of charge carriers inside the converter and therefore enlarge the chance of thermalization losses. In other words, the excitations of the feedback EL cannot be fully used by the converter because of thermalization losses, which causes severe particle losses for the spectrum conversion at the open-circuit condition. (Concluded from Chapter 4)

## 4.5 Conclusion

In this chapter, more practical working principles of the OHCSC are investigated using the RTA model. By using a set of exponential relaxations as approximations, competitions between different carrier dynamics is assessed, and energy losses caused by thermalization and Auger recombination are explicitly taken into account. The device concept still shows potential when subjected to a more practical estimation of its performance, where the long carrier thermalization lifetime and sufficiently large optical enhancement of carrier hot-luminescence extraction are the primary design requirements of this kind of photovoltaic device. Efficient optical extraction is not only able to manage the photon fluxes but also influences the quantum yield of the hot-luminescence and reduces the thermalization loss. More complex device behavior is observed when varying both the optical configurations and electronic properties of the material, where the non-equilibrium steady state of the spectrum converter is critical to an understanding of the device operation.

The down-conversion system is further investigated in detail. The operation of this down-conversion hot carrier device relies on carrier multiplication through impact ionization, which strongly resembles the MEG solar cell substantially. The competition between carrier thermalization and multiplication has already been addressed in the high-efficiency MEG materials before [107, 108]. Efficient optical extraction can further reduce the loss of newly created carriers at the band edge due to Auger recombination and thermalization, as the same design principle for the MEG solar cell. Therefore, the device operating characteristics concluded in this chapter is also valid for an “optical MEG solar cell” as well.



## Chapter 5

# Optical Energy Selective Contact via Near-field Coupling

The previous chapters have discussed the necessity and importance of photonic engineering for an optical hot carrier solar cell (OHCSC) based on a simple planar-tandem device architecture. Particularly, when the hot carrier absorber has continuous electronic energy states, the optical energy selective contact (OESC) also applies frequency selection in addition to luminescence enhancement. The overall target of the OESC is to obtain quasi-monochromatic carrier hot-luminescence with a matched frequency and sufficient intensity to the secondary solar cell in the device.

This chapter will consider a detailed photonic environment and practical realizations of the OESC via a near-field coupling. A rigorous electromagnetic model is introduced and developed to examine the rate of luminescence transfer analytically. It provides physical insight into the photonic dynamics and several useful design/operating principles of this optically-integrated device. Based on the developed framework, a plasmonic core-shell nanowire structure is investigated systematically, showing the general design work-flow of the OHCSC and also the potential of this particular example.

### 5.1 Introduction

Transferring energy by optical coupling in a near-field region is well known in nano-optics and has been widely studied in thermal radiation applications [78]. Such an energy transfer process can be called optical contacting, which is analogous to electrical charge carrier transport via a metallic contact.

This idea is included in the so-called OESC for the OHCSC [8], which aims to achieve an energy-selective hot carrier luminescence coupling by modifying the local density of optical states (LDOS) in the device. Since the OHCSC can be understood as a general spectrum management system, as discussed in Chapter 3, the OESC technique would also be beneficial for the conventional spectrum up/down conversions in photovoltaics.

This optical contacting scheme can also be considered as a general carrier extraction method in optoelectronic. Just as for the energy selection required by the hot carrier solar cell (HCSC), regular conductive contacts may become inapplicable when unusual carrier transport schemes are required. In this case, optical coupling is a promising alternative to avoid complex engineerings in electronic band structures. More generally, it is always challenging to export charge carriers from a nano-structured material efficiently due to its complex surface morphology and quality [137]. Nano-structured semiconductor materials exhibit attractive electronic and optical functionalities including slowed carrier thermalization [46, 47, 138], multiple exciton generations [45, 107, 139] and high photon absorption [23, 140, 141]. However, a reduced electrical conductivity and associated parasitic losses in metallic contacting always limit a full utilization of these functional features in general. Hence, the optical contacting scheme is an inspiring attempt to explore which, however, is lack of comprehensive theoretical tools for further development.

In this chapter, we focus on the near-field luminescence transfer via cavity resonance. By applying a rigorous electromagnetic model, further insight is given into the optical contacting problem. The rest of the chapter is organized as follows. A theoretical model based on the electromagnetic Green's function is introduced first in Section 5.2. Particular attention is paid to obtaining an accurate and self-consistent Green's function using the quasi-normal mode (QNM) method since the optical mode must be lossy and damping in this energy transfer problem. The photon current transferred by the optical contacting can then be examined analytically. In section 5.3, a plasmonic core-shell nanowire structure is given as an example to embody the developed theoretical tools and their applications in photovoltaic analysis. It suggests the effectiveness of optical contacting depends on both the photonic configuration of the system and the hot carrier occupation states in the emitter. The chapter then concludes with further discussions.

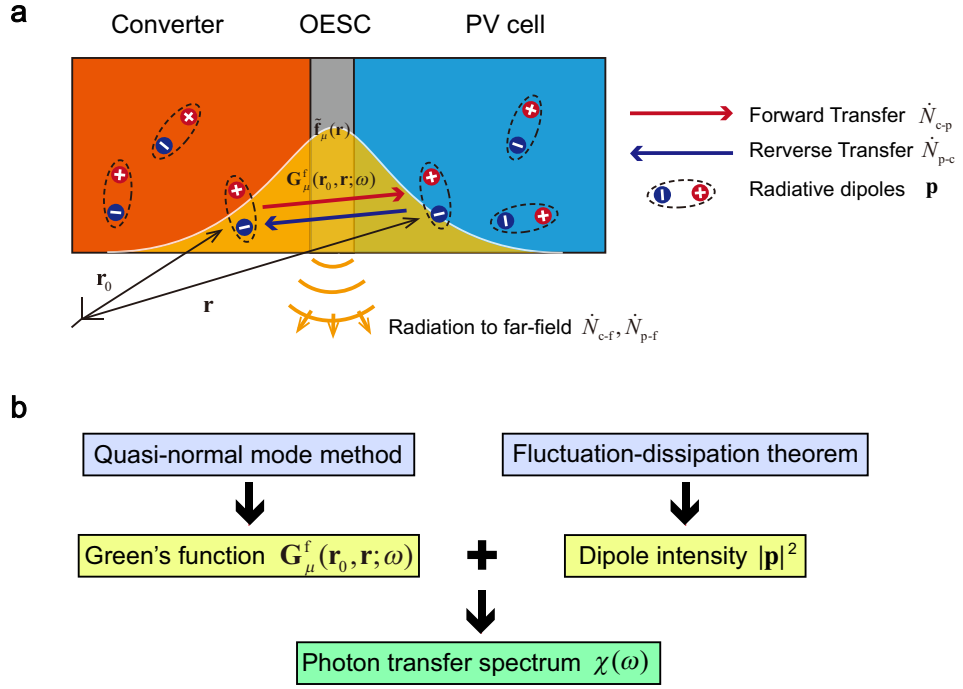


Figure 5.1: (a) Schematic illustration of the optical contacting via an OESC structure and (b) theoretical framework used in the analysis.  $\tilde{\mathbf{f}}_\mu(\mathbf{r})$  is profile the localized resonant mode,  $\mathbf{G}_\mu^f(\mathbf{r}_0, \mathbf{r}; \omega)$  is the corresponding Green's function  $\dot{N}_{c-p}$ ,  $\dot{N}_{p-c}$  denote the luminescence convection between the spectrum converter (“c”) and photovoltaic (PV) cell (“p”), while  $\dot{N}_{c-f}$ ,  $\dot{N}_{p-f}$  mean the far-field radiation back to free-space (“f”). The LDOS is increased around the central resonant frequency in this system which facilitates the optical energy exchange. Parts of the energy may also escape to the far-field resulting in power loss.

## 5.2 Theoretical model of luminescence transfer

This section summarizes the basic theoretical tools and formulas used in the optical analysis of the OESC. These formulae are not only necessary to understand the near-field luminescence transfer but can also be used as a general method to analyze the optical behavior of photovoltaic devices. For more background on control of spontaneous emission, please refer to section 2.3.1 of Chapter 2.

Figure 5.1 gives a general schematic illustration of the luminescence transfer process via an OESC structure between a spectrum converter and PV cell. These two active components are physically close but electrically isolated from each other. Localized optical resonant modes  $\tilde{\mathbf{f}}_\mu$  are introduced by the OESC, such as the cavity mode with modal index  $\mu$ , which penetrates into both the converter and PV cell simultaneously to deliver optical energy. The resonance enforces the frequency selection naturally. It is not necessary to place the OESC equidistant from the converter and PV cell. The only criterion is that the same resonant mode should couple both components.

The theoretical framework consists of two fundamental elements, which are the dyadic

electric Green's function<sup>1</sup>  $\mathbf{G}(\mathbf{r}, \mathbf{r}_0; \omega)$  over coupling volumes and the average radiative dipole density  $\mathbf{p}(\mathbf{r}_0; \omega)$  in the luminescence emitter. The dipole density defines the source intensity of photon emissions, while the Green's function indicates the establishment and propagation of electromagnetic fields in a certain photonic environment. Then the excited electric field  $\mathbf{E}$  can be written as Eq. (5.1) using the volume-integral method [65]. The symbolic and formula conventions of electromagnetics used in this thesis are given in Appendix A.

$$|\mathbf{E}(\mathbf{r}; \omega)|^2 = \frac{1}{\varepsilon_0^2} \iint_V d\mathbf{r}_1^3 d\mathbf{r}_2^3 G_{im}(\mathbf{r}, \mathbf{r}_1; \omega) p_{mn} G_{in}^*(\mathbf{r}, \mathbf{r}_2; \omega) \quad (5.1)$$

In the above equation,  $\varepsilon_0$  is the permittivity in vacuum,  $V$  is the integral volume over the field emitter,  $G_{ab}$  is the tensor component of the  $3 \times 3$  dyadic Green's function  $\mathbf{G}$  with subscript indexes  $a$  and  $b$ , while the superscript “\*” means its corresponding complex conjugation. Einstein's sum rule should run over all the indices  $i$ ,  $m$  and  $n$  in orientation and polarization. Similarly, the symbol  $p_{ab} = \langle p_a p_b^* \rangle$  denotes the correlative dipole intensity between any two arbitrary polarizations  $a$  and  $b$ , in which  $p_a$  is the vector component of the  $1 \times 3$  dipole moment  $\mathbf{p}$  in the direction  $a$ . When the media is isotropic without any off-axis correlations,  $p_{ab}$  is then reduced to the regular dipole intensity  $|\mathbf{p}|^2$  defined by the inner product.

To evaluate the optical field intensity and associated optical power, the corresponding Green's function  $\mathbf{G}_\mu^f$  and average dipole intensity  $|\mathbf{p}|^2$  have to be determined first. Further explanation of these two essential elements is given below.

### 5.2.1 Green's function evaluation using quasi-normal mode method

Evaluating an accurate and self-consistent Green's function is always challenging in the research of nano-optics, especially in a damping resonant system caused by either local absorptions or far-field radiation [90]. Since the convection and absorption of luminescence are essential to the optical contacting problem discussed here, the inevitable damping of the optical modes has to be considered. To solve this problem, the quasi-normal mode (QNM) method is used here to calculate the numerical Green's function of the cavity mode in a semi-analytical way [90, 92, 93, 97, 98].

The QNM is the natural solution of Maxwell's equation in a leaky resonant system. The normalized QNM by a unique formalism can be used to construct an accurate and

---

<sup>1</sup>All the Green's function  $\mathbf{G}$  used in this thesis are defined between the electric dipole moment and electric field only, see Appendix A

self-consistent Green's function close to the lossy resonator, both inside and outside

In this method, the mode profile function  $\tilde{\mathbf{f}}_\mu(\mathbf{r}; \omega_\mu)$  at resonant frequency  $\omega_\mu$  is computed numerically via finite-difference time-domain (FDTD) simulations first. A specially designed time-domain windowing function applies to obtain the QNM accurately. After mode normalization, the Green's function of this resonant mode is then constructed by a modified mode expansion technique [65]. It could be written as  $\mathbf{G}_\mu^f(\mathbf{r}_1, \mathbf{r}_2; \omega) \equiv W(\omega, \omega_\mu) \left[ \tilde{\mathbf{f}}_\mu(\mathbf{r}_1; \omega_\mu) \otimes \tilde{\mathbf{f}}_\mu(\mathbf{r}_2; \omega_\mu) \right]$  in general, where function  $W(\omega, \omega_\mu)$  introduces a frequency dependent spectrum profile near the central resonant frequency  $\omega_\mu$ . For more detail about the FDTD modeling, please refer to section 2.3.2 of Chapter 2.

It has been proved that the QNM method is a reliable approach when analyzing the LDOS of lossy cavity modes, where the traditional Purcell formula typically fails [90–93, 97, 98]. For more details about the physical background, simulation method and Green's function construction of the QNM, please see Appendix A.

### 5.2.2 Dipole density evaluation via fluctuation-dissipation theorem

The ensemble-averaged dipole intensity  $p_{mn}$  used in Eq. (5.1) can be predicted by the fluctuation dissipation theorem (FDT) in a thermo-equilibrium condition. In an isotropic medium with only local response,  $p_{mn}$  is given as below [78]

$$p_{mn} = \langle p_m p_n^* \rangle = \frac{4}{\pi\omega} \Theta(T, \mu) \varepsilon_0 \varepsilon''(\mathbf{r}_1; \omega) \delta_{mn} \delta(\mathbf{r}_1 - \mathbf{r}_2) \quad (5.2)$$

Eq. (5.2) demonstrates a detailed-balance between the optical absorption and emission in thermal-equilibrium. In the above equation, the imaginary part of the dielectric function  $\varepsilon = \varepsilon' + i\varepsilon''$  describes the optical dissipation in the material, which in turn relates to the dipole excitation density. This formula is an essential element often used in the thermal radiation problem [78, 80] and can also apply to semiconductor photoluminescence [142], since the radiative interband transition of charge carriers dominates the dielectric function of a semiconductor near its band edge. Function  $\Theta(T, \mu)$  above is the average energy of radiative dipoles. It is characterized by the ensemble-averaged temperature  $T$  and electrochemical potential  $\mu$  in Bose-Einstein statistics as shown in Eq. (5.3), where  $k_B$  is the Boltzmann's constant. It is noted that  $T$  is NOT the physical temperature of the material (always at 300 K) but the thermodynamic parameter of the radiative dipoles inside. In the hot carrier absorber,  $T$  and  $\mu$  are for the electron-hole pairs formed in the hot carrier population.

$$\Theta(T, \mu) = \frac{\hbar\omega}{\exp[(\hbar\omega - \mu)/k_{\text{B}}T] - 1} \quad (5.3)$$

It is worth noting that the FDT is essentially compatible with the conventional framework of photovoltaic analysis. By substituting the dipole intensity predicted by Eq. (5.2) into the familiar dipole radiation formula in Eq. (5.4), we can reproduce the van Roosbroeck-Shockley's luminescence formula (see Chapter 3) with a prefactor of 1/3, where  $n_{\text{r}}$  is the real refractive index of the medium (complex index written as  $\tilde{n}=n_{\text{r}}+i\kappa$ ) while the imaginary dielectric function has been replaced by the material's absorption coefficient with a proper coefficient  $\varepsilon'' = 2n_{\text{r}}\kappa = \alpha c n_{\text{r}}/\omega$ . The prefactor 1/3 denotes the orientational average in an isotropic photonic environment which will disappear once the Eisenstein's sum rule has run over all the directional indices.

$$P = \frac{|\mathbf{p}|^2}{12\pi} \frac{\omega}{\varepsilon_0} \frac{\omega^3 n_{\text{r}}}{c^3} d\omega = \frac{1}{3} \frac{n_{\text{r}}^2}{\pi^2 c^2 \hbar^3} \alpha(\hbar\omega) \frac{(\hbar\omega)^3}{\exp[(\hbar\omega - \mu)/k_{\text{B}}T] - 1} d\hbar\omega \quad (5.4)$$

### 5.2.3 Luminescence transfer spectrum

With the local electric and magnetic fields  $\mathbf{E}$  and  $\mathbf{H}$ , the transferred luminescence energy due to the local absorptions and far-field radiations are then written as below

$$\dot{Q}_{\text{e-r}}(\omega) = \frac{\omega\varepsilon_0}{2} \int_{V_{\text{r}}} d\mathbf{r}^3 \varepsilon_{\text{r}}''(\mathbf{r}; \omega) \cdot |\mathbf{E}(\mathbf{r}; \omega)|^2 \quad [\text{Near-field local absorption}] \quad (5.5)$$

$$\dot{Q}_{\text{e-f}}(\omega) = \frac{1}{2} \int_{S_0} d\mathbf{r}^2 \hat{\mathbf{n}} \cdot \text{Re} \{ \mathbf{E}(\mathbf{r}; \omega) \times \mathbf{H}^*(\mathbf{r}; \omega) \} \quad [\text{Far-field radiation}] \quad (5.6)$$

In the above equations, the subscript “e-r” denotes the optical power emitted by an emitter (“e”) and reabsorbed by another receiver (“r”) while “e-f” means the radiation to the far-field (or free-space) (“f”). The imaginary part of the receiver's dielectric function  $\varepsilon_{\text{r}}''$  is used in Eq. (5.5) to evaluate the local absorption rates, and the spatial integral run over the receiver's volume  $V_{\text{r}}$ . Instead,  $S_0$  and  $\hat{\mathbf{n}}$  in Eq. (5.6) denotes the outer surface of the whole device and out-going surface vector respectively. An extra absorptance needs to be considered in Eq. (5.6) if the far-field receiver cannot absorb all the luminescence.

By substituting Eq. (5.1) ~ Eq. (5.3) into Eq. (5.5) and Eq. (5.6), we can finally represent the transferred power in Eq. (5.7) and Eq. (5.8). In order to analyze the impact of photonic engineering and the emitter excitation separately, the transferred power is further

represented by a product of photon transfer spectrum  $\chi(\omega)$  and dipole occupation function  $\Theta_e(T_e, \mu_e)$ . The analytical formulae of  $\chi(\omega)$  via a certain optical mode (characterized by Green's function  $G_{ab}$ ) are given in Eq. (5.9) and Eq. (5.10)

$$\dot{Q}_{e-r}(\omega) = \chi_{e-r}(\omega)\Theta_e(T_e, \mu_e) \quad (5.7)$$

$$\dot{Q}_{e-f}(\omega) = \chi_{e-f}(\omega)\Theta_e(T_e, \mu_e) \quad (5.8)$$

$$\chi_{e-r}(\omega) = \frac{2}{\pi} \int_{V_r} d\mathbf{r}^3 \varepsilon_r''(\mathbf{r}; \omega) \int_{V_e} d\mathbf{r}_0^3 G_{im}(\mathbf{r}, \mathbf{r}_0; \omega) \varepsilon_e''(\mathbf{r}_0; \omega) G_{im}^*(\mathbf{r}, \mathbf{r}_0; \omega) \quad (5.9)$$

$$\begin{aligned} \chi_{e-f}(\omega) = & \frac{2c^2}{\pi\omega^2} \int_{S_0} d\mathbf{r}^2 \hat{\mathbf{n}}(\mathbf{r}) \cdot \varepsilon_{ijk} \\ & \times \text{Re} \left\{ i \int_{V_e} d\mathbf{r}_0^3 G_{jm}(\mathbf{r}, \mathbf{r}_0; \omega) \varepsilon_e''(\mathbf{r}_0; \omega) [\nabla \times \mathbf{G}(\mathbf{r}, \mathbf{r}_0; \omega)]_{km}^* \right\} \end{aligned} \quad (5.10)$$

The above four equations are the central conclusion of this section. In these equations, all the variables with a subscript “e” mean that of the photon emitter while the subscript “r” means photon receiver; a Levi-Civita tensor  $\varepsilon_{ijk}$  is used in  $\chi_{e-f}(\omega)$  as a shorthand of cross-product in the Poynting vector. Also, the Einstein sum rule should run over all the orientation and polarization indices  $i, j, k$ , and  $m$ .

The photon transfer spectra  $\chi(\omega)$  act as transfer functions for the luminescence, whose unit is the photon number per unit time per unit energy. It defines the effectiveness of luminescence coupling between an arbitrary emitter (“r”) and receiver (“e”) pair at frequency  $\omega$  and is determined by the photonic configuration of the system only. By using the material ( $\varepsilon_e'', \varepsilon_r''$ ) and geometric parameters ( $V_r, V_e, S_0$ ) of the real device,  $\chi(\omega)$  includes the intrinsic emissivity of the emitter providing the dipole occupation probability is unity inside. Similarly, it also includes the intrinsic absorptance of the receiver by ignoring any absorption quenching/bleaching effect due to carrier occupations. Maximizing  $\chi_{e-r}(\omega)$  between the spectrum converter and PV cell at the cell's bandgap frequency is the primary design principle of a near-field OESC while increasing the intensity of  $\chi_{e-f}(\omega)$  is necessary in the far-field coupling case.

On the other hand, the occupation function  $\Theta_e$  introduces the actual availability of radiative dipoles. Overall, the total transferred power  $\dot{Q}$  and corresponding photon current

$\dot{N}$  can be further written as Eq. (5.11).

$$\dot{Q} = \int_0^\infty d\omega \dot{Q}(\omega) ; \quad \dot{N} = \int_0^\infty d\omega \frac{1}{\hbar\omega} \dot{Q}(\omega) \quad (5.11)$$

### 5.3 Optical contacting by a plasmonic core-shell nanowire

This section considers the near-field luminescence coupling inside a plasmonic core-shell nanowire structure based on the theoretical tools developed above. Use of a plasmonic nanowire to enhance the photon emission, especially the carrier hot-luminescence, has been verified for both direct and indirect bandgap semiconductors [64, 73]. Several thousand times of local field enhancement has been reported in this kind of structure due to the surface plasmon resonance where the yield of photoluminescence increases significantly. It is, therefore, interesting to consider a near-field coupling system by integrating both the PV component and spectrum converter into the same plasmonic core-shell nanowire. The tunable plasmonic resonance is then expected to enhance the luminescence transfer at selected frequencies just as that required by the OESC. It is noted that this plasmonic core-shell nanowire structure is an example for application of the theoretical analysis developed above. Other potential structures to implement the OESC will be discussed in section 5.5 and Chapter 7.

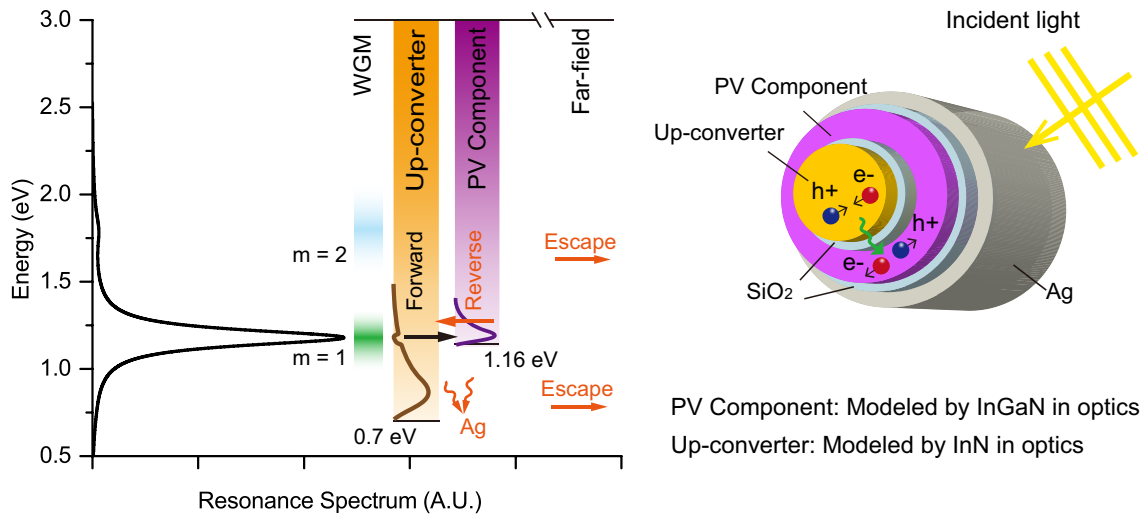


Figure 5.2: A plasmonic core-shell nanowire structure is acting as an OESC device. Left side: the resonance spectrum of WGMs resulted from SPPs is overlaid with a schematic illustration of the optical energy band configuration of the device. The arrows label all the energy flows in the structure. The  $m = 1$  WGM acts as a coupling channel to facilitate the carrier hot-luminescence transfer from the up-converter (0.7 eV bandgap) to the band edge of the PV component around 1.16 eV. Right side: Schematic illustration of the plasmonic core-shell nanowire. The up-converter is modeled by InN in optics while  $\text{In}_x\text{Ga}_{1-x}\text{N}$  with a bandgap of 1.16 eV models the PV component.

### 5.3.1 Whispering-gallery mode of plasmonic nanowire

The plasmonic core-shell nanowire supports a series of whispering-gallery-modes labeled by the azimuthal index  $m$ , whose resonant frequency can be tuned by the diameter of the wire. These non-propagating whispering-gallery-mode (WGM) appears around the lower cut-off frequencies of the plasmonic guiding mode [64, 143]. The multiple interferences of surface plasmon polaritons (SPPs) traveling along the azimuthal direction of the wire lead to a finite mode extension length along the wire's long axis [143]. Hence, a quasi-2D approximation applies in the following discussion.

In this example, we consider a spectrum up-converter providing a hot carrier population with an ensemble-averaged temperature  $T_c > 300$  K. We intend to couple the emitted carrier hot-luminescence to a nearby PV component for further photovoltaic conversion, as shown in Figure 5.2. A brief optical energy band configuration is also given on the left side of Figure 5.2, where the orange and purple block denotes the absorbing energy range of the up-converter and PV component, respectively. The dark curves inside represent the carrier distributions with different temperatures. Both the luminescence emission and absorption are expected to be amplified around the resonant frequency of plasmonic WGM.

A low-bandgap up-conversion material makes the core-wire with a diameter of 60 nm, whose dielectric function is modeled by that of InN. Then, a 20 nm outer-layer acts as the PV component with a larger bandgap, whose dielectric function is modeled by that of  $\text{In}_x\text{Ga}_{1-x}\text{N}$ . InN and  $\text{In}_x\text{Ga}_{1-x}\text{N}$  are selected here to represent typical direct bandgap materials used as spectrum converter and PV component with suitable bandgap energies which are about 0.7 eV and 1.16 eV ( $x = 0.65$  [144]) respectively. The whole wire is then coated by a silver shell (5 nm thick) to introduce SPPs, which can penetrate into both the up-converter and PV component. Two partitioning layers of  $\text{SiO}_2$  (5 nm thick each) are also included in the wire to insulate all active components from each other. Therefore, the optical coupling is the only way of energy exchange in this system. Also, no hot electron emission from the silver shell is taken into account, only the luminescence from the up-converter and PV component is considered. All the dielectric functions of modeled materials here are cited from literature (InN [145],  $\text{In}_x\text{Ga}_{1-x}\text{N}$  [144],  $\text{SiO}_2$  [146] and Ag [147]) assuming they are isotropic and homogeneous.

The above geometric sizes just align the dipole-like WGM ( $m = 1$ ) to the band edge of the PV component (1.18 eV), which enables a quasi-monochromatic excitation of the photovoltaic conversion and avoids the thermalization losses in the PV component. The

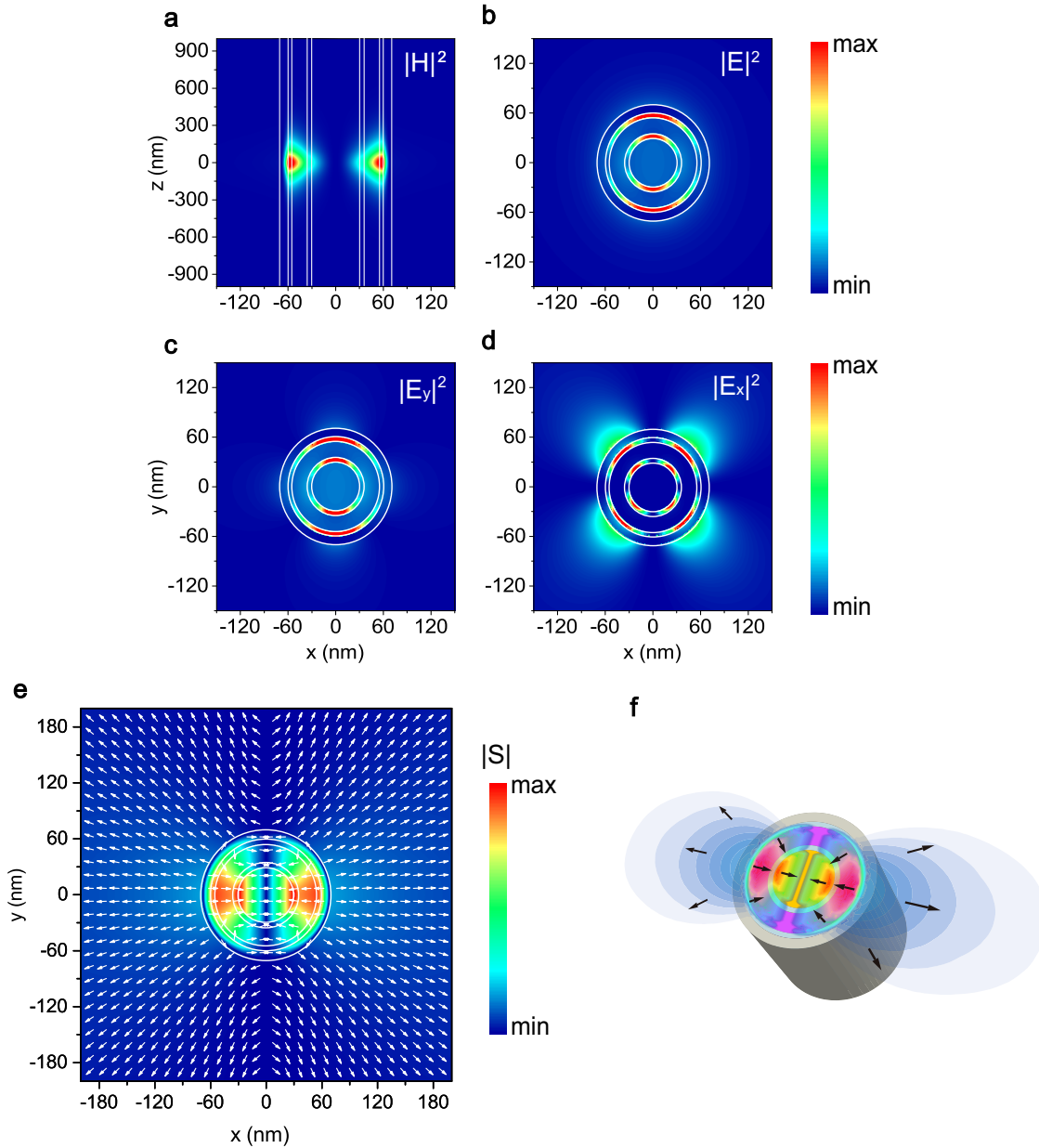


Figure 5.3: Normalized mode profile of the  $m = 1$  WGM used as the optical coupling channel. (a) Magnetic field intensity along  $z$ -direction; (b)-(d) electric field intensity in the cross sectional plane; (e) Poynting vector in the cross sectional plane; (f) Poynting vector field shown on the nanowire model

mode profiles around the wire are given in Figure 5.3 (a)-(d), which shows a mode extension length in the  $z$ -direction of about 250 nm. The corresponding quality factor  $Q$  of this dipole-like mode is about 9.14, which means that the effective bandwidth, i.e., the full-width-at-half-maximum (FWHM), of the carrier hot-luminescence is about 0.129 eV. It is noted that such a bandwidth is acceptable for an electrical energy selective contacts (ESC) to extract hot carriers [57]. Since the large absorption of semiconductor components leads to a fast damping of the resonance, the contributions from highly ordered ( $m > 1$ ) WGMs

are ignored. Actually, the second ordered mode ( $m = 2$ ) is about 0.5 eV away from the dipole-like mode with a much smaller intensity ( $Q \approx 1$ ). Also, the emissivity of hot-luminescence is further reduced by a much lower occupation probability  $\Theta$  of hot carriers at those higher energies.

Parts of the optical energy will also escape to the far-field or be absorbed by the Ag shell. These energy flows are labeled as red arrows in Figure 5.2(a), which corresponds to unavoidable energy losses in this single plasmonic nanowire structure. All those energy flows and corresponding photon currents can be explicitly calculated by Eq. (5.7) ~ Eq. (5.11) with the Green's function of the  $m = 1$  WGM  $\mathbf{G}^{\text{WGM}}$  evaluated by the QNM method (Appendix A).

To verify the accuracy of QNM analysis, we compare the in-plane LDOS enhancement  $F_n$  from the Green's function  $\mathbf{G}^{\text{WGM}}(\mathbf{r}, \mathbf{r}; \omega)$  to the result of the full dipole FDTD simulation [93, 95]. By using the Green's function,  $F_n$  can be analytically written as  $F_n = \frac{\text{Im}\{\hat{\mathbf{n}} \cdot \mathbf{G}^{\text{WGM}}(\mathbf{r}, \mathbf{r}; \omega) \cdot \hat{\mathbf{n}}\}}{\text{Im}\{\hat{\mathbf{n}} \cdot \mathbf{G}^{\text{B}}(\mathbf{r}, \mathbf{r}; \omega) \cdot \hat{\mathbf{n}}\}}$ , where  $\mathbf{G}^{\text{B}}$  is the background Green's function in free space which has  $\text{Im}[G^{\text{B}}(\mathbf{r}, \mathbf{r}; \omega)] = \omega^2/8c^2$  in the 2D space and  $\text{Im}[G^{\text{B}}(\mathbf{r}, \mathbf{r}; \omega)] = \omega^3 n_r/6\pi c^3$  in the 3D space. On the other hand, the full dipole simulation naturally includes all the optical modes existing at the dipole's location and gives the numerically exact result of  $F_n$  with no approximations (averaged over the mesh grid volume [96]). Two sets of simulations are made with the dipole's locations both inside (Figure 5.4(a)) and outside (Figure 5.4(b)) the nanowire. In both cases, the electric dipole is placed 20 nm away from the outer surface of the Ag shell with a polarization as shown in the insets of Figure 5.4.

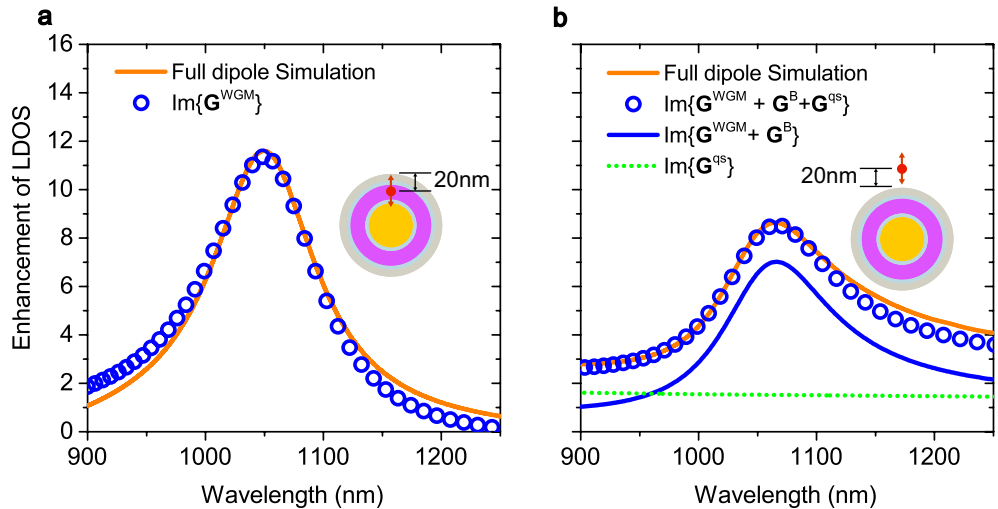


Figure 5.4: The enhancement of in-plane LDOS calculated by the Green's function via QNM analysis and full dipole simulation result. The insert shows the location and polarization of the source for the LDOS calculation.

In both cases, the analytical method gives reasonably accurate results in both the intensity and spectrum profile of  $F_n$ . It attests to the accuracy and self-consistency of  $\mathbf{G}^{WGM}$  evaluated by the QNM method. Particularly, when the dipole is outside the cavity, the contributions from free-space Green's function  $\mathbf{G}^B$  and the quasi-static response of the Ag surface  $\mathbf{G}^{qs}$  have to be taken into account [92]. Then, the total Green's function outside the wire should be  $\mathbf{G}^{WGM} + \mathbf{G}^B + \mathbf{G}^{qs}$ . The Ag's quasi-static response is examined using another full dipole FDTD simulation by putting a dipole source with the same polarization (p-polarized) and distance to a semi-infinite Ag's surface.

### 5.3.2 Photon transfer spectra

Based on the Green's function  $\mathbf{G}^{WGM}$  evaluated in the previous section, the photon transfer spectra associated with different emitter-receiver pairs ("e-r") in the wire are calculated in Figure 5.5. We still follow the same symbolic system used in Chapter 3 to represent the luminescence conventions, where the subscript "c", "p", "s", "f" denote the converter, PV cell, the sun and far-field free-space, respectively. Particularly, we also need to consider the parasitic absorption of silver in this example, which is represented by the subscript "Ag".

Figure 5.5(a) and (c) show the forward transfer process as that labeled in Figure 5.2 where the up-converter acts as the luminescence emitter ( $\dot{N}_{c-c}$ ,  $\dot{N}_{c-p}$ ,  $\dot{N}_{c-Ag}$ ,  $\dot{N}_{c-f}$ ). Instead, the PV component is considered as the emitter in Figure 5.5 (b) and (d) to show the reverse transfer process ( $\dot{N}_{p-c}$ ,  $\dot{N}_{p-p}$ ,  $\dot{N}_{p-Ag}$ ,  $\dot{N}_{p-f}$ ). All of the calculated spectra are strongly peaked around the resonant energy owing to the selective enhancement of WGM resonance. It is noted that the spectra  $\dot{N}_{c-p}$  and  $\dot{N}_{p-c}$  are the same with each other as expected since they are the extract reciprocal transfer channels to couple the carrier hot-luminescence.

The far-field coupling spectrum with a planar geometry is considered as a reference to quantify the enhancement in photon transfer. First, the photon current spectrum in free space [115] is written as  $\chi(\omega)_{\text{free}} = \omega^2 \sigma / 4\pi^2 c^2$ , where the factor  $\sigma$  is the geometric cross-section of the nanowire, i.e., the wire's diameter here, given as the black dot dash in Figure 5.5(c) and (d). Then, an additional thin-film absorptivity (emissivity)  $a$  with the same thickness used in this model for each component is added in. The actual absorbed (emitted) photon spectrum and the corresponding mutual transfer spectrum are then given as  $N(\omega)_{\text{free}} a_p$  (green dot-dash line in Figure 5.5(c)),  $N(\omega)_{\text{free}} a_c$  (blue dot-dash line in Figure 5.5(d)), and  $N(\omega)_{\text{free}} a_p a_c$ , respectively.

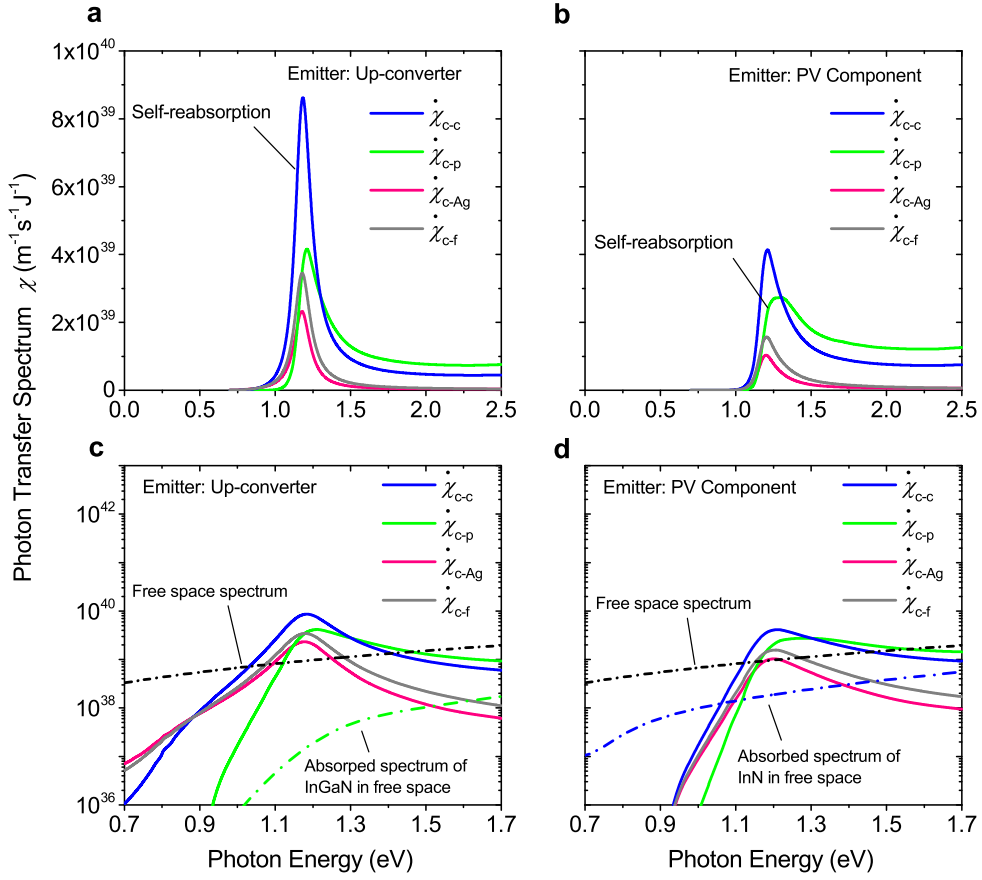


Figure 5.5: Photon transfer spectra in the cross sectional plane of the core-shell plasmonic nanowire. (a) and (c) show the result when the up-converter act as the luminescence emitter, where  $\dot{N}_{c-c}$ ,  $\dot{N}_{c-p}$ ,  $\dot{N}_{c-Ag}$ ,  $\dot{N}_{c-f}$  are the spectra absorbed by the converter itself (self-reabsorption), PV component, Ag and escaping to the far-field (back to free-space) respectively; (b) and (d) show the result when the PV component act as the luminescence emitter, where  $\dot{N}_{p-c}$ ,  $\dot{N}_{p-p}$ ,  $\dot{N}_{p-Ag}$ ,  $\dot{N}_{p-f}$  are the spectra absorbed by the converter, PV component itself (self-reabsorption), Ag and escaping to the far-field (back to free-space) respectively. The free space photon current spectrum  $\dot{N}(\omega)_{\text{free}}$  and those absorbed by the active materials are given as references.

Figure 5.5(c) shows that the absorption of PV component via the WGM is increased by a factor of about 240 times around the resonant peak in the core-shell nanowire structure. The absorptance and also the emissivity of the up-converter are enlarged by about 20 times compared to their far-field counterparts, given by Figure 5.5(d). Therefore, the total increment ratio in the mutual transfer spectrum  $\chi(\omega)_{c-p}$  is about 4800 times than that of the far-field planar setup.

Four aspects are discussed here to show further insight into the transfer spectra.

First, self-reabsorption effects are observed in Figure 5.5, corresponding to photon recycling in each component via the WGM. This reabsorption effect results from the excited electric fields distributing inside the emitter's volume, which rises in a natural way when both the emitter and receiver are the same component in Eq. (5.9) ( $\dot{N}(\omega)_{c-c}$ ,

$N(\omega)_{\text{p-p}}$ ). The stronger self-reabsorption of the lower-bandgap up-converter comes from its larger absorption coefficient near the resonant frequency. Such a photon recycling effect is undesirable in the side of spectrum converter, since it may allow more parasitic losses in a practical situation by increasing the effective residence time of hot carriers in the converter (concluded in Chapter 4). However, a large  $\chi(\omega)_{\text{p-p}}$  is helpful to keep a higher working voltage of the PV component.

Second, increasing the relative penetration of electric fields into the PV component by an optimized photonic design could reduce the amount of photon recycling inside the spectrum converter. Considering the evanescent nature of the SPPs, a smaller refractive index of the PV component than that of the spectrum converter is suggested [85] in this kind of plasmonic optical contact. However, a lower emission enhancement of the carrier hot-luminescence will occur at the same time in principle because of the reduced local field enhancement in the converter. A careful trade-off must be applied when changing the material's indices in the device.

Third, the actual directionality of the luminescence convention between the up-converter and PV components is determined by their dipole occupation functions  $\Theta(T, \mu)$  around the coupling channel, i.e.,  $\dot{N}_{\text{c-p}} [\Theta_{\text{c}}(\omega) - \Theta_{\text{p}}(\omega)]$ , which therefore varies with the working voltage of the PV component.

Finally, several inherent loss mechanisms also need to be addressed. The radiation losses to the far-field are considerable in this single wire picture because of a finite local absorption and field confinement. Such a loss can probably be reduced in a large array of wires, where the escaped radiations could be reabsorbed by other wires again. The absorption caused by the Ag, or the surface plasmon provider in general, is likely to be inevitable in this plasmonic system.

### 5.3.3 Carrier temperature dependent luminescence transfer

The influences from the thermodynamic state  $\Theta_{\text{c}}(T_{\text{c}}, \mu_{\text{c}})$  of the converter are now discussed. As in the analogy used in previous chapters, a hot carrier population with a temperature  $T_{\text{c}}$  higher than 300 K is used to simulate the up-conversion process. It is noted that the physical temperature of the device is always at 300 K.

Figure 5.6(a) shows the temperature dependent carrier hot-luminescence currents (in units of charge current) emitted by the up-converter. In this calculation, the carrier temperature in the converter varies from 300 K to about 3000 K while the electrochemical

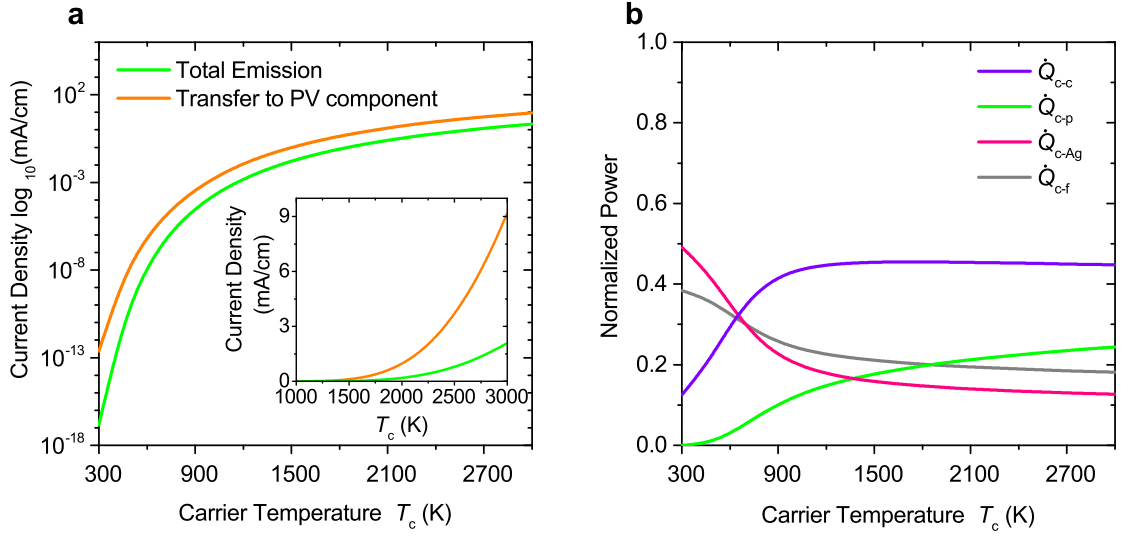


Figure 5.6: (a) The transferred photon current density per unit length of the nanowire by InN for different carrier temperatures; (b) The normalized power transferred from InN at different carrier temperatures.

potential  $\mu_c$  stays at zero [8]. The difference between the total emitted photocurrent and that transferred to the PV component comes from the contributions of the converter's self-reabsorption, Ag's parasitic absorption and also the far-field radiation.

Figure 5.6(b) shows the normalized optical power transferred via the selected WGM, where considerable changes in the energy efficiency are also observed when varying the carrier temperature. The utilization ratio of the hot carrier energy will be larger with a higher carrier temperature. When  $T_c > 1800$  K, transfer to the PV component can even become the dominate energy extraction channel apart from the converter's self-reabsorption. This phenomenon can be well explained by the change of carrier hot-luminescence current spectrum  $\dot{N}(\omega)$  in the bottom side of Figure 5.7. The current spectra are calculated from Eq. (5.7), Eq. (5.8) and Eq. (5.11), which combines both the luminescence transfer spectrum and also the occupation function of carriers. The absorbed local power intensities  $\dot{Q}(\mathbf{r})$  are also given on the top side of Figure 5.7, which is evaluated by integrating  $\omega \epsilon_0 \epsilon_f''(\mathbf{r}; \omega) |\mathbf{E}(\mathbf{r}; \omega)|^2$  in Eq. (5.5) over frequencies when the up-converter is acting as the emitter.

Three cases are considered with different carrier temperatures in the up-converter.

When  $T_c$  is not much above room temperature, such as  $T_c = 450$  K in Figure 5.7(a) and (d), the yield of carrier up-conversion at the coupling frequency 1.18 eV is around zero. Nearly all of the luminescence is emitted below the absorption edge of the PV component. The purple areas in Figure 5.7 (d),(e) and (f) represent the absorbing regions of the PV component. Apart from a partial self-reabsorption by the converter, most of

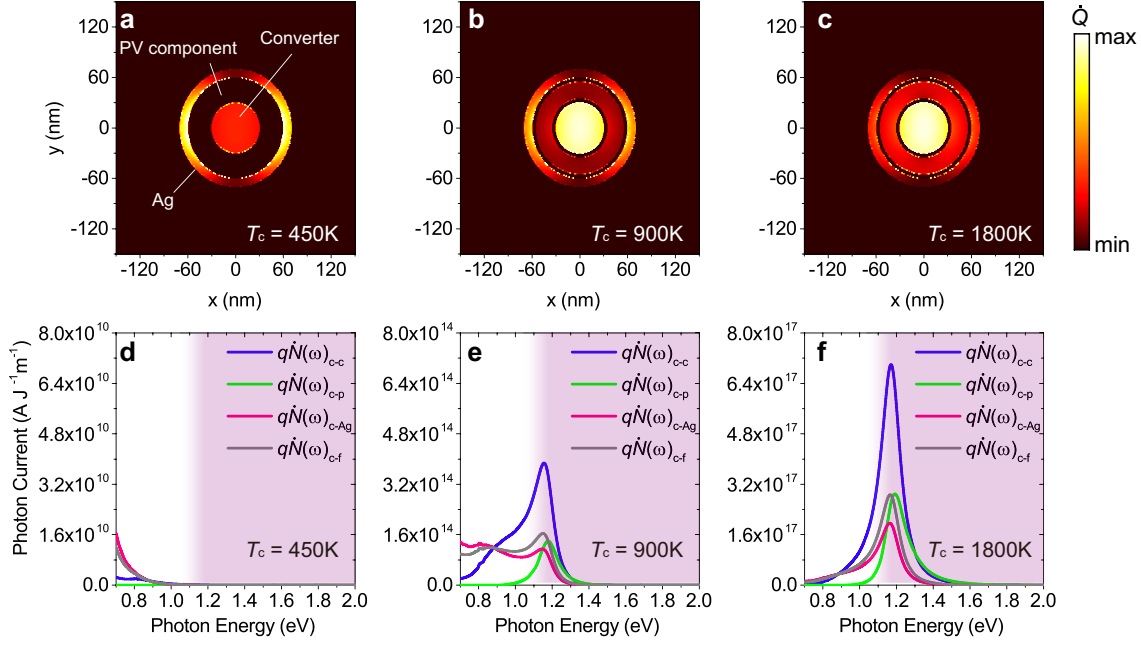


Figure 5.7: (a), (b), (c) Normalized local power absorption  $\dot{Q}(\mathbf{r})$  in the nanowire excited by converter's luminescence under different  $T_c$ ; (d), (e), (f) Corresponding photocurrent spectrum  $q\dot{N}(\omega)$  absorbed by different components. The purple region highlight where the PV component is absorbing.

the luminescent power is dissipated in the silver shell and radiated to the far-field. No photocurrent can be absorbed by the PV component in this case, as shown in Figure 5.7(a), even through a photonic enhancement has been introduced.

A more efficient up-conversion occurs when  $T_c$  rises to 900 K. Correspondingly, much stronger carrier hot-luminescence is observed now with an apparent peak around the coupling energy in their spectra, as shown in Figure 5.7(e). Figure 5.7(b) also shows that the hot-luminescence starts to excite the PV component properly. However, relatively large optical losses still exist below the bandgap of the PV component.

When the carrier temperature increases to 1800 K, hot-luminescence transfer via the WGM is further improved in both of the intensity and monochromaticity. It becomes competitive with other optical losses channels near and even below the bandgap of PV component, as shown in Figure 5.7(c) and (f). Importantly, although the spectrum converter in this example has continuous electronic energy states, which is reflected by the continuous  $\varepsilon''_{\text{InN}}(\omega)$  of InN, a narrowband carrier hot-luminescence can still be achieved using the OESC providing sufficient yield of carrier up-conversion.

### 5.3.4 Photovoltaic efficiency with hot-luminescence up-conversion

With a clear understanding of the carrier hot-luminescence transfer via the WGM in the core-shell nanowire structure, we now evaluate the photovoltaic performance of this

system.

We keep to the standard framework of detailed-balance as that used in Chapter 3 to simplify the discussion. By assuming a zero chemical potential and no thermalization losses inside the up-converter [7, 8], the steady carrier temperature  $T_c$  is then solved by the energy conservation equation Eq. (5.12). This equation is evaluated at a single cross-sectional plane of the nanowire by considering the non-polarized external incident light is perpendicular to the long-axis of the wire, as shown in Figure 5.2.

$$\dot{Q}_{s-c}(R_c) + \dot{Q}_{p-c}(qV) = \dot{Q}_{c-p}(T_c) + \dot{Q}_{c-f}(T_c) + \dot{Q}_{c-Ag}(T_c) \quad (5.12)$$

$$\dot{Q}_{s-c}(R_c) = \frac{f_s R_c}{4\pi^2 c^2} \int_{E_1}^{E_2} \Theta_s(T_s, 0) \sigma_c(\omega) \omega^2 d\omega \quad (5.13)$$

The incident power from the sun  $\dot{Q}_{s-c}$  is a function of concentration factor  $R_c$  with  $T_s = 5760\text{K}$ ,  $f_s = 2.1464 \times 10^{-5}$  [115],  $\sigma_c(\omega)$  is the absorption cross-section of the up-converter. The electroluminescence (EL)  $\dot{Q}_{p-c}$  from the PV component is determined by its bias voltage  $V$ , whose temperature is always at 300 K. The term  $\dot{Q}_{c-Ag}$  represents energy losses due to parasitic absorption by the silver shell. Since no thermalization loss is considered here, the obtained  $T_c$  from Eq. (5.12) corresponds to the maximum available carrier temperature and also the up-conversion yield in this model. Based on the quantities defined above, the device efficiency  $\eta$  is then determined with respect to the total incident power  $\dot{Q}_{\text{total}}(R_c) = \frac{f_s R_c}{4\pi^2 c^2} \int_0^\infty \Theta_{\text{sun}}(T_{\text{sun}}, 0) \sigma_{\text{wire}}(\omega) \omega^2 d\omega$  as below

$$\eta = \frac{qV}{\dot{Q}_{\text{total}}(R_c)} [\dot{N}_{s-p}(R_c) + \dot{N}_{c-p}(T_c) - \dot{N}_{p-c}(qV) - \dot{N}_{p-Ag}(qV) - \dot{N}_{p-f}(qV)] \quad (5.14)$$

Figure 5.8 shows device performance in two scenarios about the external excitation.

We first consider a single wire operation in Figure 5.8(a) and (b) by using the actual absorption cross-section of each component in the core-shell nanowire, which is evaluated by FDTD simulations. About 25% to above 50% increment in the power conversion efficiency (PCE) is obtained as shown in Figure 5.8(a), comparing to the case when the PV component works alone in the wire structure. Figure 5.8(b) explains the origin of PCE enhancements which comes from an efficient hot-luminescence coupling and therefore increased photocurrents of the PV component.

We then consider an ideal situation by assuming the overall system act as a back-side

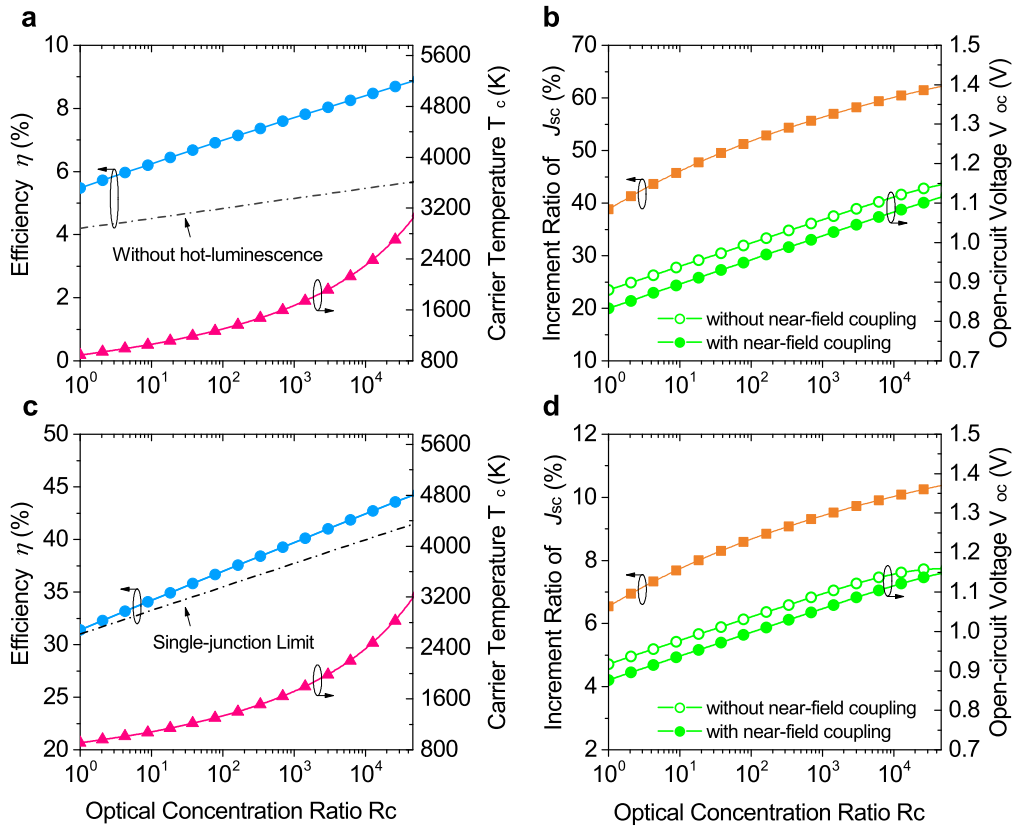


Figure 5.8: Device performance of the core-shell nanowire model examined by the detailed-balance model. Device efficiency and converter’s steady carrier temperature at the maximum power point in (a) single wire operation; (c) large wire array (single-junction limit). Increment ratios of the short-circuit current density  $J_{sc}$  in the PV component and also the corresponding open-circuit voltage  $V_{oc}$  in (a) single wire operation; (c) large wire array (single-junction limit).

up-conversion device with an ideal absorption, such as that discussed in Chapter 3. All the semiconductor components can fully absorb the external incident light with an energy above their bandgaps, i.e.,  $[0.7 \text{ eV}, 1.16 \text{ eV}]$  for the lower-bandgap up-converter and  $[1.16 \text{ eV}, \infty]$  for larger-bandgap PV component. By ignoring the field scattering occurring in the single wire picture, the geometric diameter for each component is used as the absorption cross-section. This situation can be considered as an analogy of a large wire array. Figure 5.8(c) confirms that the overall device efficiency can go beyond the conventional single-junction limit based on the current photon transfer spectra. An approximate increase of 7%  $\sim$  10% in the photocurrent can be achieved in this case. As a reference, by keeping the thicknesses of the converter and PV component as the same, the transferred carrier hot-luminescence via the far-field coupling in a face-to-face planar geometry can only contribute about 0.1% of  $J_{sc}$ .

Both scenarios suggest the effectiveness of photonic management in the luminescence transfer and also the potential of this particular plasmonic nanowire example.

It is also noted that in both cases the open-circuit voltage  $V_{oc}$  always drops a little when the near-field coupling is introduced, which is not surprising as we have discussed in Chapter 3. In such an optically-integrated device, the actual open-circuit voltage will depend on the steady carrier temperature  $T_c$  in the converter (see Eq. (3.6) in Chapter 3) which cannot go above the temperature of the sun ( $T_c \leq T_s$ ). However, in this particular example, we also need to emphasize the detrimental effects from the parasitic absorptions of the silver shell which increases the dark saturation current of the PV cell as well when examining Eq. (3.6) (adding an extra term in the denominator).

Figure 5.8 also gives the steady carrier temperature solved at the maximum power point of each situation. All these temperatures have reasonable values compared to the typical working condition of the electrical hot carrier solar cell [29, 34]. Besides, silver's parasitic absorption and also the far-field radiation losses are suppressed under these high carrier temperatures, as shown in Figure 5.7. It is also another important reason to achieve PCE enhancements.

## 5.4 Discussion

Further discussions about the physical fundamentals of the near-field energy luminescence transfer are given here.

We have developed the analytical formula of the photon transfer spectrum for the near-field coupling in Eq. (5.10), which contains a spatial integral of Green's function over the emitter's volume. Actually, this integral of the Green's function is no stranger to the field of nano-optics [88]. After some mathematical manipulations (see Appendix B), we can finally rewrite the near-field photon transfer spectra as below

$$\begin{aligned} \chi_{e-r} &= \frac{2}{\pi} \int_{V_r} d\mathbf{r}^3 \varepsilon_r''(\mathbf{r}; \omega) \int_{V_e} d\mathbf{r}_0^3 G_{im}(\mathbf{r}, \mathbf{r}_0; \omega) \varepsilon_e''(\mathbf{r}_0; \omega) G_{im}^*(\mathbf{r}, \mathbf{r}_0; \omega) \\ &= \frac{\omega}{3} \int_{V_r} d\mathbf{r}^3 \varepsilon_r''(\mathbf{r}; \omega) \rho_i(\mathbf{r}; \omega) - \hat{S}(\mathbf{r}; \omega) \end{aligned} \quad (5.15)$$

, where  $\rho_i$  is the projected LDOS in direction  $i$  while  $\hat{S}(\mathbf{r}; \omega)$  is about the surface integral of the Green's function. Then, the transferred optical power can be written correspondingly as

$$\begin{aligned}\dot{Q}_{e-r}(\omega) &= \chi_{e-r}(\omega)\Theta_e(T_e, \mu_e) \\ &= \frac{1}{3} \cdot f_{\text{ph}}^e \cdot \hbar\omega \cdot \omega \cdot \int_{V_r} d\mathbf{r}^3 \varepsilon_r''(\mathbf{r}; \omega) \rho_i(\mathbf{r}; \omega) - \hat{S}(\mathbf{r}; \omega)\Theta_e(T_e, \mu_e)\end{aligned}\quad (5.16)$$

, where  $f_{\text{ph}}^e$  is the shorthand of the Bose-Einstein's probability in the function  $\Theta_e$  belonging to the luminescence emitter.

It is noted that the first term in Eq. (5.16) is exactly the result of Eq. (3.11) in Chapter 3 if the PV cell is acting as the photon receiver<sup>2</sup>. In that term, the transferred optical power is represented by a product of the LDOS  $\rho_i$  (with modifications from photonic engineering) and optical conductivity  $\omega\varepsilon''$  in the PV cell. However, since the second term is non-zero typically, it suggests that the luminescence transfer process cannot take a full use of the receiver's LDOS. In fact, the term  $\hat{S}(\mathbf{r}; \omega)$  vanishes when the net Poynting vector over the receiver's volume is zero [148], which happens only in an ideal resonant cavity without local absorptions and far-field leakage. Therefore, the estimation of Eq. (3.11) is the upper limit of optical contacting for an established photonic configuration while the photon transfer spectrum  $\chi_{e-r}$  is the accurate expression. In other words, it confirms again that recognizing the damping characteristics of optical modes is critical to obtain an accurate and self-consistent photonic dynamics.

Another aspect of note concerns the dipole intensity predicted by the fluctuation-dissipation theorem (FDT). Strictly speaking, the conclusion of FDT is only valid when the dipole population is in a thermal-equilibrium state, such as that in the detailed-balance model. Revision of a non-equilibrium version of the FDT is far beyond the scope of this study. However, since we have noticed that the FDT is essentially compatible to the generalized Planck radiation formula in Eq. (5.4); at the same time we can also use the generalized dipole occupation function  $\{[\rho_e(\epsilon_e)/n(\epsilon_e) - 1][\rho_h(\epsilon_h)/p(\epsilon_h) - 1]\}^{-1}$  rather than the Bose-Einstein distribution to approximate the non-equilibrium photoluminescence (see Chapter 4), at least in the conventional study of semiconductor photoluminescence [34, 120]. Therefore, it seems acceptable to apply the generalized dipole occupation function in Eq. (5.3) as well to describe the carrier hot-luminescence. As a result, the relaxation-time approximation (RTA) model used in Chapter 4 becomes compatible to the luminescence formulas developed in this chapter.

---

<sup>2</sup>Factor 1/3 will disappear after run the Eisenstein's sun rule over index  $i$ .

## 5.5 Conclusions

In this chapter, a theoretical model based on electromagnetic Green's functions is presented to analyze the luminescence transfer via the OESC quantitatively. The localized cavity mode introduced by the OESC works as an energy transfer channel near the resonant frequency, which enhances both the photon's emission and reabsorption of the spectrum converter and PV cell, respectively. Two aspects determine the effectiveness of luminescence coupling. The intrinsic photon transfer ability of the optical contact is characterized by the photon transfer spectrum, which relates to the photonic configuration of the system only. The actual emissivity of the luminescence will also be influenced by the occupation status of radiative dipoles. For example, a higher carrier temperature can improve both the intensity and monochromaticity of the transferred carrier hot-luminescence through a narrow-band extraction window.

A plasmonic core-shell nanowire structure is presented as an example to embody the developed theoretical tools. An up-conversion system is further considered based on this model to demonstrate the device operating principles in photovoltaic applications. Both the PV component and spectrum converter are integrated into the same core-shell nanowire structure and coupled with the plasmonic WGM. The hot-luminescence transfer rate is enlarged by about 4800 times in this particular example comparing to the far-field radiation counterpart, which fulfills the requirements of optical enhancement asked by Chapter 3 and Chapter 4. Modifying the field distribution of the optical mode can further improve the performance of near-field coupling. For example, increasing the field penetration into the PV component can reduce the ratio of useless photon-recycling in the spectrum converter. On the other hand, the inevitable absorption by the metal leads to a considerable loss in this surface plasmonic optical contact, which can be reduced by adopting dielectric resonators. Potential structures include the photonic crystal cavity [63, 67], waveguide [74–77], Mie resonator [70], and ultra-thin metamaterials such as graphene [149, 150].

Since photon absorption is essential in this OESC problem, the lossy nature of the resonant mode has to be carefully considered. The QNM method developed recently in nano-optics is therefore adopted here to calculate an accurate and self-consistent Green's function. It is also worth noting that by defining a proper dipole distribution function  $\Theta(T_c, \mu)$  and optical constant  $\varepsilon(\omega)$  of the converter, the presented analysis can fit any functional materials being used for spectrum conversion including the commonly used dielectric matrix doped by rare-earth elements.



## Chapter 6

# Hot Carrier Dynamics in Lead-halide Perovskites

Apart from the development of optical energy selective contact (OESC), suppressing the non-radiative spectrum losses in the photon absorber material is another vital element to enable the optical hot carrier solar cell (OHCSC), concluded from the previous chapters. Exploring the high-quality hot carrier absorber material with outstanding optical properties is still challenging although encouraging progress has been achieved recently in the III-V (multiple) quantum wells [44, 151]. As a promising photovoltaic material with high yield luminescence and significant hot-phonon bottleneck effect discovered recently, the lead-halide perovskite becomes interesting to be explored as the potential hot carrier absorber material of the OHCSC. It shows that the slow hot carrier relaxation on hundreds of picoseconds in these materials relates to the localization of acoustic phonons, and organic cation assisted low-energy phonon up-conversions.

Using ultrafast optical characterization and first-principle calculations, four kinds of lead-halide perovskites with different cations and halide ions are compared in this chapter to reveal their carrier-phonon dynamics (Section 6.2). A stronger phonon bottleneck effect is observed in the organic-inorganic hybrid perovskites than in their inorganic counterpart (Section 6.3), where the up-conversion of low-energy phonons is proposed to explain the mechanism behind (Section 6.3 ~ 6.4).

## 6.1 Introduction: Lead-halide perovskites in photovoltaics

Significant progress has been achieved in metal-halide perovskite ( $\text{APbX}_3$ ) solar cells with the certified efficiency record now exceeding 20%, just a few years after the first solid state device was reported to have an efficiency of 9.7% in 2012 [152–154]. The photophysics and carrier dynamics in lead-halide perovskites have been intensively studied in the last few years because of their promising performance for the conventional photovoltaic devices with the thermalized carrier. The rapid emergence of lead-halide perovskites is attributed to their outstanding optoelectronic properties, including superb optical absorption, high ambipolar charge mobility, appropriate bandgap and low non-radiative recombination [155, 156]. Recently, a significant hot-phonon bottleneck effect in carrier thermalization was also observed in lead-halide perovskites [48, 157], which indicates potential applications of these kinds of materials in the advanced concept of hot carrier optoelectronics.

The so-called hot-phonon bottleneck effect denotes a phenomenon where the relaxation rate of a non-equilibrium carrier-phonon system is reduced when the carrier injection level is high [158–160]. Although several mechanisms have been suggested for the hot carrier dynamics on sub-picosecond timescales in lead-halide perovskites [50–52], a comprehensive understanding of the phonon bottleneck effect occurring on the subsequent and longer timescales (up to thousand picoseconds) is still lacking.

This study provides further insight into the phonon bottleneck effect in the lead-halide perovskite family. The hot carrier and phononic properties among four typical kinds of lead-halide perovskites used in photovoltaics, namely methylammonium lead iodide ( $\text{CH}_3\text{NH}_3\text{PbI}_3$ ,  $\text{MAPbI}_3$ ), formamidinium lead iodide ( $\text{HC}(\text{NH}_2)_2\text{PbI}_3$ ,  $\text{FAPbI}_3$ ), methylammonium lead bromide ( $\text{CH}_3\text{NH}_3\text{PbBr}_3$ ,  $\text{MAPbBr}_3$ ) and caesium lead iodide bromide ( $\text{CsPbIBr}_2$ ), are investigated. By varying the A-site cations ( $\text{MA}^+$ ,  $\text{FA}^+$ ,  $\text{Cs}^+$ ) and X-site halide anions ( $\text{I}^-$ ,  $\text{Br}^-$ ), the impact of lattice composition on the carrier cooling properties is elucidated. A complete picture of hot carrier relaxation in lead-halide perovskites is presented using the ultrafast transient absorption (TA) technique. Further studies of the phonon band structure and emission rates reveal the dynamics behind the relaxation. The phonon bottleneck effect in these materials is explained by the acoustic phonon up-conversion, which leads to a LO phonon emission rate that is at least 10 times slower in  $\text{FAPbI}_3$  compared to its inorganic counterpart under the same experimental conditions. The presence of rotatable groups on the organic sub-lattice is proposed to be the essential reason for these efficient up-transition dynamics, which appears to have been ignored

previously in lead-halide perovskite research.

## 6.2 Power dependent carrier cooling dynamics

All the samples used in this study, including MAPbI<sub>3</sub>, FAPbI<sub>3</sub>, MAPbBr<sub>3</sub>, and CsPbI<sub>3</sub>, were prepared on glass substrates with a thickness of about 300 nm. The sample preparation is described in Appendix C, and the detailed regular characterizations have been reported elsewhere [161–164]. The fundamental absorption bandgaps were determined to be 1.69 eV, 1.55 eV, 2.31 eV and 2.05 eV for the MAPbI<sub>3</sub>, FAPbI<sub>3</sub>, MAPbBr<sub>3</sub>, and CsPbI<sub>3</sub> samples, respectively. Based on the fabrication methods, all samples are optimized for conventional photovoltaic applications which are also sufficiently stable during the TA measurements to ensure that accurate and reproducible experimental data are obtained.

All the femtosecond pump-probe TA measurements (see Appendix C) were conducted under identical ambient conditions at room temperature (295 K). A pump pulse with a wavelength of 400 nm and duration of 100 fs was used to excite carriers well above the bandgap for all the samples, while an ultrashort broadband super-continuum laser covering the whole visible range was used as the probe. The pump-induced change in the absorption spectrum was acquired as a function of time delay. The carrier relaxation dynamics were then resolved via the bleaching in the spectra above the band edge under different excitation fluences. For more details about the experimental setup and theoretical understanding of TA spectroscopy, please see section 2.3.3 of Chapter 2.

### 6.2.1 TA spectra of lead-halide perovskites

Figure 6.1 shows the TA spectrum obtained from the FAPbI<sub>3</sub> sample under a pump fluence of  $90 \mu\text{J cm}^{-2}$  with an initial carrier concentration around  $N_0 = 4.84 \times 10^{18} \text{ cm}^{-3}$  (see Appendix C for carrier injection estimation). Sustained absorption bleaching is peaked around the apparent bandgap (about 1.55 eV) and broadening into the high-energy region, whose gradual narrowing as shown in Figure 6.1(b) and 6.1(c) exhibits the carrier relaxation process. It is noticed that the density of excited carriers in this study are comparable to the typical range employed in the previous studies [48, 165–168], where the influence of band fillings is not significant to the high-energy tail of the bleaching signal.

The so-called phonon bottleneck effect is qualitatively demonstrated by a power dependent measurement. The bleaching intensity in the high-energy region is markedly re-

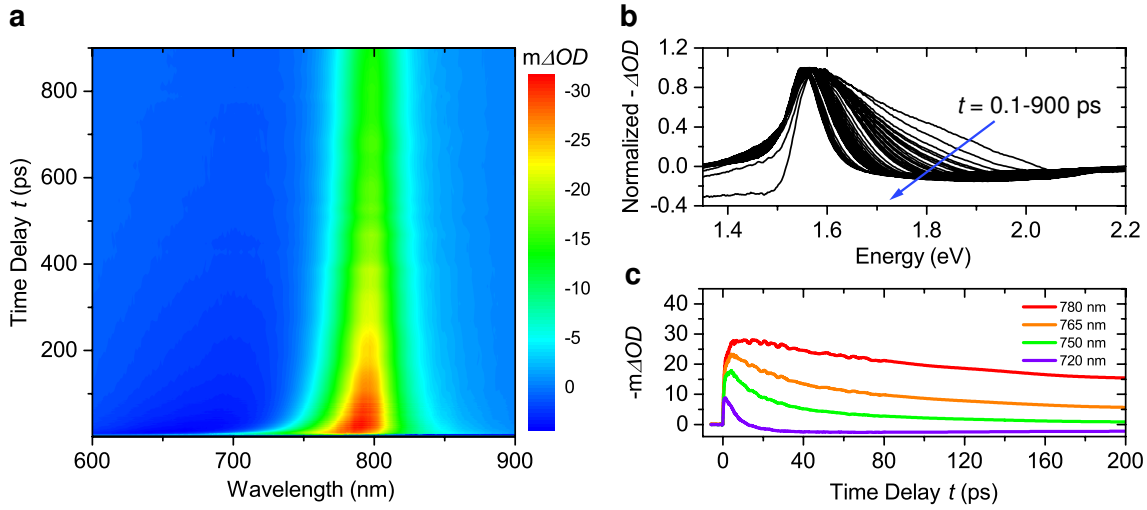


Figure 6.1: Transient absorption spectra of the FAPbI<sub>3</sub> sample. (a) 3D TA spectrum pumped at 400 nm with an initial carrier concentration  $N_0 = 4.84 \times 10^{18} \text{ cm}^{-3}$ . The initial broadening of the bleaching signal extending above the apparent bandgap energy indicates the temporary presence of high-energy hot carriers. (b) Normalized negative TA spectra ( $-\Delta OD$ ) at different pump-probe time delays  $t$  from 0.1 ps to about 900 ps. (c) Decay of the bleaching signal given as negative milli- $\Delta OD$  ( $-m\Delta OD$ ) at different wavelengths showing carrier relaxation kinetics.

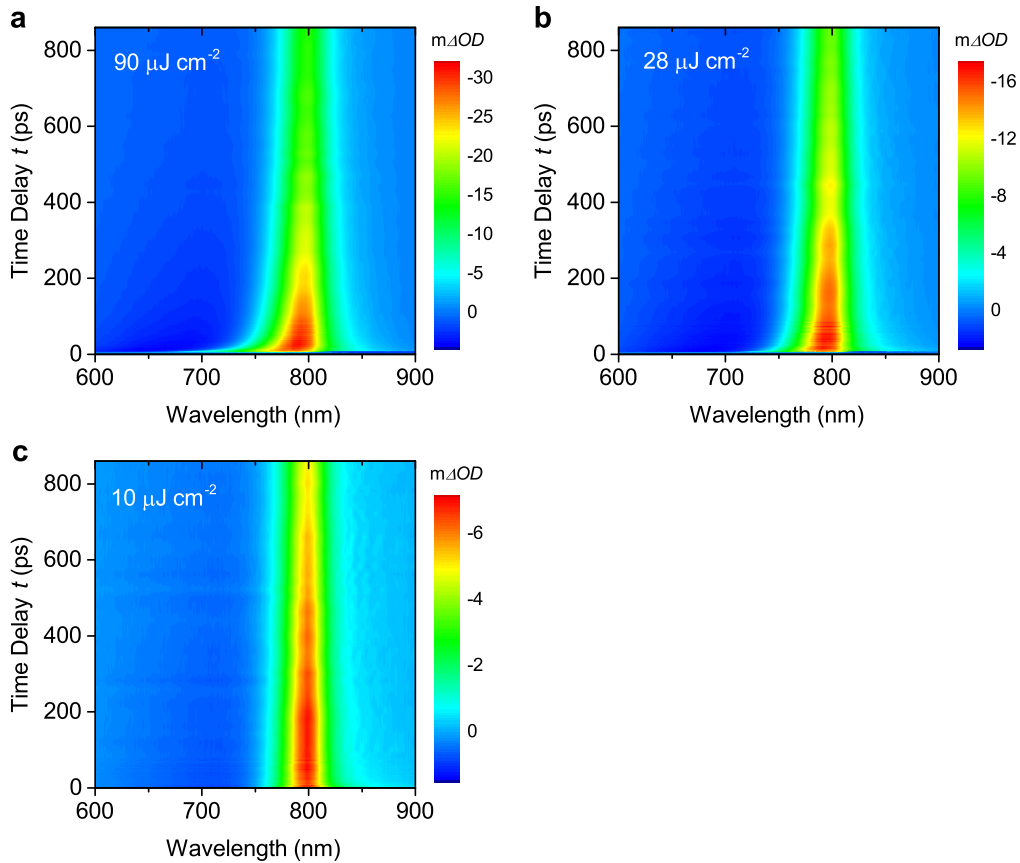


Figure 6.2: TA spectrum pumped at 400 nm in the FAPbI<sub>3</sub> sample with different excitation intensities and initial carrier concentrations: (a)  $N_0 = 4.84 \times 10^{18} \text{ cm}^{-3}$ ; (b)  $N_0 = 1.51 \times 10^{18} \text{ cm}^{-3}$ ; (c)  $N_0 = 5.38 \times 10^{17} \text{ cm}^{-3}$ .

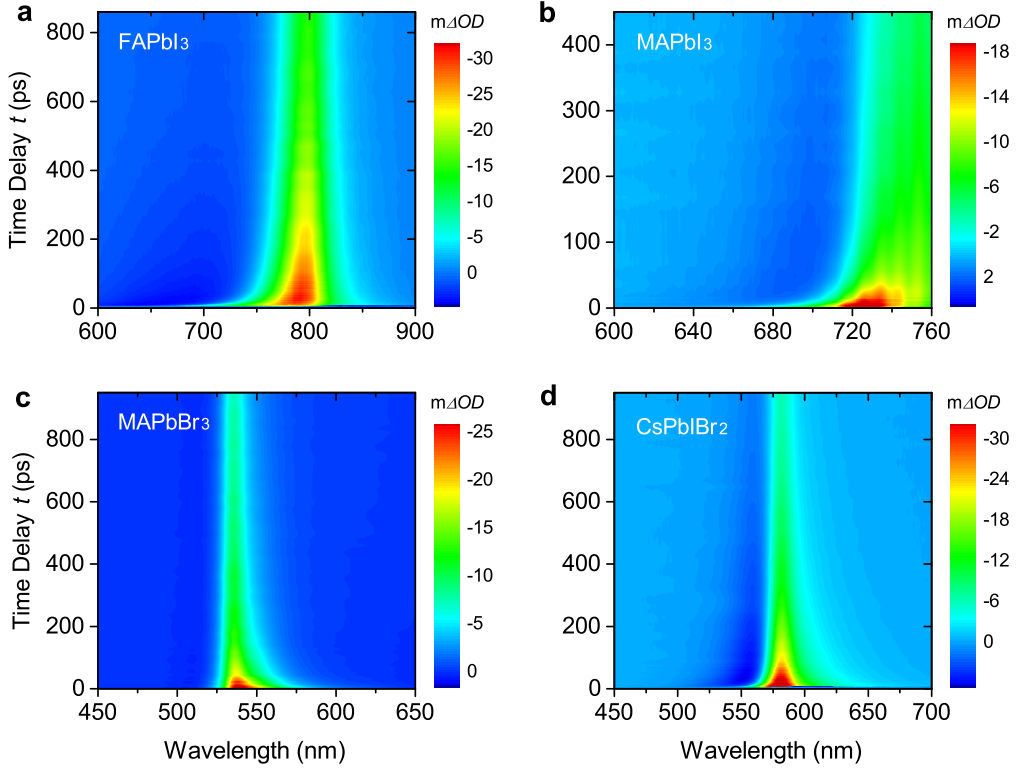


Figure 6.3: TA spectrum pumped at 400 nm with an initial carrier concentration around  $N_0 = 5 \times 10^{18} \text{ cm}^{-3}$  in four kinds of perovskite samples: (a). FAPbI<sub>3</sub>; (b) MAPbI<sub>3</sub>; (c) MAPbBr<sub>3</sub>; (d) CsPbIBr<sub>2</sub>.

duced under a pump fluence of  $10 \mu\text{J cm}^{-2}$  as shown in Figure 6.2, indicating a variation in carrier relaxation dynamics in different concentrations. Under similar experimental conditions, power dependent TA measurements were also performed on the other three samples. The measured 3D TA spectra under the maximum pump fluence (about  $100 \mu\text{J cm}^{-2}$ ) in each sample are given in Figure 6.3.

### 6.2.2 Carrier temperature fitting

Bleaching of absorbance reflects the carrier occupation above the band edge after excitation [102–104]. For carriers distributed across the high-energy region ( $\epsilon \gg \mu_c$ ,  $\epsilon$  is the carrier energy), the rigorous Fermi-Dirac distribution defined by carrier temperature  $T_c$  and chemical potential  $\mu_c$  can be approximated by a modified Maxwell-Boltzmann distribution, as shown in the first term of Eq. (6.1). The second term in that equation represents the photon-induced absorbance (PIA) in a parabolic band approximation [48]. This equation is then fitted to a high-energy tail of the bleaching peak to extract the carrier temperature. The contribution of PIA must be taken into account in order to further extend the fitting region to higher energies, where the TA spectra usually show a

positive  $\Delta OD$  due to a very low carrier occupation. The detailed influence of bandgap renormalization is ignored here since we deal with the high-energy tail only. Also, in a continuous band semiconductor with a reasonably well behaved parabolic band structure, the effect of absorptance on the emission spectrum at short wavelengths well above the bandgap is minimal for all but the highest illumination intensities. This fitting formula can better capture the exponential curvature of a TA spectrum when varying the tail selection scheme. A typical fitting example is shown in Figure 6.4, where the selected tails (see details below) are from 1/3 of the maximum bleaching with a 0.3 eV length.

$$f(\epsilon) \approx A_1 \exp\left(-\frac{\epsilon}{k_B T_c}\right) + A_2 \epsilon^{-1/2} \quad (6.1)$$

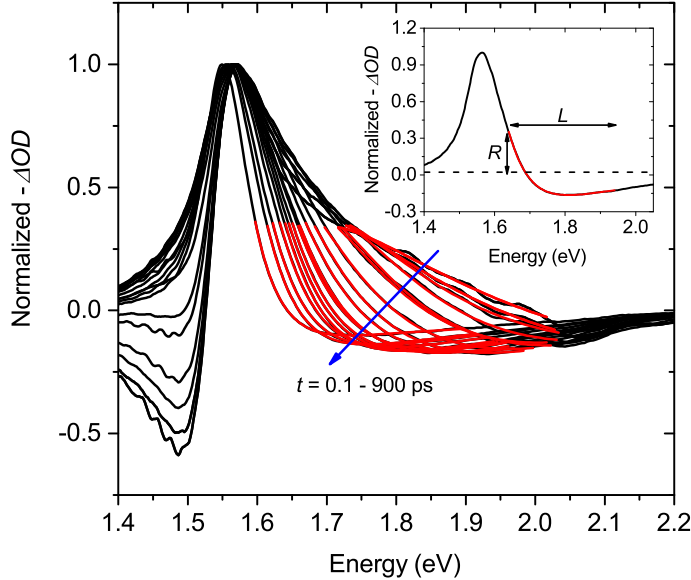


Figure 6.4: High-energy tails on the normalized bleaching spectra of FAPbI<sub>3</sub> sample under  $28 \mu\text{J cm}^{-2}$  when  $R$  is around 1/3 and  $L = 0.3 \text{ eV}$ . The black lines are the normalized minus  $\Delta OD$  ( $-\Delta OD$ ) for different time delays (from 0.1 ps to about 900 ps) while the fitted results are shown as red curves. The insert shows the definition of tail head ratio  $R$  and tail length  $L$  on an example TA spectrum

We always use the following tail selection scheme in all the TA spectra from different samples to ensure comparable results between them:

1. The high-energy tails are always selected from a location whose bleaching intensity has a constant ratio  $R$  (e.g., 1/5 initially) to the maximum bleaching, as shown in the inset of Figure 6.4;
2. All tails extend to the high energy region by a constant tail length  $L = 0.3 \text{ eV}$ ;
3. The modified Maxwell-Boltzmann fitting is applied on the selected tails at each time delay to get carrier temperatures  $T_c(t)$ ;

4. Using the same tail length  $L$ , the fitting is then repeated when increasing  $R$  from  $1/5$  to  $1/2$  linearly (in 10 steps) ;

5. All the fitted  $T_c(t)$  at the same time delay  $t$  under different  $R$  are then averaged as the final result. The corresponding standard error of the mean (s.e.m) of  $T_c(t)$  is considered as the error and will be labeled in the figure.

The fittings are then conducted among all the measured TA spectra using the tail selection scheme developed above. The fitted carrier temperatures as a function of time delay  $t$  are summarized in Figure 6.5. Precise sensitivity and stability analyses have also been carried out in Appendix D to ensure reliable and comparable fitting results.

### 6.2.3 Discussion on carrier temperature decay in lead-halide perovskites

For the different lead-perovskite samples, there are two common primary features in their cooling curves.

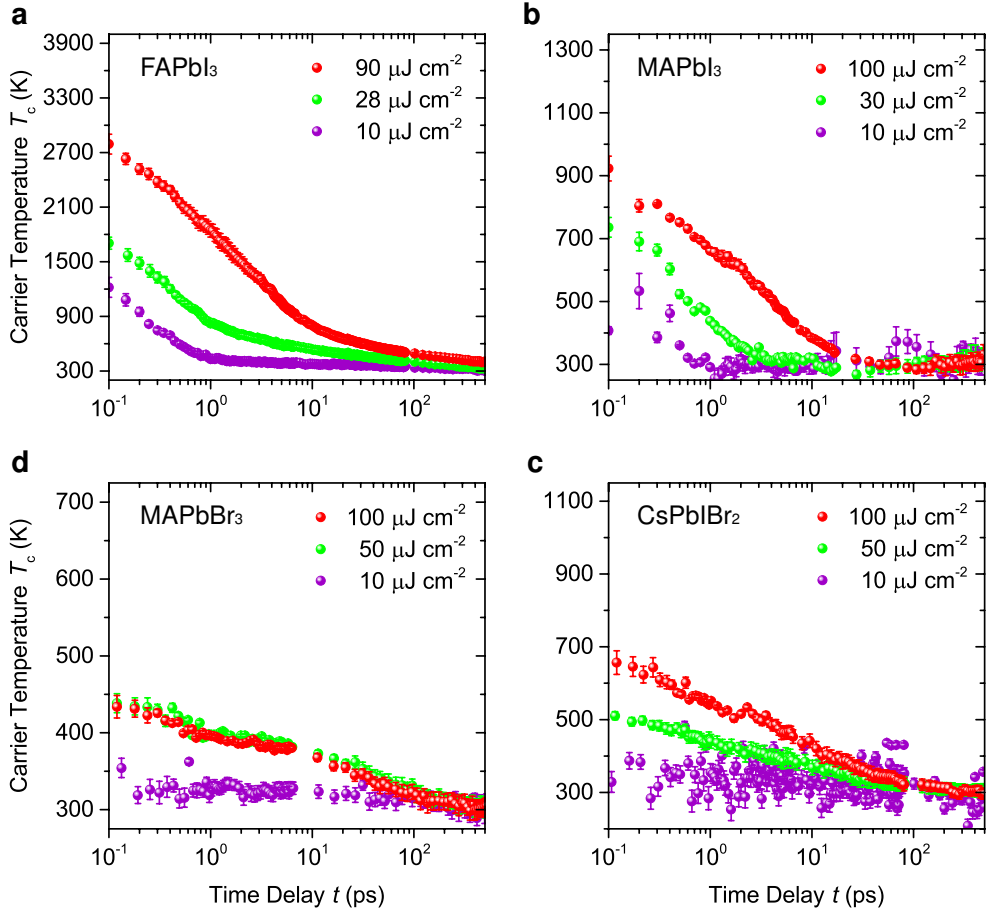


Figure 6.5: Time dependent carrier temperature under different incident fluence in: (a) FAPbI<sub>3</sub>, (b) MAPbI<sub>3</sub>, (c) MAPbBr<sub>3</sub>, (d) CsPbIBr<sub>3</sub>. The carrier temperatures are extracted by fitting the high-energy tail of the bleaching in the TA spectra. The error bar shows the standard error of the mean (s.e.m) fitting results.

First, all the samples show an evident temperature dependent carrier cooling rate which decreases when the carrier temperature is lower. Although the primary carrier temperature drop roughly occurs within the first 10 ps in these samples, a subsequent slower cooling rate extends the overall relaxation period up to several hundred picoseconds. On the same cooling curve of FAPbI<sub>3</sub> under 90  $\mu\text{J cm}^{-2}$  fluence in Figure 6.5(a), an average cooling lifetime of 25 ps and 124 ps are observed beginning at  $T_c = 1500\text{ K}$  and 700 K respectively. These average lifetimes are obtained using a double-exponential fitting which is applied from the selected initial high carrier temperature to the end of the cooling curve.

Second, two stages of the carrier cooling process are identified from Figure 6.5 whose cooling rates exhibit different power dependences. The first cooling stage shows a very similar sub-picosecond lifetime under different excitation intensities. This stage is dominated by the intrinsic Fröhlich phonon emission corresponding to the typical timescales studied previously in lead-halide perovskites [169]. A limited thermalization rate for hot holes is observed in this stage compared to conventional organic semiconductors. A reduced electronic density of states (DOS) near the fundamental valence band maximum (VBM) was used to explain the restricted relaxation of carriers which leads to the almost power independent cooling rate observed here. Since the electronic band structure near the band edge is primarily dominated by the lead-halide bond [169, 170], similar cooling lifetimes and their power independence are also observed in the inorganic CsPbIBr<sub>2</sub> sample. The second stage of cooling is then observed in the later period under a sufficiently high fluence (larger than 10  $\mu\text{J cm}^{-2}$ ). The cooling lifetime increases with a larger carrier density in the second stage, corresponding to the effect of a phonon bottleneck. From the similar double-exponential fitting used above from a fixed initial temperature  $T_c = 700\text{ K}$ , the cooling lifetime of FAPbI<sub>3</sub> grows from 45 ps to 124 ps when the fluence is tuned from 28  $\mu\text{J cm}^{-2}$  to 90  $\mu\text{J cm}^{-2}$  correspondingly.

Compared to FAPbI<sub>3</sub>, an average cooling lifetime of only 6 ps beginning from  $T_c = 700\text{ K}$  is observed in our MAPbI<sub>3</sub> sample with a much lower initial carrier temperature when it is under the maximum pumping. This observation is inconsistent with the previous theoretical and experimental conclusions on MAPbI<sub>3</sub>, although a power dependent bottleneck effect is also observed in the second cooling stage. The changes in the organic cation (FA<sup>+</sup> and MA<sup>+</sup>) with the same kind of lead-halide framework should not strongly perturb both the electronic and phononic properties of the material [48, 51, 169]. This significant difference is believed to be caused by the lattice defects. Previous observation confirms that the MAPbI<sub>3</sub> sample prepared by the gas-assisted method (See Appendix

C) has a large density of sub-bandgap trapping states [171]. The fast carrier relaxation observed here convinces us that a large number of above-bandgap defects also present in this sample which could provide more relaxation pathways for the hot carriers or more opportunity for hot carriers to be trapped [172]. It is noted that the solar cell made of such a material can still achieve a fairly good energy conversion efficiency up to 17% [161], suggesting that the relaxation of hot carriers seems to be more sensitive to the presence of lattice defects, perhaps due to their broadband energy distribution.

Although the initial carrier temperatures in MAPbBr<sub>3</sub> and CsPbIBr<sub>2</sub> are lower than that in FAPbI<sub>3</sub> and MAPbI<sub>3</sub> due to larger bandgaps, power dependent cooling lifetimes are still observed in their second cooling stage. Under a similar carrier concentration, the bottleneck effect of all samples can be compared by investigating the second cooling stage in a similar range of carrier temperature. To intuitively show the difference in the bottleneck effect among these samples, we first compare their average cooling lifetimes fitted with the same beginning carrier temperature  $T_c = 400$  K under an intermediate fluence ( $28 \mu\text{J cm}^{-2}$  for FAPbI<sub>3</sub>,  $50 \mu\text{J cm}^{-2}$  for MAPbBr<sub>3</sub> and CsPbIBr<sub>2</sub>). All the samples are then in the second cooling stage with a similar carrier density of about  $N_0 = 2 \times 10^{18} \text{ cm}^{-3}$  for a ready comparison. A cooling lifetime of about 305 ps is observed in the FAPbI<sub>3</sub> sample in this period, while only a lifetime of 71 ps and 37 ps are observed in the MAPbBr<sub>3</sub> and CsPbIBr<sub>2</sub> sample respectively. When the excitation intensity increases to the maximum one used in our measurements with a carrier density of about  $N_0 = 5 \times 10^{18} \text{ cm}^{-3}$ , the cooling lifetime of FAPbI<sub>3</sub> is significantly increased to around 1 ns after  $T_c = 400$  K while only about 48 ps is achieved in CsPbIBr<sub>2</sub>.

An unusual saturation effect was observed in the MAPbBr<sub>3</sub> sample (Figure 6.5), where both the TA spectra and carrier temperature show nearly the same result when the excitation is larger than  $50 \mu\text{J cm}^{-2}$ , corresponding to a carrier density about  $N_0 = 2.69 \times 10^{18} \text{ cm}^{-3}$ . Since there is no evidence of either saturation in absorptions at the pumping wavelength (400 nm) or a lasing effect in MAPbBr<sub>3</sub> according to the TA spectrum, we consider this observation to be a result of Auger-recombination/Impact-ionization (AI) processes [173]. It has been reported that the Auger coefficient in MAPbBr<sub>3</sub> is about four times larger than that in MAPbI<sub>3</sub> [174]. Triggered by a sufficiently high excess carrier concentration, it is possible that a strong multi-particle interaction occurs in this material, limiting the change of carrier temperature under a higher excitation power density.

## 6.3 Phonon relaxation and bottleneck effect

### 6.3.1 Review of carrier-phonon dynamics in semiconductors

To understand the mechanism behind the bottleneck effect observed in lead-halide perovskites, we first review some general understanding of carrier-phonon dynamics in solid-state polar semiconductors. The carrier thermalization is accompanied by the emission of LO phonons which then decay to the low-energy acoustical modes and lead to local lattice heating. With an efficient thermal transfer to the surroundings via acoustic phonon propagation, the carrier's excess kinetic energy is eventually dissipated irreversibly. Therefore, three distinct relaxation stages exist:

- 1) carrier-phonon scattering (Fröhlich interaction);
- 2) optical phonon decay to acoustic phonons;
- 3) acoustic phonon propagation to the far-field region in the material (thermal conduction).

Correspondingly, in a non-quantized system with continuous electronic DOS, possible blocking mechanisms can be introduced at each relaxation stage to prolong the overall cooling period of hot carriers:

- 1) thermal isolation between the optical phonon and carrier population;
- 2) reducing the phononic DOS to inhibit hot-phonon decay;
- 3) acoustic phonon up-conversion to optical phonon.

Strong thermal isolation required by the first mechanism is very difficult to achieve due to the spontaneous interaction between the carriers and LO phonons in a polar environment. In lead-halide perovskites, the Fröhlich interaction mainly occurs between the charge carriers and the lead-halide bond [51, 169], which governs the carrier relaxation in the first cooling stage. Although the large polaron effect proposed recently [50] demonstrates that a reduced carrier-phonon coupling may exist in the organic-inorganic lead-halide perovskites, a Fröhlich scattering rate similar to the typical III-V semiconductor materials, such as GaAs, has also been reported [48, 51]. In particular, since the electron-phonon coupling constantly occurs during carrier thermalization, a simple change of Fröhlich coupling also cannot explain why a power dependent carrier cooling rate is only observed in the second cooling stage while the rate in the first stage remains nearly unaffected. Therefore it can be ruled out as a primary cause of the phonon bottleneck effect here.

The second method is one of the popular mechanisms utilized in the current carrier

thermalization engineering. In typical semiconductor systems, the decay mechanisms of LO phonon to low-energy acoustic modes include the symmetric Klemens-decay and anti-symmetric Ridley-decay [10]. Opening the phonon bandgap (between the optical and acoustic branches) using compounds with a large atomic mass-difference has been intensively studied before [10, 175] to slow carrier cooling, since the Klemens-decay mechanism is blocked in principle if the phonon bandgap is greater than twice the highest acoustic phonon energy.

The third blocking mechanism happens in the last stage of carrier cooling where the induced local lattice heat finally dissipates to the surroundings. An efficient acoustic phonon up-conversion can recycle the thermal energy back and reheat carriers [176].

### 6.3.2 Phonon band structures of lead-halide perovskites

The phonon band structures of FAPbI<sub>3</sub>, MAPbI<sub>3</sub>, MAPbBr<sub>3</sub>, and CsPbBr<sub>3</sub> (as an analogue of CsPbIBr<sub>2</sub>) were calculated from first-principles using density functional theory (DFT) (see Appendix C). All the structures were optimized based on a pseudocubic lattice which has been extensively used to predict properties of these materials [177–179]. The calculation results have also been compared with previous reports to ensure a good estimation of the phonon energy distribution. Figure 6.6 shows the calculated phonon band structures (below 200 cm<sup>-1</sup>). All the acoustic bands are plotted as red curves. The imaginary phonon modes with a negative frequency result from the metastable lattice of the perovskite where the permanent displacement of the atoms is possible through distortions of the crystal lattice [169, 180]. The projected density of states (PDOS) on each atom is also given in Figure 3 to show the detailed contributions from each sub-lattice.

Evidently, no complete phonon bandgap is observed in these four kinds of perovskite. Therefore, there is no significant blocking effect from the second mechanism mentioned above. Compared to the inorganic type CsPbBr<sub>3</sub>, lattice vibration properties in the hybrid types are strongly affected by the presence of organic cations according to Figure 6.6. Different to the Cs<sup>+</sup> ion, whose vibrational modes are primarily distributed over the acoustic branches in CsPbBr<sub>3</sub>, the phonon modes relating to the organic cations show an optical-like character with a good overlap to the lead-halide optical modes in the range roughly from 30 cm<sup>-1</sup> to 100 cm<sup>-1</sup>. This result is consistent with the previous Raman observations [181] on MAPbI<sub>3</sub> that the libration and torsion of the MA<sup>+</sup> are coupled with the lead/halide ions and leads to a series of low-energy optical modes in the range of 60-

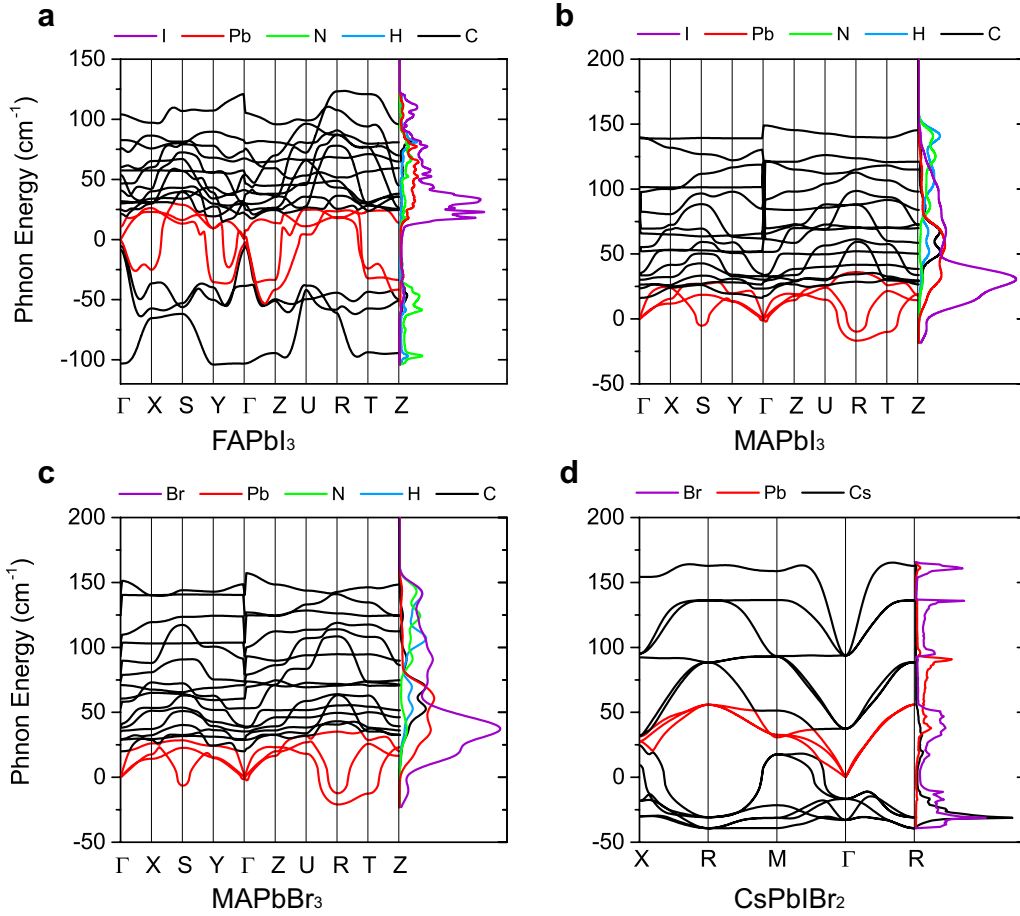


Figure 6.6: Phonon band structure and projected phonon DOS in (a) FAPbI<sub>3</sub>; (b) MAPbI<sub>3</sub>; (c) MAPbBr<sub>3</sub>; (d) CsPbI<sub>3</sub>. The projected phonon DOS are given in arbitrary units (A.U.) and show the contributions of the organic cation and inorganic sub-lattice respectively. The acoustic bands are plotted in the red.

$100 \text{ cm}^{-1}$ . This unusual phonon structure implies that although the organic cations do not govern the Fröhlich interaction directly, the overlapping vibration modes can still allow them to participate in the carrier-phonon relaxation through phonon-phonon scattering.

With the influence of non-propagating vibrations on the organic cation, most of the optical phonon modes below  $200 \text{ cm}^{-1}$  in the hybrid types show a relatively flat band dispersion across the first Brillouin zone comparing to the inorganic case. A cascade decay of LO phonons may be supported by this mini-band-like structure to slow phonon relaxation. However, it cannot fully explain the much slower carrier cooling lifetime of FAPbI<sub>3</sub> in its second stage (below  $T_c = 400 \text{ K}$ ) observed above comparing to MAPbBr<sub>3</sub>, although similar mini-band-like optical branches are shown in both of them. A series of high-energy (larger than  $200 \text{ cm}^{-1}$ ) quasi-static modes are also observed in the hybrid perovskites, which result from the resonant vibrations of H atoms primarily as shown in Figure 6.7. However, these high-energy modes are considered to be irrelevant to the carrier

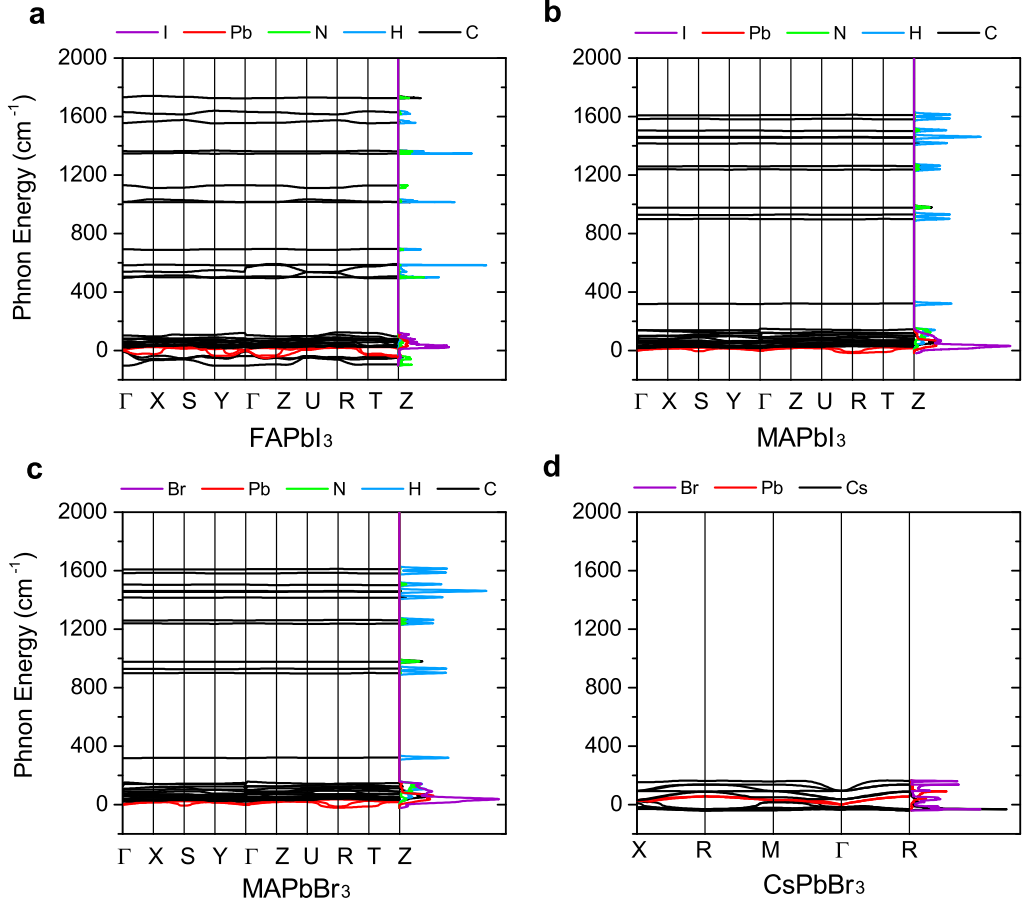


Figure 6.7: Phonon band structure and projected phonon DOS (larger view in phonon energy) in (a) FAPbI<sub>3</sub>; (b) MAPbI<sub>3</sub>; (c) MAPbBr<sub>3</sub>; (d) CsPbBr<sub>3</sub>. The projected phonon DOS are given in arbitrary units (A.U.) and show the contributions of the organic cation and inorganic sub-lattice respectively. The acoustic bands are plotted in red

relaxation because the band edge carrier states are mainly derived from the lead/halide atoms [48, 51, 169, 182].

### 6.3.3 Possibility of phonon up-conversion

As no apparent implementation of the first and second phonon blocking mechanisms exists in these materials, we infer that a relatively effective up-conversion of acoustic phonons may occur to prolong the relaxation period [176]. Actually, the acoustic-to-optical phonon up-conversion has been reported recently in the perovskite-like organic-inorganic hybrid multiferroic material [183]. In that material, the existence of organic sub-lattices introduces a series of low-energy “hybrid phonon” modes, which are defined as the strong co-vibrations between the organic and inorganic sub-lattices rather than the modes dominated by either kind of sub-lattice alone, according to Ref. [183]. These low-energy

optical-like “hybrid phonons” cannot be excited efficiently by an external perturbation but only by phonon-phonon scatterings instead. Their large thermal coupling rate to acoustic phonons, via phonon-phonon scattering, can facilitate the acoustics-to-optical phonon up-conversion and prolong the overall relaxation period of hot phonon populations.

We adopt the phonon classification concept here used in Ref. [183] and classify the phonons in organic-inorganic perovskites according to the PDOS plotted in Figure 6.6(a)-(c) and also Figure 6.7(a)-(c). As pointed out before, the co-vibrations between the organic cation and lead/halide ions roughly in  $30\text{-}100\text{ cm}^{-1}$  can be called “hybrid phonons”. Since initial Fröhlich scattering occurs on the lead-halide framework primarily, these low-energy “hybrid phonons” are mainly excited by phonon-phonon scattering events and these are very similar to the phonon relaxation process occurring in the multiferroic material discussed in Ref. [183]. Also, these “hybrid phonons”, which shows very little dispersion at around  $30\text{ cm}^{-1}$  have a good energy overlap with the top of the acoustic branches. This kind of phonon band structure is expected to increase the probability of acoustic phonons scattering to optical states and recycle the vibrational energy, corresponding to good thermal coupling. Based on this information, it is reasonable to propose that a similar acoustic-to-optical phonon up-conversion process discussed in Ref. [183] may also exist in lead-halide perovskites, especially in the organic-inorganic types. In partial support of this, the purely inorganic  $\text{CsPbIBr}_2$  sample with a simpler phonon band structure and reduced phononic DOS do have the fastest carrier relaxation rate in the second cooling stage, probably because they do not have the combined organic/inorganic hybrid phonon and hence do not undergo phonon up-conversion.

### 6.3.4 Hot phonon relaxation in lead-halide perovskites

To further quantify the relaxation rate of the phonon system, we estimate the average LO phonon emission lifetime  $\tau_{\text{ave}}$  for the three samples with good quality ( $\text{FAPbI}_3$ ,  $\text{MAPbBr}_3$ , and  $\text{CsPbIBr}_2$ ) using Eq. (6.2), where  $T_L$  is the lattice temperature [104]. Since the elastic scattering between LO phonons and carriers does not dissipate energy irreversibly, the eventual cooling of the carrier-phonon system is caused by the inelastic decay of optical phonons (exciting acoustic phonons). By considering both the emission and reabsorption processes of LO modes, the  $\tau_{\text{ave}}$  can be taken as an effective cooling lifetime of carriers interacting with a non-equilibrium phonon population [103, 104, 184].

$$-\frac{3k_B}{2} \frac{dT_c}{dt} \approx \frac{\hbar\omega_{LO}}{\tau_{ave}} \left[ \exp\left(-\frac{\hbar\omega_{LO}}{k_B T_c}\right) - \exp\left(-\frac{\hbar\omega_{LO}}{k_B T_L}\right) \right] \quad (6.2)$$

We choose the characteristic/effective LO phonon energies for FAPbI<sub>3</sub> [51], MAPbBr<sub>3</sub> [185, 186], CsPbBr<sub>3</sub> [187, 188] as 13 meV, 18 meV and 16 meV respectively by taking into account both the experimental and theoretical estimations performed before and also the band structure presented in Figure 6.6. These characteristic  $\hbar\omega_{LO}$  are near the top of the optical bands contributed by the lead-halide framework. Complete results for the carrier temperature dependent LO emission lifetime in each sample are given in Figure 6.9. All the samples start with a very rapid emission rate  $\tau_{ave}(t)|_{t \rightarrow 0} \leq 0.1$  ps in the early stage of carrier thermalization without an evident power dependence as shown in Figure 6.10, since a large non-equilibrium optical phonon population has not yet been achieved at that stage.

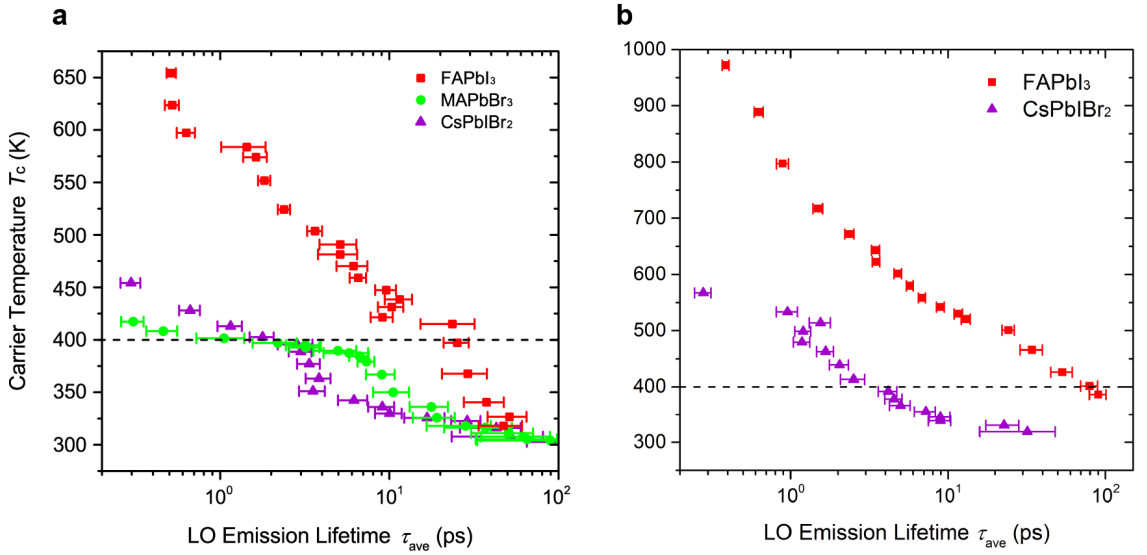


Figure 6.8: Phonon dynamics in lead-halide perovskites (a) Carrier temperature dependent phonon emission lifetime in different lead halide perovskites with a similar initial carrier concentration of around  $2 \times 10^{18} \text{ cm}^{-3}$ . An emission lifetime that is about 10 times longer than the other materials is observed in FAPbI<sub>3</sub> with carrier temperature at or below 400 K. The error bars show the standard error of the mean (s.e.m) emission lifetime; (b) Carrier temperature dependent LO phonon emission lifetime  $\tau_{ave}$  in FAPbI<sub>3</sub> and CsPbBr<sub>2</sub> with a similar initial carrier concentration  $N_0$  of around  $5 \times 10^{18} \text{ cm}^{-3}$ . The emission lifetime in FAPbI<sub>3</sub> is around 20 times longer than that in CsPbBr<sub>2</sub> when the carrier temperature is around 400 K. The error bar shows the standard error (s.e.m) of  $\tau_{ave}$

In Figure 6.8(a), we compare the results from the three perovskite samples with good lattice quality. Again, an intermediate excitation intensity ( $28 \mu\text{J cm}^{-2}$  for FAPbI<sub>3</sub>,  $50 \mu\text{J cm}^{-2}$  for MAPbBr<sub>3</sub> and CsPbBr<sub>2</sub>) is chosen for this comparison to avoid the influence of bleaching saturation in the MAPbBr<sub>3</sub> sample under a higher pump fluence. We now focus on the second cooling stage in each sample with a carrier temperature around

and below 400 K, where the cooling properties are dominated by the phonon bottleneck effect. We find that the phonon emission rate for FAPbI<sub>3</sub> is about 10 times slower than that in CsPbIBr<sub>2</sub> in this particular cooling period and around 3 times slower than that in MAPbBr<sub>3</sub>, as shown in Figure 6.8(a). A comparison of the LO emission lifetime between FAPbI<sub>3</sub> and CsPbIBr<sub>2</sub> under the maximum fluences is also provided in Figure 6.8(b). A larger increment of  $\tau_{\text{ave}}$  is still observed in FAPbI<sub>3</sub> which shows up to 20 times longer emission lifetime than CsPbIBr<sub>2</sub> around  $T_c = 400$  K. Further numerical estimation confirms that this discrepancy does not result from the different LO phonon energies used in the calculation but is dominated by the temperature gradient  $-dT_c/dt$  among the various samples instead. Indeed, the smaller LO phonon energy used for FAPbI<sub>3</sub> decreases the corresponding emission lifetime a little bit according to Eq. (6.2). Combined with the previous cooling lifetime comparison, it suggests that a much stronger bottleneck effect exists in FAPbI<sub>3</sub> while the pure inorganic counterpart shows the weakest blocking.

Varying phonon up-conversion efficiencies could also explain the differing phonon bottleneck effect observed in these materials, where the proposed up-conversion of acoustic phonons shows a strong correlation to the unique thermal property of lead-halide perovskites. It is expected that the up-conversion of acoustic phonons is accompanied by their rapid and short-range attenuation, which relates microscopically to the thermal conductivity of the material. A strong anharmonic phonon-phonon scattering corresponds to a low thermal conductivity in general which can localize acoustic phonons by blocking their propagation and increase the probability of an up-conversion event. In turn, an efficient acoustic-to-optical phonon up-conversion can contribute to the slow thermal propagation in the lattice and reduce the thermal conductivity, at least in principle [183].

In fact, an ultra-low thermal conductivity (less than  $1 \text{ W K}^{-1} \text{ m}^{-1}$ ) has been reported in both of the hybrid type lead-halide perovskites [189, 190] and their CsPbX<sub>3</sub> inorganic counterparts [191]. An enhanced anharmonic phonon-phonon scattering resulting from the highly overlapped phonon branches is recognized as the major cause, especially in the hybrid types [190, 192]. The resonant scattering resulting directly from the rotational-like vibrations of the organic cation also contributes [189, 190]. Both aspects are consistent with the picture of acoustic phonon up-conversion via the low-energy “hybrid phonon” modes presented above. In particular, the resonant scattering from the organic cation corresponds to an organic cation assisted up-conversion route for low-energy acoustic phonons, which directly indicates the co-vibrational optical-like modes can be re-excited by acoustic phonons efficiently in hybrid lead-halide perovskites and therefore recycle the phonon en-

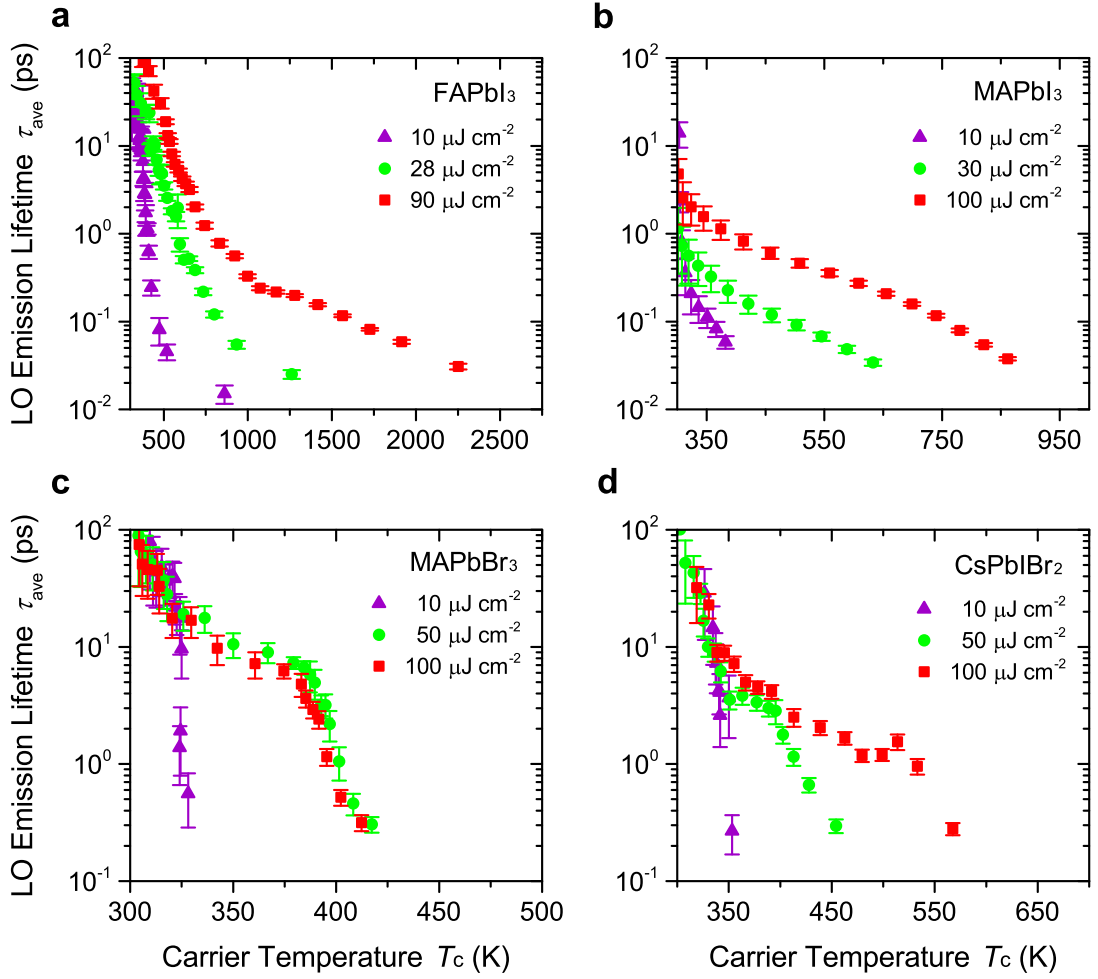


Figure 6.9: LO phonon emission lifetime  $\tau_{\text{ave}}$  versus carrier temperature  $T_c$  under different carrier injection levels in: (a) FAPbI<sub>3</sub>, (b) MAPbI<sub>3</sub>, (c) MAPbBr<sub>3</sub>, (d) CsPbIBr<sub>2</sub>. The error bar shows the standard error (s.e.m) of average  $\tau_{\text{ave}}$ .

ergy. It is worthy to mention that the phonon anharmonicity in the lead-halide perovskites can come from the octahedral tilting of the inorganic lattice alone, while the rotational activity of the organic cation introduces an additional anharmonic perturbation [192–194]. The strong phonon anharmonicity leads to a phonon lifetime in the perovskites to be three orders of magnitude smaller than that in GaAs and CdTe with a mean free path within 10 nm [192]. This efficient phonon confinement (isolation from far-field propagation) is beneficial to the phonon bottleneck effect and increases the probability of acoustic-to-optical phonon up-conversion, as that has been noticed in the quantum well/dot super lattice [195–198].

Now back to the divergence of LO emission lifetime in Figure 6.8. Phonon propagation is blocked in CsPbIBr<sub>2</sub> due to the anharmonic scatterings, which contributes to the power-dependent phonon bottleneck effect and increases the phonon up-transition probability.

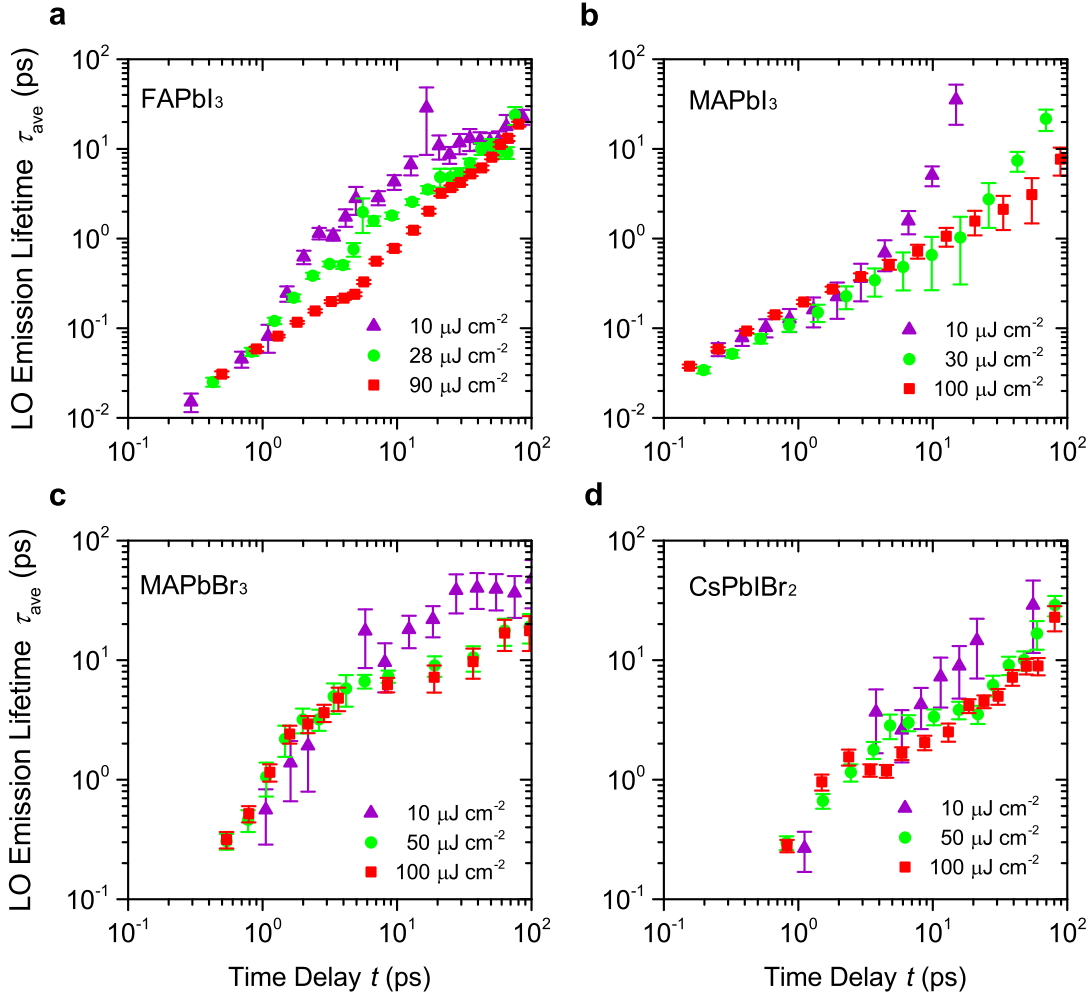


Figure 6.10: LO phonon emission lifetime  $\tau_{\text{ave}}$  varying with time delay  $t$  of measurement under different carrier injection levels in: (a) FAPbI<sub>3</sub>, (b) MAPbI<sub>3</sub>, (c) MAPbBr<sub>3</sub>, (d) CsPbIBr<sub>2</sub>. The error bar shows the standard error (s.e.m) of  $\tau_{\text{ave}}$ .

However, the lack of the rotatable organic cation and corresponding altered phonon modes leads to an insufficient phonon up-conversion efficiency compared to the other hybrid types. This suggests the indispensable role of the organic cation, or a large amount of low-energy co-vibrational optical modes, in the phonon up-conversion discussed here. The difference between FAPbI<sub>3</sub> and MAPbBr<sub>3</sub> may be the result of two aspects. On the one hand, a stronger acoustic phonon localization is expected in the FAPbI<sub>3</sub> compared to MAPbBr<sub>3</sub>. The thermal conductivity of MAPbBr<sub>3</sub> has been predicted to be higher than its iodide counterparts due to higher elastic moduli [190]. Practically, the trigonal phase of FAPbI<sub>3</sub> with a lower lattice-symmetry at room temperature is also expected to limit its thermal conductivity [199] further. On the other hand, it looks like a better phonon band overlap near the top of acoustic branches is observed in FAPbI<sub>3</sub> than in

MAPbBr<sub>3</sub> according to Figure 6.6. This could facilitate the re-excitation of optical modes in the former more efficiently. Overall, the conclusion is that an efficient up-conversion of low-energy phonons discussed here relies on both the blocking of the acoustic phonons propagation and organic cation assisted phonon up-transition. Both aspects lead to a significant hot-phonon bottleneck in the hybrid lead-halide perovskites, where the hot-phonon relaxation rate in FAPbI<sub>3</sub> is observed as at least 10 times slower than that in the inorganic counterpart via LO phonon emission.

## 6.4 Discussion

### 6.4.1 Proposed phonon dynamics in lead-halide perovskites

In summary, we propose the following carrier-phonon dynamics in hybrid type lead-halide perovskites to explain the observed strong phonon bottleneck effect under a large carrier population. The proposed process is shown in Figure 6.11.

- 1) Firstly, the Fröhlich interaction occurs predominantly between the hot carriers and inorganic sub-lattice, exciting the high-energy lead-halide LO phonons;
- 2) The excited LO phonons then decay to acoustic modes. During this stage, the co-vibration between organic and inorganic sub-lattices can also be excited via phonon-phonon scattering;
- 3) The propagation of acoustic phonons is blocked due to strong anharmonic phonon-phonon scatterings;
- 4) The up-conversion probability of phonons is then increased, especially when organic cations appear in the lattice. The organic cation introduces lots of low-energy co-vibrational optical modes which overlap well with acoustic branches and facilitate the phonon up-transition.
- 5) The recycled thermal (vibrational) energy reheats charge carriers and prolongs the overall cooling period of the carrier-phonon system.

It is worth emphasizing that processes 3)-5) are inefficient in conventional bulk semiconductors whose acoustic phonons can easily propagate away increasing the hot carrier cooling. The overall thermal recycling will be more efficient when the phonon density is larger since the probability of phonon-phonon scattering and up-conversion will further increase, especially if phonon propagation is restricted. This leads to an apparent pumping power dependent hot-phonon bottleneck effect.

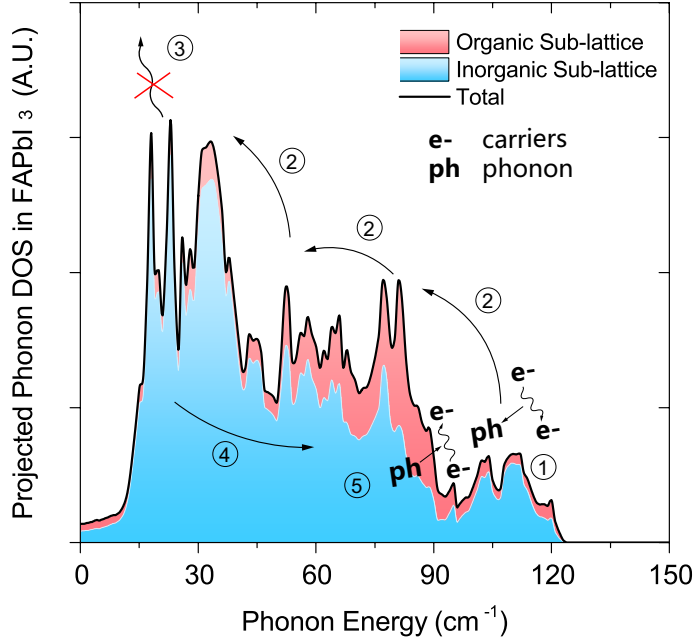


Figure 6.11: Proposed phonon dynamics in the FAPbI<sub>3</sub>. The solid black line shows the total phonon DOS, in which the contributions from the inorganic and organic sub-lattices are shown by the blue region on the bottom with the pink region stacked on top, respectively. The labeled phonon dynamic process are: 1) Fröhlich interaction of carriers primarily on the lead-halide framework; 2) Relaxation of lead-halide LO phonon, organic sub-lattice can be excited by phonon-phonon scattering; 3) Propagation of acoustic phonon is blocked due to anharmonic phonon-phonon scatterings; 4) Up-conversion of acoustic phonons; 5) Carrier reheating.

## 6.4.2 Further discussions about phonon dynamics

Further considerations about the proposed carrier-phonon dynamics are addressed below.

The mechanism behind the bottleneck effect we have discussed relies on the unique lattice structure and phonon properties of lead-halide perovskites, especially in the organic-inorganic hybrid types. Low-energy optical modes that have a good overlap with acoustic modes need to be introduced to realize a more efficient up-conversion process. This is supposed to be a new and general strategy to achieve long-lived hot carriers in material than opening a large phonon bandgap. It is now established that the large bandgap is not sufficient to suppress the decay of hot phonons, especially those via the anti-symmetric Ridley route in practice [200]. Blocking the propagation of acoustic phonons is another aspect to enhance the overall efficiency of up-conversion, since selection and conservation rules usually limit the up-conversion probability. Materials with a low thermal conductivity are valuable to explore, such as the thermoelectric material with strong phonon confinements, and the type with organic-inorganic hybrid compositions.

We also notice that our proposed mechanism has some relations to the large-polaron effect suggested by Zhu et al. recently [50]. This theory suggests that the freely rotating

organic cation can form a long-range polaron along with charge carriers. The large polaron can screen the hot carriers from scattering with LO phonons. This mechanism only relates to the effective strength of Fröhlich interaction in this material (the first kind of blocking mechanism mentioned above) and dominates in the first cooling stage primarily. Instead, the mechanism we proposed here is attempting to explain the bottleneck effect in the following second cooling stage on a timescale of several hundred picoseconds. These two mechanisms are not in contradiction with each other. In fact, the polaron effect suggests a stronger dynamic coupling between the charge carriers and organic cation directly in lead-halide perovskites, which is usually ignored in the conventional description. Our study also indicates the rotatable organic cation plays a major role in the acoustic phonon up-conversion in this kind of material. The direct coupling between carriers and organic cation may further facilitate the thermal recycling of the material, since the vibrational energy transferred onto the organic sub-lattice from low-energy modes could reheat charge carriers more efficiently. Additional works to further investigate the connection between these two mechanisms are still needed.

## 6.5 Conclusion

In conclusion, we have studied the bottleneck effect of carrier-phonon cooling in various lead-halide perovskite thin films with different compositions. By comparing both the carrier cooling lifetime and LO emission rate, we conclude that the hybrid perovskites have a stronger phonon bottleneck effect than the pure inorganic types. The phonon relaxation lifetime in FAPbI<sub>3</sub> is estimated to be more than 10 times longer than that in CsPbIBr<sub>2</sub> under a similar carrier concentration and temperature. The up-conversion of acoustic phonons was proposed as the primary factor in the phonon dynamics. In hybrid type perovskites, the low-energy optical phonon modes introduced by the rotatable organic cation show a good band overlap and thermal coupling with the acoustic phonons, allowing an efficient phonon up-conversion. Blocking phonon propagation caused by strong anharmonic scatterings also increases the up-conversion probability of low-energy modes. Both aspects mentioned above result in an efficient vibrational energy recycling in hybrid lead-halide perovskites and prolong the overall cooling period of the carrier-phonon system. It is valid to note again that the poor hot carrier response observed in our MAPbI<sub>3</sub> sample despite it having a fairly good performance in conventional solar cells. Particular attention to the lattice purity is required in the hot carrier applications although it is also vital in

the conventional photovoltaics as we all know.

## Chapter 7

# Conclusions

### 7.1 Summaries of the thesis

This thesis presented a series of studies to explore the working and design principles of the optical hot carrier solar cell (OHCSC), known as a general optically-integrated spectrum conversion system.

An OHCSC integrates a hot carrier absorber and a conventional solar cell together using a photonic structure called the optical energy selective contact (OESC), which enhances the carrier hot-luminescence transfer rate at the bandgap frequency of the solar cell to reduce the thermalization losses during the conversion. Such an optically-integrated system has the physical features of both a hot carrier solar cell and a spectrum up/down converter. Therefore, all the results about device physics, photonic engineering, and other developed theoretical tools are also applicable to the latter.

There are two essential aspects to realize the device concept properly. First, it relies on a well-designed photonic engineering to obtain quasi-monochromatic carrier hot-luminescence with a matched frequency and sufficient intensity to the secondary solar cell. Second, it requires a slow hot carrier cooling rate or fast Auger-recombination/Impact-ionization (AI) process to improve the spectrum conversion yield of the hot carrier absorber.

In this thesis, the potential and feasibility of this novel photovoltaic concept are examined in a more practical consideration with detailed numerical examples and experimental characterizations. It has developed a complete picture of the device operating and also the theoretical tools for further analyses.

Chapter 3 explored the global working principles of the OHCSC within the frame-

work of detailed-balance and thermal-equilibrium. It is where the similarity between the OHCSC and the conventional spectrum conversion systems is recognized. A systematic comparison between these two concepts is discussed at the beginning of Chapter 3, which concludes the carrier hot-luminescence as a general representation of spectrum up/down conversion processes. The gain of photon currents is then recognized as the necessary condition to improve the power conversion efficiency (PCE) of the device eventually. It demonstrates the necessity of photonic engineering for such a device. The significance of the feedback electroluminescence (EL) from the photovoltaic (PV) cell is also emphasized, which can strongly perturb the conversion dynamics of the spectrum converter when a deep photonic engineering presents. It leads to a complex dependence of the device performance on both the optical enhancement ratio and the working voltage of the PV cell. Among them, the phenomenon of “voltage-dependent open-circuit voltage” is valuable to mention again here (Figure 3.6). This effect indicates that the actual open-circuit voltage of the cell will be larger than its pseudo value  $k_{\text{B}}T_{\text{rt}}/q \cdot \ln(J_{\text{sc}}/J_0)$  estimated at the short-circuit condition since the emitted EL will be resorted to the cell efficiently by a lossless spectrum converter through a superb OESC.

Chapter 4 improved the modeling method of spectrum conversion dynamics to consider the non-equilibrium steady state of the hot carrier population inside the converter. By using the relaxation-time approximation (RTA) method, the final steady state of the hot carrier population is established based on the competition between multiple carrier scattering mechanisms. It, therefore, can estimate the non-radiative spectrum losses, such as the thermalization, naturally and obey the directionality of thermodynamics for the spectrum conversion. It suggests the OHCSC still shows potential in more practical considerations but with more stringent requirements in both of the carrier cooling lifetime and optical enhancement ratio. Several unique operating features rise further when the non-radiative spectrum losses occur in the device. First, it shows that an effective optical extraction can increase the quantum yield of the carrier hot-luminescence by reducing the probability of carrier thermalizations and shifting the dynamic equilibrium of electrochemistry. Second, the actual yield of the hot-luminescence also depends on the carrier refilling rates within the extract window, requiring a fast carrier renormalization. Third, the feedback EL will increase the probability of carrier thermalization that causes serious energy losses in the open-circuit condition. The effect of “voltage-dependent open-circuit voltage” will be weakened correspondingly in this case due to the existence of thermalization losses. For a down-conversion system, it requires an optical enhancement ratio larger than hundreds

of times and a carrier thermalization lifetime longer than about 500 ps. On the other hand, the up-conversion systems typically require an even longer carrier thermalization lifetime (over nanoseconds) and stronger optical enhancements (over thousand times).

A complete portrait of OHCS has been depicted in the above chapters so far. To fulfill the requirements of device design, Chapter 5 and Chapter 6 further explore the photonic engineering and hot carrier dynamics respectively.

Chapter 5 studied the near-field resonant luminescence coupling in details, which is recognized to be more efficient to deliver the carrier hot-luminescence in Chapter 3. A rigorous electromagnetic model is presented in this chapter to analyze the luminescence transfer quantitatively. The electromagnetic Green's functions constructed by the quasi-normal mode (QNM) is one of the essential theoretical basis here. It emphasizes the damping nature of the optical modes in the energy transfer problem. It also has developed the photon transfer spectrum function  $\chi(\omega)$  to qualify the performance of the coupling process, which is recognized to be more accurate than the estimation based on the local density of optical states (LDOS) directly. A plasmonic core-shell nanowire structure is presented as an example which shows about 4800 times of optical enhancements in an up-conversion system via the plasmonic whispering-gallery-mode (WGM) comparing to the far-field radiation counterpart. The actual emissivity of the hot-luminescence will also be influenced by the occupation status of radiative dipoles which therefore exhibits carrier-temperature dependent photonic dynamics.

Exploring eligible hot carrier materials with a long thermalization lifetime and high luminescence yield is always challenging. In Chapter 6, the hot-phonon bottleneck effect in lead-halide perovskites is investigated, which is proposed to be a novel candidate in the hot carrier engineering recently with superb luminescence properties. By comparing both the carrier cooling lifetime and phonon emission rate, we conclude that the hybrid perovskites have a stronger phonon bottleneck effect than the pure inorganic types. The significant power-dependent phonon bottleneck effect extends the overall cooling period of hot carriers up to nanoseconds in the  $\text{FAPbI}_3$  whose phonon relaxation lifetime is also found to be more than 10 times longer at least than that in the  $\text{CsPbIBr}_2$  under a similar carrier concentration and temperature. The up-conversion of acoustic phonons via the co-vibrations of organic-inorganic sub-lattices was proposed as the main reason for the hot-phonon bottleneck effect. The presence of organic cations introduces overlapping phonon branches that facilitate the up-conversion of low-energy modes. The blocking of phonon propagation due to anharmonic scatterings also increases the overall up-conversion

efficiency. This result also suggests a new and general method for achieving long-lived hot carriers in materials, which, therefore, is expected to inspire new exploration of hot carrier functional materials in future.

Overall, this thesis concludes the concept of OHCS and OESC are promising to improve the PCE of photovoltaic devices. By applying both the material and photonic engineering, the optically-integrated spectrum conversion system would be an inspiring and exciting field to explore further.

## 7.2 Future work

Based on the obtained theoretical and experimental results, more studies of the OHCS could perform in the future. One aim is to develop the established theoretical framework further and investigate more candidate structures for the OESC. Also, further studies of the carrier hot-luminescence are also needed. Another important aspect is realizing the OHCS device experimentally with characterizations. In detail, following study directions are proposed.

### **Investigation of OESC based on the photonic crystal cavity and waveguides**

Although the plasmonic core-shell nanowire structure shows attractive potential and intuitive illustration of the OESC, the difficulties of fabricating high-quality core-shell nanowire structure are also noticed. Instead, the photonic crystal cavity and waveguide structures are easier fabricated based on the well-developed E-beam lithography technique. Importantly, it is compatible with the planar geometry in conventional photovoltaics. Some early modeling results have been reported in Ref. [201] by the author of the thesis, where a hexagonal-type (H1-type) photonic crystal cavity is examined as the OESC to increase the absorptance of a silicon thin-film by about 80 times with a proper energy selection. The overall transfer enhancement (both the emission and absorption) can reach to several hundred times, known as the optimal value for the high-yield spectrum converter (see Chapter 3).

### **Investigation of carrier hot-luminescence in lead-halide perovskites**

Ultrafast hot carrier dynamics in the lead-halide perovskites could be explored further using transient time-resolved photoluminescence microscopy (TRPL). It is encouraging to detect the carrier hot-luminescence signal in lead-halide perovskites considering its hot-phonon bottleneck effect and high-yield luminescence.

### **Investigation of non-equilibrium energy transfer using optical damping modes**

It is also interesting to combine the RTA model into the development of photonic analysis framework to examine the device performance, where further improvement of the non-equilibrium dissipation-fluctuation theorem and damping optics need to be introduced.



# Bibliography

1. IRENA (2017). *REthinking Energy 2017: Accelerating the global energy transformation* tech. rep. (International Renewable Energy Agency (IRENA), Abu Dhabi, 2017).
2. Green, M. A. Third generation photovoltaics: Ultra-high conversion efficiency at low cost. *Progress in Photovoltaics: Research and Applications* **9**, 123–135 (2001).
3. Conibeer, G. Third-generation photovoltaics. *Materials Today* **10**, 42–50 (2007).
4. Shockley, W & Queisser, H. J. Detailed balance limit of efficiency of p-n junction solar cells. *Journal of Applied Physics* **32**, 510–519 (1961).
5. <http://pv.energytrend.com/pricequotes.html>
6. Ross, R. T. & Nozik, A. J. Efficiency of hot-carrier solar energy converters. *Journal of Applied Physics* **53**, 3813–3818 (1982).
7. Würfel, P. Solar energy conversion with hot electrons from impact ionisation. *Solar Energy Materials and Solar Cells* **46**, 43–52 (1997).
8. Farrell, D. J. *et al.* A hot-carrier solar cell with optical energy selective contacts. *Applied Physics Letters* **99** (2011).
9. Würfel, P. The chemical potential of radiation. *Journal of Physics C: Solid State Physics* **15**, 3967–3985 (1982).
10. König, D. *et al.* Hot carrier solar cells: Principles, materials and design. *Physica E* **42**, 2862–2866 (2010).
11. Hirst, L. C. & Ekins-Daukes, N. J. Fundamental losses in solar cells. English. *Progress in Photovoltaics* **19**, 286–293 (2011).
12. Würfel, P. *Physics of Solar Cells: From Principles to New Concepts* (Wiley, 2007).
13. Trupke, T., Green, M. A. & Würfel, P. Improving solar cell efficiencies by down-conversion of high-energy photons. *Journal of Applied Physics* **92**, 1668–1674 (2002).
14. Trupke, T., Green, M. A. & Würfel, P. Improving solar cell efficiencies by up-conversion of sub-band-gap light. English. *Journal of Applied Physics* **92**, 4117–4122 (2002).
15. Gai, S. *et al.* Synthesis of magnetic, up-conversion luminescent, and mesoporous core-shell-structured nanocomposites as drug carriers. *Advanced Functional Materials* **20**, 1166–1172 (2010).
16. Wang, F. & Melosh, N. a. Plasmonic energy collection through hot carrier extraction. *Nano Letters* **11**, 5426–5430 (2011).
17. Strümpel, C. *et al.* Modifying the solar spectrum to enhance silicon solar cell efficiency-An overview of available materials. *Solar Energy Materials and Solar Cells* **91**, 238–249 (2007).

18. Shalav, A., Richards, B. S. & Green, M. A. Luminescent layers for enhanced silicon solar cell performance: Up-conversion. *Solar Energy Materials and Solar Cells* **91**, 829–842 (2007).
19. Feldmann, C., Jüstel, T., Ronda, C. R. & Schmidt, P. J. Inorganic luminescent materials: 100 Years of research and application. *Advanced Functional Materials* **13**, 511–516 (2003).
20. Bednarkiewicz, A., Nyk, M., Samoc, M. & Streck, W. Up-conversion FRET from Er<sup>3+</sup>/Yb<sup>3+</sup>: NaYF<sub>4</sub> nanophosphor to CdSe quantum dots. *The Journal of Physical Chemistry C* **114**, 17535–17541 (2010).
21. Timmerman, D., Valenta, J., Dohnalová, K., de Boer, W. D.A. M. & Gregorkiewicz, T. Step-like enhancement of luminescence quantum yield of silicon nanocrystals. *Nature Nanotechnology* **6**, 710–713 (2011).
22. Zhuo, S., Shao, M. & Lee, S. T. Upconversion and downconversion fluorescent graphene quantum dots: Ultrasonic preparation and photocatalysis. *ACS Nano* **6**, 1059–1064 (2012).
23. Chen, G., Yang, C. & Prasad, P. N. Nanophotonics and Nanochemistry: Controlling the Excitation Dynamics for Frequency Up- and Down-Conversion in Lanthanide-Doped Nanoparticles. *Accounts of Chemical Research* **46**, 1474–1486 (2013).
24. Shang, Y., Hao, S., Yang, C. & Chen, G. Enhancing Solar Cell Efficiency Using Photon Upconversion Materials. *Nanomaterials* **5**, 1782–1809 (2015).
25. Brendel, R., Werner, J. H. & Queisser, H. J. Thermodynamic efficiency limits for semiconductor solar cells with carrier multiplication. *Solar Energy Materials and Solar Cells* **41-42**, 419–425 (1996).
26. Conibeer, G. J., König, D., Green, M. A. & Guillemoles, J. F. Slowing of carrier cooling in hot carrier solar cells. *Thin Solid Films* **516**, 6948–6953 (2008).
27. Schaller, R. D., Agranovich, V. M. & Klimov, V. I. High-efficiency carrier multiplication through direct photogeneration of multi-excitons via virtual single-exciton states. *Nature Physics* **1**, 189–194 (2005).
28. Würfel, P., Brown, A. S., Humphrey, T. E. & Green, M. A. Particle conservation in the hot-carrier solar cell. *Progress in Photovoltaics: Research and Applications* **13**, 277–285 (2005).
29. Takeda, Y. *et al.* Hot carrier solar cells operating under practical conditions. *Journal of Applied Physics* **105** (2009).
30. Takeda, Y. *et al.* Practical factors lowering conversion efficiency of hot carrier solar cells. *Applied Physics Express* **3** (2010).
31. Le Bris, A & Guillemoles, J.-F. Hot carrier solar cells: achievable efficiency accounting for heat losses in the absorber and through contacts. *Applied Physics Letters* **97**, 113506 (2010).
32. Aliberti, P. *et al.* Effects of non-ideal energy selective contacts and experimental carrier cooling rate on the performance of an indium nitride based hot carrier solar cell. *Applied Physics Letters* **99**, 2012–2015 (2011).
33. Neges, M., Schwarzburg, K. & Willig, F. Monte Carlo simulation of energy loss and collection of hot charge carriers, first step towards a more realistic hot-carrier solar energy converter. *Solar Energy Materials and Solar Cells* **90**, 2107–2128 (2006).

34. Feng, Y. *et al.* Investigation of carrier-carrier scattering effect on the performance of hot carrier solar cells with relaxation time approximation. *Applied Physics Letters* **102** (2013).
35. Shank, C. V. *et al.* Picosecond Dynamics of Hot Carrier Relaxation in Highly Excited Multi-Quantum Well Structures. English. *Solid State Communications* **47**, 981–983 (1983).
36. Motta, C. *et al.* Revealing the role of organic cations in hybrid halide perovskite  $\text{CH}_3\text{NH}_3\text{PbI}_3$ . *Nature communications* **6**, 7026 (2015).
37. Hata, T., Giorgi, G. & Yamashita, K. The Effects of the Organic–Inorganic Interactions on the Thermal Transport Properties of  $\text{CH}_3\text{NH}_3\text{PbI}_3$ . *Nano letters* **16**, 2749–2753 (2016).
38. Liu, F., Ming, P. & Li, J. Ab initio calculation of ideal strength and phonon instability of graphene under tension. *Physical Review B* **76**, 64120 (2007).
39. Peelaers, H., Partoens, B & Peeters, F. M. Phonon band structure of Si nanowires: a stability analysis. *Nano letters* **9**, 107–111 (2008).
40. Clady, R. *et al.* Interplay between the hot phonon effect and intervalley scattering on the cooling rate of hot carriers in GaAs and InP. English. *Progress in Photovoltaics* **20**, 82–92 (2012).
41. Chen, F., Cartwright, a. N., Lu, H. & Schaff, W. J. Ultrafast carrier dynamics in InN epilayers. *Journal of Crystal Growth* **269**, 10–14 (2004).
42. Jang, D. J. *et al.* Energy relaxation of InN thin films. *Applied Physics Letters* **91**, 1–3 (2007).
43. Hirst, L. C. *et al.* InGaAs/GaAsP quantum wells for hot carrier solar cells. *Physics, Simulation, and Photonic Engineering of Photovoltaic Devices* **8256**, 82560X (2012).
44. Zhang, Y. *et al.* Extended hot carrier lifetimes observed in bulk  $\text{In}_{0.265\pm 0.02}\text{Ga}_{0.735}\text{N}$  under high-density photoexcitation. *Applied Physics Letters* **108**, 0–5 (2016).
45. Nozik, A. J. *et al.* Semiconductor quantum dots and quantum dot arrays and applications of multiple exciton generation to third-generation photovoltaic solar cells. *Chemical Reviews* **110**, 6873–6890 (2010).
46. Pandey, A. & Guyot-Sionnest, P. Slow electron cooling in colloidal quantum dots. *Science* **322**, 929–932 (2008).
47. Mueller, M. L., Yan, X., Dragnea, B. & Li, L. S. Slow hot-carrier relaxation in colloidal graphene quantum dots. *Nano Letters* **11**, 56–60 (2011).
48. Yang, Y. *et al.* Observation of a hot-phonon bottleneck in lead-iodide perovskites. *Nature Photonics* **10**, 53–59 (2016).
49. Zhu, H. *et al.* Screening in crystalline liquids protects energetic carriers in hybrid perovskites. *Science* **353**, 1409–1413 (2016).
50. Zhu, X. Y. & Podzorov, V. Charge carriers in hybrid organic-inorganic lead halide perovskites might be protected as large polarons. *Journal of Physical Chemistry Letters* **6**, 4758–4761 (2015).
51. Wright, A. D. *et al.* Electron–phonon coupling in hybrid lead halide perovskites. *Nature Communications* **7**, 11755 (2016).
52. Mueller, M. L., Yan, X., Dragnea, B. & Li, L.-s. Slow hot-carrier relaxation in colloidal graphene quantum dots. *Nano letters* **11**, 56–60 (2010).

53. Conibeer, G. *et al.* Silicon nanostructures for third generation photovoltaic solar cells. *Thin solid films* **511**, 654–662 (2006).
54. Liao, Y. *et al.* Resonant Tunneling through Monolayer Si Colloidal Quantum Dots and Ge Nanocrystals. *Advanced Functional Materials* **27** (2017).
55. Kirk, A. P. & Fischetti, M. V. Fundamental limitations of hot-carrier solar cells. *Physical Review B* **86**, 16520 (2012).
56. König, D., Yao, Y. & Patterson, R. Shortcomings in efficiency modelling of hot carrier solar cells: Considering device concepts and hot carrier absorber materials from a practical viewpoint. *Japanese Journal of Applied Physics* **53**, 1–5 (2014).
57. Feng, Y. *et al.* Non-ideal energy selective contacts and their effect on the performance of a hot carrier solar cell with an indium nitride absorber. *Applied Physics Letters* **100**, 53502 (2012).
58. Purcell, E. M. Proceedings of the American Physical Society. *Phys. Rev* **69**, 674 (1946).
59. Darvill, D., Centeno, A. & Xie, F. Plasmonic fluorescence enhancement by metal nanostructures: shaping the future of bionanotechnology. *Physical Chemistry Chemical Physics* **15**, 15709–15726 (2013).
60. Vukovic, S., Corni, S. & Mennucci, B. Fluorescence enhancement of chromophores close to metal nanoparticles. Optimal setup revealed by the polarizable continuum model. *The Journal of Physical Chemistry C* **113**, 121–133 (2008).
61. Barnes, W. L. Fluorescence near interfaces: the role of photonic mode density. *Journal of Modern Optics* **45**, 661–699 (1998).
62. Anger, P., Bharadwaj, P. & Novotny, L. Enhancement and quenching of single-molecule fluorescence. *Physical Review Letters* **96**, 3–6 (2006).
63. Altug, H., Englund, D. & Vučković, J. Ultrafast photonic crystal nanocavity laser. *Nature Physics* **2**, 484–488 (2006).
64. Cho, C.-H. *et al.* Tailoring hot-exciton emission and lifetimes in semiconducting nanowires via whispering-gallery nanocavity plasmons. *Nature materials* **10**, 669–675 (2011).
65. Novotny, Lukas; Hecht, B. *Principles of Nano-Optics* 2nd (Cambridge University Press, 2012).
66. Englund, D. *et al.* Controlling the spontaneous emission rate of single quantum dots in a two-dimensional photonic crystal. *Physical Review Letters* **95**, 2–5 (2005).
67. Noda, S., Fujita, M. & Asano, T. Spontaneous-emission control by photonic crystals and nanocavities. *Nature Photonics* **1**, 449–458 (2007).
68. Celanovic, I., O’Sullivan, F., Jovanovic, N., Qi, M. & Kassakian, J. G. 1D and 2D Photonic Crystals for Thermophotovoltaic Applications. *Proc. SPIE 5450, Photonic Crystal Materials and Nanostructures* **5450**, 416–422 (2004).
69. Celanovic, I., Perreault, D. & Kassakian, J. Resonant-cavity enhanced thermal emission. *Physical Review B* **72**, 2–7 (2005).
70. Shugayev, R. & Bermel, P. Core-shell Mie resonant structures for quantum computing applications. *Applied Physics Letters* **109** (2016).
71. Kuttge, M., García De Abajo, F. J. & Polman, A. Ultrasmall mode volume plasmonic nanodisk resonators. *Nano Letters* **10**, 1537–1541 (2010).

72. Min, B. *et al.* High-Q surface-plasmon-polariton whispering-gallery microcavity. *Nature* **457**, 455–458 (2009).
73. Cho, C.-H., Aspetti, C. O., Park, J. & Agarwal, R. Silicon coupled with plasmon nanocavity generates bright visible hot-luminescence. *Nature photonics* **7**, 285–289 (2013).
74. Robinson, J. T., Manolatou, C., Chen, L. & Lipson, M. Ultrasmall mode volumes in dielectric optical microcavities. *Physical Review Letters* **95**, 1–4 (2005).
75. Lampert, Z. E., Papanikolas, J. M. & Lewis Reynolds, C. Enhancement of optical gain and amplified spontaneous emission due to waveguide geometry in the conjugated polymer poly[2-methoxy-5-(2'-ethylhexyloxy)-p-phenylene vinylene]. *Applied Physics Letters* **102**, 073303 (2013).
76. Creatore, C., Andreani, L. C., Miritello, M., Lo Savio, R. & Priolo, F. Modification of erbium radiative lifetime in planar silicon slot waveguides. *Applied Physics Letters* **94**, 35–38 (2009).
77. Kolchin, P. *et al.* High purcell factor due to coupling of a single emitter to a dielectric slot waveguide. *Nano Letters* **15**, 464–468 (2015).
78. Basu, S., Zhang, Z. M. & Fu, C. J. Review of near-field thermal radiation and its application to energy conversion. *International Journal of Energy Research* **33**, 1203–1232 (2009).
79. Joulain, K. Near-field heat transfer: A radiative interpretation of thermal conduction. *Journal of Quantitative Spectroscopy and Radiative Transfer* **109**, 294–304 (2008).
80. Francoeur, M. & Pinar Mengüç, M. Role of fluctuational electrodynamics in near-field radiative heat transfer. *Journal of Quantitative Spectroscopy and Radiative Transfer* **109**, 280–293 (2008).
81. Barnes, W. L., Dereux, A. & Ebbesen, T. W. Surface plasmon subwavelength optics. *Nature* **424**, 824–830 (2003).
82. Rand, B. P., Peumans, P. & Forrest, S. R. Long-range absorption enhancement in organic tandem thin-film solar cells containing silver nanoclusters. *Journal of Applied Physics* **96**, 7519–7526 (2004).
83. Ferry, V. E., Sweatlock, L. A., Pacifici, D. & Atwater, H. A. Plasmonic nanostructure design for efficient light coupling into solar cells. *Nano letters* **8**, 4391–4397 (2008).
84. Atwater, H. A. & Polman, A. Plasmonics for improved photovoltaic devices. *Nature materials* **9**, 205–213 (2010).
85. Bohn, C. D. *et al.* Design considerations for enhancing absorption in semiconductors on metals through surface plasmon polaritons. *Physical chemistry chemical physics : PCCP* **16**, 6084–91 (2014).
86. Wubs, M., Suttorp, L. G. & Lagendijk, A. Multiple-scattering approach to interatomic interactions and superradiance in inhomogeneous dielectrics. *Physical Review A - Atomic, Molecular, and Optical Physics* **70**, 1–17 (2004).
87. Martin, O. J. F., Girard, C. & Dereux, A. Generalized field propagator for electromagnetic scattering and light confinement. *Physical Review Letters* **74**, 526–529 (1995).
88. Di Stefano, O., Savasta, S. & Girlanda, R. Three-dimensional electromagnetic field quantization in absorbing and dispersive bounded dielectrics. *Physical Review A* **61**, 023803 (2000).

## BIBLIOGRAPHY

---

89. De Lasson, J. R., Mørk, J. & Kristensen, P. T. Three-dimensional integral equation approach to light scattering, extinction cross sections, local density of states, and quasi-normal modes. *Journal of the Optical Society of America B* **30**, 1996 (2013).
90. Kristensen, P. T. & Hughes, S. Modes and Mode Volumes of Leaky Optical Cavities and Plasmonic Nanoresonators. *ACS Photonics* **1**, 2–10 (2014).
91. Koenderink, A. F. On the use of Purcell factors for plasmon antennas. *Optics letters* **35**, 4208–4210 (2010).
92. Ge, R.-C. & Hughes, S. Design of an efficient single photon source from a metallic nanorod dimer: a quasi-normal mode finite-difference time-domain approach. *Optics Letters* **39**, 4235 (2014).
93. Ge, R.-C., Kristensen, P. T., Young, J. F. & Hughes, S. Quasinormal mode approach to modelling light-emission and propagation in nanoplasmonics. *New Journal of Physics* **16**, 113048 (2014).
94. Yee, K. S. Numerical solution of initial boundary value problems involving Maxwell's equations in isotropic media. *IEEE Transactions on Antennas and Propagation* **14**, 302–307 (1966).
95. [https://kb.lumerical.com/en/diffractive\\_optics\\_cavity\\_purcell\\_factor.html](https://kb.lumerical.com/en/diffractive_optics_cavity_purcell_factor.html)
96. Van Vlack, C. & Hughes, S. Finite-difference time-domain technique as an efficient tool for calculating the regularized Green function: applications to the local-field problem in quantum optics for inhomogeneous lossy materials. *Optics Letters* **37**, 2880 (2012).
97. Ge, R.-C., Young, J. F. & Hughes, S. Quasi-normal mode approach to the local-field problem in quantum optics. *Optica* **2**, 246 (2015).
98. Kristensen, P. T., Van Vlack, C. & Hughes, S. Generalized effective mode volume for leaky optical cavities. *Optics Letters* **37**, 1649 (2012).
99. <https://www.lumerical.com/tcad-products/fdtd/>
100. Berera, R., van Grondelle, R. & Kennis, J. T. M. Ultrafast transient absorption spectroscopy: Principles and application to photosynthetic systems. *Photosynthesis Research* **101**, 105–118 (2009).
101. Othonos, A. Probing ultrafast carrier and phonon dynamics in semiconductors. *Journal of Applied Physics* **83**, 1789–1830 (1998).
102. Ryan, J. F. *et al.* Time-resolved photoluminescence of two-dimensional hot carriers in GaAs-AlGaAs heterostructures. *Physical Review Letters* **53**, 1841–1844 (1984).
103. Von Der Linde, D. & Lambrich, R. Direct measurement of hot-Electron relaxation by picosecond spectroscopy. *Physical Review Letters* **42**, 1090–1093 (1979).
104. Zanato, D., Balkan, N., Ridley, B. K., Hill, G & Schaff, W. J. Hot electron cooling rates via the emission of LO-phonons in InN. en. *Semiconductor Science and Technology* **19**, 1024–1028 (2004).
105. Xia, H. *et al.* Hot carrier dynamics in HfN and ZrN measured by transient absorption spectroscopy. *Solar Energy Materials and Solar Cells* **150**, 51–56 (2016).
106. Richards, B. S. Luminescent layers for enhanced silicon solar cell performance: Down-conversion. *Solar Energy Materials and Solar Cells* **90**, 1189–1207 (2006).

107. Klimov, V. I. Multicarrier Interactions in Semiconductor Nanocrystals in Relation to the Phenomena of Auger Recombination and Carrier Multiplication. *Annual Review of Condensed Matter Physics* **5**, 285–316 (2014).
108. Stewart, J. T. *et al.* Comparison of carrier multiplication yields in PbS and PbSe nanocrystals: The role of competing energy-loss processes. *Nano Letters* **12**, 622–628 (2012).
109. Trupke, T., Shalav, A., Richards, B. S., Würfel, P. & Green, M. A. Efficiency enhancement of solar cells by luminescent up-conversion of sunlight. *Solar Energy Materials and Solar Cells* **90**, 3327–3338 (2006).
110. Abrams, Z. R., Niv, A. & Zhang, X. Solar energy enhancement using down-converting particles: A rigorous approach. *Journal of Applied Physics* **109**, 1–9 (2011).
111. Abrams, Z. R., Gharghi, M., Niv, A., Gladden, C. & Zhang, X. Theoretical efficiency of 3rd generation solar cells: Comparison between carrier multiplication and down-conversion. *Solar Energy Materials and Solar Cells* **99**, 308–315 (2012).
112. Feng, Y., Shrestha, S., Huang, S. & Conibeer, G. Thermodynamic Efficiency Limits for Optically Boosted Planar Solar Cells. *Physical Review Applied* **2**, 1–6 (2014).
113. Luque, A & Marti, A. Entropy production in photovoltaic conversion. English. *Physical Review B* **55**, 6994–6999 (1997).
114. Hanna, M. C. & Nozik, A. J. Solar conversion efficiency of photovoltaic and photoelectrolysis cells with carrier multiplication absorbers. *Journal of Applied Physics* **100** (2006).
115. Green, M. *Third Generation Photovoltaics: Advanced Solar Energy Conversion* (Springer, 2006).
116. Ruppel, W & Würfel, P. Upper Limit for the Conversion of Solar-Energy. *IEEE Trans. Electron Devices* **27**, 877–882 (1980).
117. Neogi, A. *et al.* Enhancement of spontaneous emission in a quantum well by resonant surface plasmon coupling. *Physical Review B* **66**, 1–4 (2002).
118. Pelton, M. *et al.* An efficient source of single photons: A single quantum dot in a micropost microcavity. *Physica E: Low-Dimensional Systems and Nanostructures* **17**, 1–4 (2002).
119. Mokkalapati, S. *et al.* An Order of Magnitude Increase in the Quantum Efficiency of (Al)GaAs Nanowires Using Hybrid Photonic–Plasmonic Modes. *Nano Letters* **15**, 307–312 (2015).
120. Bhattacharya, R., Pal, B. & Bansal, B. On conversion of luminescence into absorption and the van Roosbroeck-Shockley relation. *Applied Physics Letters* **100**, 1–4 (2012).
121. Yablonovitch, E. Inhibited spontaneous emission in solid-state physics and electronics. *Physical Review Letters* **58**, 2059–2062 (1987).
122. Yu, P. Y. & Cardona, M. *Fundamentals of semiconductors: physics and materials properties* (Springer, 2010).
123. Callahan, D. M., Munday, J. N. & Atwater, H. A. Solar Cell Light Trapping beyond the Ray Optic Limit. *Nano Letters* **12**, 214–218 (2012).
124. Lodahl, P. *et al.* Controlling the dynamics of spontaneous emission from quantum dots by photonic crystals. *Nature* **430**, 654–657 (2004).

125. Rogobete, L., Kaminski, F., Agio, M. & Sandoghdar, V. Design of plasmonic nanoantennae for enhancing spontaneous emission. *Optics letters* **32**, 1623–1625 (2007).
126. Filonenko, K., Willatzen, M. & Bordo, V. Purcell effect for finite-length metal-coated and metal nanowires. *Opticsinfobase.Org* **31**, 2002–2011 (2014).
127. Knig, D. *et al.* Hot carrier solar cells: Principles, materials and design. *Physica E: Low-Dimensional Systems and Nanostructures* **42**, 2862–2866 (2010).
128. Ellingson, R. J. *et al.* Highly Efficient Multiple Excitation Generation in Colloidal PbSe and PbS Quantum Dots. *Nano Letters* **5**, 865–871 (2005).
129. Franceschetti, A., An, J. M. & Zunger, A. Impact ionization can explain carrier multiplication in PbSe quantum dots. *Nano Letters* **6**, 2191–2195 (2006).
130. Fu, Y., Zhou, Y.-H., Su, H., Boey, F. Y. C. & Ågren, H. Impact Ionization and Auger Recombination Rates in Semiconductor Quantum Dots. *The Journal of Physical Chemistry C* **114**, 3743–3747 (2010).
131. Hanna, M. C., Beard, M. C. & Nozik, A. J. Effect of solar concentration on the thermodynamic power conversion efficiency of quantum-dot solar cells exhibiting multiple exciton generation. *Journal of Physical Chemistry Letters* **3**, 2857–2862 (2012).
132. Yang, Y. *et al.* Up-conversion luminescence and near-infrared quantum cutting in Dy<sup>3+</sup>, Yb<sup>3+</sup> co-doped BaGd<sub>2</sub>ZnO<sub>5</sub> nanocrystal. *Journal of Luminescence* **146**, 284–287 (2014).
133. Florêncio, L. d. A. *et al.* Efficiency enhancement in solar cells using photon down-conversion in Tb/Yb-doped tellurite glass. *Solar Energy Materials and Solar Cells* **157**, 468–475 (2016).
134. Liu, Z. *et al.* Efficient near-infrared quantum cutting in Ce<sup>3+</sup>-Yb<sup>3+</sup> codoped glass for solar photovoltaic. *Solar Energy Materials and Solar Cells* **122**, 46–50 (2014).
135. Monguzzi, A. *et al.* Broadband up-conversion at subsolar irradiance: Triplet-triplet annihilation boosted by fluorescent semiconductor nanocrystals. *Nano Letters* **14**, 6644–6650 (2014).
136. Feng, Y. *et al.* Non-ideal energy selective contacts and their effect on the performance of a hot carrier solar cell with an indium nitride absorber. *Applied Physics Letters* **100**, 2010–2014 (2012).
137. Léonard, F. & Talin, A. A. Electrical contacts to one- and two-dimensional nanomaterials. *Nature Nanotechnology* **6**, 773–783 (2011).
138. Pandey, A. & Guyot-Sionnest, P. Hot electron extraction from colloidal quantum dots. *Journal of Physical Chemistry Letters* **1**, 45–47 (2010).
139. Semonin, O. E. *et al.* Peak External Photocurrent Quantum Efficiency Exceeding 100% via MEG in a Quantum Dot Solar Cell. *Science* **334**, 1530–1533 (2011).
140. Kamat, P. V. Quantum Dot Solar Cells. Semiconductor Nanocrystals as Light Harvesters†. *J. Phys. Chem. C* **112**, 18737–18753 (2008).
141. Kamat, P. V. Quantum Dot Solar Cells. The Next Big Thing in Photovoltaics. *The Journal of Physical Chemistry Letters* **4**, 908–918 (2013).
142. Niv, A., Gharghi, M., Gladden, C., Miller, O. D. & Zhang, X. Near-field electromagnetic theory for thin solar cells. *Physical Review Letters* **109** (2012).
143. Sumetsky, M. Mode localization and the Q-factor of a cylindrical microresonator. *Optics letters* **35**, 2385–2387 (2010).

144. Schley, P *et al.* Dielectric function and Van Hove singularities for In-rich  $\text{In}_x\text{Ga}_{1-x}\text{N}$  alloys: Comparison of N-and metal-face materials. *Physical Review B* **75**, 205204 (2007).
145. Goldhahn, R. *et al.* Anisotropy of the dielectric function for wurtzite InN. *Superlattices and Microstructures* **36**, 591–597 (2004).
146. Palik, E. *Handbook of Optical Constants of Solids* 1st, 547–569 (Academic press, 1997).
147. Johnson, P. B. & Christy, R. W. Optical Constants of the Noble Metals. *Physical Review B* **6**, 4370–4379 (1972).
148. Eckhardt, W. *First and second fluctuation-dissipation-theorem in electromagnetic fluctuation theory* 1982.
149. Gao, Y. *et al.* Analytical model for plasmon modes in graphene-coated nanowire. EN. *Optics Express* **22**, 24322 (2014).
150. Liu, R. *et al.* Graphene plasmon enhanced photoluminescence in ZnO microwires. *Nanoscale* **5**, 5294 (2013).
151. Farrell, D. J., Sodabanlu, H., Wang, Y., Sugiyama, M. & Okada, Y. Can a hot-carrier solar cell also be an efficient up-converter? *IEEE Journal of Photovoltaics* **5**, 571–576 (2015).
152. Jeon, N. J. *et al.* Solvent engineering for high-performance inorganic-organic hybrid perovskite solar cells. *Nature materials* **13**, 897–903 (2014).
153. Nie, W. *et al.* High-efficiency solution-processed perovskite solar cells with millimeter-scale grains. *Science* **347**, 522–525 (2015).
154. Saliba, M. *et al.* Cesium-containing triple cation perovskite solar cells: Improved stability, reproducibility and high efficiency. *Energy Environ. Sci.* **9**, 1989–1997 (2016).
155. Green, M. A., Ho-Baillie, A. & Snaith, H. J. The emergence of perovskite solar cells. en. *Nature Photonics* **8**, 506–514 (2014).
156. Wen, X. *et al.* Morphology and carrier extraction study of organic-inorganic metal halide perovskite by one- and two-photon fluorescence microscopy. *The Journal of Physical Chemistry Letters* **5**, 3849–3853 (2014).
157. Price, M. B. *et al.* Hot-carrier cooling and photoinduced refractive index changes in organic-inorganic lead halide perovskites. en. *Nature communications* **6**, 8420 (2015).
158. Langot, P, Del Fatti, N, Christofilos, D, Tommasi, R & Vallee, F. Femtosecond investigation of the hot-phonon effect in GaAs at room temperature. *Physical Review B* **54**, 14487–14493 (1996).
159. Murdin, B., Heiss, W, Langerak, C & Lee, S. Direct observation of the LO phonon bottleneck in wide GaAs/ $\text{Al}_x\text{Ga}_{1-x}\text{As}$  quantum wells. *Physical Review B* **55**, 5171–5176 (1997).
160. Pötz, W. Hot-phonon effects in bulk GaAs. *Physical Review B* **36**, 5016–5019 (1987).
161. Huang, F. *et al.* Gas-assisted preparation of lead iodide perovskite films consisting of a monolayer of single crystalline grains for high efficiency planar solar cells. *Nano Energy* **10**, 10–18 (2014).

162. Sheng, R. *et al.* Methylammonium lead bromide perovskite-based solar cells by vapour-assisted deposition. *The Journal of Physical Chemistry C* **119**, 3545–3549 (2015).
163. Ma, Q., Huang, S., Wen, X., Green, M. A. & Ho-Baillie, A. W. Y. Hole transport layer free inorganic CsPbIBr<sub>2</sub> perovskite solar cell by dual source thermal evaporation. *Advanced Energy Materials* **6**, 1502202 (2016).
164. Kim, J. *et al.* Nucleation and growth control of HC(NH<sub>2</sub>)<sub>2</sub>PbI<sub>3</sub> for planar perovskite solar cell. *The Journal of Physical Chemistry C* **120**, 11262–11267 (2016).
165. Yang, Y. *et al.* Comparison of recombination dynamics in CH<sub>3</sub>NH<sub>3</sub>PbBr<sub>3</sub> and CH<sub>3</sub>NH<sub>3</sub>PbI<sub>3</sub> perovskite films: Influence of exciton binding energy. *Journal of Physical Chemistry Letters* **6**, 4688–4692 (2015).
166. Manser, J. S. & Kamat, P. V. Band filling with free charge carriers in organometal halide perovskites. *Nature Photonics* **8**, 737–743 (2014).
167. Sharma, V. *et al.* New insights into exciton binding and relaxation from high time resolution ultrafast spectroscopy of CH<sub>3</sub>NH<sub>3</sub>PbI<sub>3</sub> and CH<sub>3</sub>NH<sub>3</sub>PbBr<sub>3</sub> films. *Journal of Materials Chemistry A: Materials for energy and sustainability* **00**, 1–8 (2016).
168. Wang, X. *et al.* Cesium lead halide perovskite triangular nanorods as high-gain medium and effective cavities for multiphoton-pumped lasing. *Nano Research*, 1–11 (2017).
169. Kawai, H., Giorgi, G., Marini, A. & Yamashita, K. The mechanism of slow hot-hole cooling in lead-iodide perovskite: First-principles calculation on carrier lifetime from electron-phonon interaction. *Nano Letters* **15**, 3103–3108 (2015).
170. Chang, Y. H., Park, C. H. & Matsuishi, K. First-principles study of the structural and the electronic properties of the lead-halide-based inorganic-organic perovskites (CH<sub>3</sub>NH<sub>3</sub>)PbX<sub>3</sub> and CsPbX<sub>3</sub> (X = Cl, Br, I). English. *Journal of the Korean Physical Society* **44**, 889–893 (2004).
171. Wen, X. *et al.* Defect trapping states and charge carrier recombination in organic–inorganic halide. *Journal of Materials Chemistry C* **4**, 793–800 (2015).
172. Zhang, B. & Yang, J. A simulation study of the micro-grooved electrode structure for back-contact back-junction silicon solar cell. *Japanese Journal of Applied Physics* **54**, 014301 (2015).
173. Beard, M. C. Multiple exciton generation in semiconductor quantum dots. *Journal of Physical Chemistry Letters* **2**, 1282–1288 (2011).
174. Yang, Y. *et al.* Low surface recombination velocity in solution-grown CH<sub>3</sub>NH<sub>3</sub>PbBr<sub>3</sub> perovskite single crystal. en. *Nature communications* **6**, 7961 (2015).
175. Conibeer, G. *et al.* Progress on hot carrier cells. *Solar Energy Materials and Solar Cells* **93**, 713–719 (2009).
176. Hejda, B. & Kral, K. Hot-electron cooling and second-generation phonons in polar semiconductors. *Physical Review B* **47**, 15554–15561 (1993).
177. Brivio, F., Butler, K. T., Walsh, A. & van Schilfgaarde, M. Relativistic quasiparticle self-consistent electronic structure of hybrid halide perovskite photovoltaic absorbers. *Physical Review B* **89**, 155204 (2014).
178. Frost, J. M. *et al.* Atomistic origins of high-performance in hybrid halide perovskite solar cells. *Nano Letters* **14**, 2584–2590 (2014).

179. Mosconi, E., Amat, A., Nazeeruddin, M. K., Grätzel, M. & De Angelis, F. First-principles modeling of mixed halide organometal perovskites for photovoltaic applications. *Journal of Physical Chemistry C* **117**, 13902–13913 (2013).
180. Motta, C. *et al.* Revealing the role of organic cations in hybrid halide perovskite  $\text{CH}_3\text{NH}_3\text{PbI}_3$ . *Nature communications* **6**, 7026 (2015).
181. Quarti, C. *et al.* The raman spectrum of the  $\text{CH}_3\text{NH}_3\text{PbI}_3$  hybrid perovskite: Interplay of theory and experiment. *Journal of Physical Chemistry Letters* **5**, 279–284 (2014).
182. Pérez-Osorio, M. A. *et al.* Vibrational Properties of the Organic-Inorganic Halide Perovskite  $\text{CH}_3\text{NH}_3\text{PbI}_3$  from Theory and Experiment: Factor Group Analysis, First-Principles Calculations, and Low-Temperature Infrared Spectra. *Journal of Physical Chemistry C* **119**, 25703–25718 (2015).
183. Caretta, A. *et al.* Measurement of the acoustic-to-optical phonon coupling in multicomponent systems. *Physical Review B* **91**, 1–6 (2015).
184. Ridley, B. K. Hot phonons in high-field transport. *Semiconductor Science and Technology* **4**, 1142–1150 (1999).
185. Ledinský, M. *et al.* Raman spectroscopy of organic-inorganic halide perovskites. *The journal of physical chemistry letters* **6**, 401–406 (2015).
186. Kunugita, H. *et al.* Excitonic feature in hybrid perovskite  $\text{CH}_3\text{NH}_3\text{PbBr}_3$  single crystals. *Chemistry Letters* **44**, 852–854 (2015).
187. Yunakova, O. N., Miloslavskii, V. K. & Kovalenko, E. N. Exciton absorption spectrum of thin  $\text{CsPbI}_3$  and  $\text{Cs}_4\text{PbI}_6$  films. *Optics and Spectroscopy* **112**, 91–96 (2012).
188. Sebastian, M. *et al.* Excitonic emissions and above-band-gap luminescence in the single-crystal perovskite semiconductors  $\text{CsPbBr}_3$  and  $\text{CsPbCl}_3$ . *Physical Review B* **92**, 235210 (2015).
189. Pisoni, A., Baris, O. S., Spina, M. & Gaa, R. Ultra-Low Thermal Conductivity in Organic-Inorganic Hybrid. *J. Phys. Chem. Lett.* **5**, 2488–2492 (2014).
190. Wang, M. & Lin, S. Anisotropic and ultralow phonon thermal transport in organic-inorganic hybrid perovskites: Atomistic insights into solar cell thermal management and thermoelectric energy conversion efficiency. *Advanced Functional Materials* **26**, 5297–5306 (2016).
191. Kubičár, L., Boháč, V & Nitsch, K. Thermophysical properties of the  $\text{CsPbCl}_3$  single crystal using pulse transient method. *International Journal of Thermophysics* **21**, 571–583 (2000).
192. Whalley, L. D., Skelton, J. M., Frost, J. M. & Walsh, A. Phonon anharmonicity, lifetimes, and thermal transport in  $\text{CH}_3\text{NH}_3\text{PbI}_3$  from many-body perturbation theory. *Physical Review B* **94**, 1–5 (2016).
193. Yang, R. X., Skelton, J. M., da Silva, E. L., Frost, J. M. & Walsh, A. Spontaneous Octahedral Tilting in the Cubic Inorganic Caesium Halide Perovskites  $\text{CsSnX}_3$  and  $\text{CsPbX}_3$  (X= F, Cl, Br, I). *arXiv preprint arXiv:1708.00499* (2017).
194. Brivio, F. *et al.* Lattice dynamics and vibrational spectra of the orthorhombic, tetragonal, and cubic phases of methylammonium lead iodide. *Physical Review B - Condensed Matter and Materials Physics* **92**, 1–8 (2015).
195. Patterson, R. *et al.* Phonon lifetimes in model quantum dot superlattice systems with applications to the hot carrier solar cell. *Solar Energy Materials and Solar Cells* **94**, 1931–1935 (2010).

## BIBLIOGRAPHY

---

196. Conibeer, G. *et al.* Hot carrier solar cell absorber prerequisites and candidate material systems. *Solar Energy Materials and Solar Cells* **135**, 124–129 (2015).
197. Svizhenko, A, Bandyopadhyay, S & Stroschio, M. The effect of acoustic phonon confinement on the momentum and energy relaxation of hot carriers in quantum wires. *J. Phys.: Condens. Matter* **10**, 6091 (1998).
198. Campos, V. B., Das Sarma, S. & Stroschio, M. A. Phonon-confinement effect on electron energy loss in one-dimensional quantum wires. *Physical Review B* **46**, 3849–3853 (1992).
199. Qian, X., Gu, X. & Yang, R. Lattice thermal conductivity of organic-inorganic hybrid perovskite  $\text{CH}_3\text{NH}_3\text{PbI}_3$ . **063902**, 3–8 (2015).
200. Xia, H *et al.* Numerical calculation of optical phonon decay rate in InN/GaN MQW. *IOP Conference Series: Materials Science and Engineering* **68**, 012009 (2014).
201. Yang, J. *et al.* Selective optical contacting for solar spectrum management in *Proc. of SPIE Vol* **10099** (2017), 1009911–1009917.
202. Martin, P. A. *Multiple scattering: interaction of time-harmonic waves with N obstacles* (Cambridge University Press, 2006).
203. Leung, P. T., Liu, S. Y. & Young, K. Completeness and time-independent perturbation of the quasinormal modes of an absorptive and leaky cavity. *Physical Review A* **49**, 3982–3989 (1994).
204. Sheng, R. *et al.* Methylammonium Lead Bromide Perovskite-Based Solar Cells by Vapor-Assisted Deposition. *The Journal of Physical Chemistry C* **119**, 3545–3549 (2015).
205. Jiang, Y. *et al.* Time-resolved fluorescence anisotropy study of organic lead halide perovskite. *Solar Energy Materials and Solar Cells* **151**, 102–112 (2016).
206. Giannozzi, P. *et al.* Quantum ESPRESSO: a modular and open-source software project for quantum simulations of materials. *Journal of Physics: Condensed Matter* **21**, 395–502 (2009).
207. Perdew, J. P., Ernzerhof, M. & Burke, K. Rationale for mixing exact exchange with density functional approximations. *The Journal of Chemical Physics* **105**, 9982 (1996).
208. Giannozzi, P., De Gironcoli, S., Pavone, P. & Baroni, S. Ab initio calculation of phonon dispersions in semiconductors. *Physical Review B* **43**, 7231–7242 (1991).

# Appendix A

## Quasi-normal mode method

### A.1 Symbolic and formula conventions of electromagnetics

We only consider a non-magnetic environment in this thesis. Then the source-free Maxwell equation of electric fields and corresponding Green's dyadic function are defined below [93].

$$\nabla \times \nabla \times \mathbf{E}(\mathbf{r}; \omega) - k_0^2 \varepsilon(\mathbf{r}; \omega) \mathbf{E}(\mathbf{r}; \omega) = 0 \quad (\text{A.1})$$

$$\nabla \times \nabla \times \mathbf{G}(\mathbf{r}, \mathbf{r}_0; \omega) - k_0^2 \varepsilon(\mathbf{r}; \omega) \mathbf{G}(\mathbf{r}, \mathbf{r}_0; \omega) = k_0^2 \mathbf{I} \delta(\mathbf{r} - \mathbf{r}_0) \quad (\text{A.2})$$

, where  $k_0 = \omega/c$  is the free-space wave number,  $\varepsilon(\mathbf{r}; \omega)$  the dielectric function of the medium,  $\mathbf{I}$  is the unit dyad and  $\delta(\mathbf{r} - \mathbf{r}_0)$  is the Dirac delta function. Using the volume-integral method [65], the excitations of electric  $\mathbf{E}$  and magnetic  $\mathbf{H}$  field are given below, where  $\mathbf{E}_0$  and  $\mathbf{H}_0$  are the background fields.

$$\mathbf{E}(\mathbf{r}; \omega) = \mathbf{E}_0(\mathbf{r}; \omega) + \int d\mathbf{r}_0^3 \frac{\mathbf{G}(\mathbf{r}, \mathbf{r}_0; \omega) \mathbf{p}(\mathbf{r}_0; \omega)}{\varepsilon_0} \quad (\text{A.3})$$

$$\mathbf{H}(\mathbf{r}; \omega) = \mathbf{H}_0(\mathbf{r}; \omega) - \int d\mathbf{r}_0^3 i \frac{c^2}{\omega} [\nabla \times \mathbf{G}(\mathbf{r}, \mathbf{r}_0; \omega)] \mathbf{p}(\mathbf{r}_0; \omega) \quad (\text{A.4})$$

### A.2 Quasi-normal mode

When a resonant system is ideal without any energy losses, Eq. (A.1) is Hermitian with a series of discrete normal mode solutions whose resonant frequencies are real and positive [65].

However, outgoing wave boundary conditions, also known as the Sommerfeld radiation condition [202], must exist in practice which allows optical fields to escape to the far-field. Besides, local dissipations may also happen inside the resonant. Both aspects make the resonant modes always have a finite lifetime characterized by a finite quality factor  $Q$ .

The so-called quasi-normal mode (QNM)s  $\tilde{\mathbf{f}}_\mu(\mathbf{r})$  are the solutions of Eq. (A.1) when the above two situations occur, where the subscript  $\mu$  is the modal index. Different to normal modes, the QNM have two distinct features. First, the QNM has a complex resonant frequency  $\tilde{\omega}_\mu = \omega_\mu - i\gamma_\mu$ , whose quality factor is then written as  $Q = \omega_\mu/2\gamma_\mu$ ; second, its amplitude will diverge exponentially as  $\mathbf{r} \rightarrow \infty$  [90]. To deal with the above two features, a special normalization formula Eq.(A.5) has to be applied [93, 203].

$$\begin{aligned} \langle\langle \tilde{\mathbf{f}}_\mu | \tilde{\mathbf{f}}_\mu \rangle\rangle &= \lim_{V \rightarrow \infty} \int_V \left[ \frac{1}{2\omega} \frac{\partial (\varepsilon(\mathbf{r}, \omega)\omega^2)}{\partial \omega} \right]_{\omega=\tilde{\omega}_\mu} \tilde{\mathbf{f}}_\mu(\mathbf{r}) \cdot \tilde{\mathbf{f}}_\mu(\mathbf{r}) d\mathbf{r} \\ &+ i \frac{n_{\text{BC}}}{2\tilde{\omega}_\mu} \int_{\partial V} \tilde{\mathbf{f}}_\mu(\mathbf{r}) \cdot \tilde{\mathbf{f}}_\mu(\mathbf{r}) = 1 \end{aligned} \quad (\text{A.5})$$

Eq.(A.5) have both the volume ( $V$ ) and surface ( $\partial V$ ) integrals, where  $n_{\text{B}}$  is the background refractive index at the selected integral boundary. By adding the surface term, Eq.(A.5) has a stable numerical behavior when arbitrarily increase the integral boundary and normalize the field profile  $\tilde{\mathbf{f}}_\mu$  properly[93, 98]. Then normalized mode profile constructs the transverse Green's function of a single QNM inside and near the resonator as below<sup>1</sup> [93]. The prefactor  $\frac{\omega^2}{2\tilde{\omega}_\mu(\tilde{\omega}_\mu - \omega)}$  corresponds to the spectrum profile function  $W(\omega, \omega_\mu)$  mentioned in the main text.

$$\mathbf{G}_\mu(\mathbf{r}_1, \mathbf{r}_2; \omega) \equiv \frac{\omega^2}{2\tilde{\omega}_\mu(\tilde{\omega}_\mu - \omega)} \tilde{\mathbf{f}}_\mu(\mathbf{r}_1) \otimes \tilde{\mathbf{f}}_\mu(\mathbf{r}_2) \quad (\text{A.6})$$

The self-consistency and accuracy of the resulted Green's function have been intensively verified in different nano-optical problems [90, 92, 93, 97, 98]. Since the QNM is defined on the complex frequency plan, a special designed Gaussian windowing function has to be applied on the time-domain monitor in the finite-difference time-domain (FDTD) simulations to obtain its numerical results [92]. This Gaussian windowing function is defined based on the complex resonant frequency  $\tilde{\omega}_\mu = \omega_\mu - i\gamma_\mu$  of a certain QNM, whose time offset is  $t_{\text{off}} = 4\pi/\omega_\mu$  while variances is  $\tau_{\text{win}}^2 = t_{\text{off}}^2/\gamma_\mu$ . Once we obtain the mode profiles of QNM, normalization needs to be done according to Eq. (A.5). Then the Green's function is constructed using Eq. (A.6).

---

<sup>1</sup> $\otimes$  means outer product

## Appendix B

# LDOS and photon transfer spectrum

The following derivations are based on the Appendix in Ref. [88].

We start with the transverse Green's function  $\mathbf{G}$  constructed by the quasi-normal mode (QNM) method. The transverse part of Maxwell's equation written by the dyadic component of Green's function is given as

$$\nabla_{\mathbf{r}''}^2 G_{ji}(\mathbf{r}'', \mathbf{r}; \omega) - k_0^2 \varepsilon(\mathbf{r}'') G_{ji}(\mathbf{r}'', \mathbf{r}; \omega) = k_0^2 \delta_{ji}^T \delta(\mathbf{r} - \mathbf{r}'') \quad (\text{B.1})$$

, where  $k_0$  is the free space wave vector,  $\varepsilon$  is the dielectric function at the field point  $\mathbf{r}''$ ,  $\delta_{ji}^T = \delta_{ji} - k_i k_j / k^2$  is the so-called transverse delta function defined in Ref. [88],  $\nabla_{\mathbf{r}''}^2$  is the Laplace operator acting on  $\mathbf{r}''$ . Noting that the commutation relation  $G_{ij}(\mathbf{r}, \mathbf{r}''; \omega) = G_{ji}(\mathbf{r}'', \mathbf{r}; \omega) \propto \tilde{f}_i(\mathbf{r}) \tilde{f}_j(\mathbf{r}'')$  is still held for the Green's function of QNM, we can rewrite Eq. (B.1) as

$$\nabla_{\mathbf{r}''}^2 G_{ij}(\mathbf{r}, \mathbf{r}''; \omega) - k_0^2 \varepsilon(\mathbf{r}'') G_{ij}(\mathbf{r}, \mathbf{r}''; \omega) = k_0^2 \delta_{ij}^T \delta(\mathbf{r} - \mathbf{r}'') \quad (\text{B.2})$$

Multiply  $G_{i'j}^*(\mathbf{r}', \mathbf{r}'')$  on both sides of Eq. (B.2) and integrate over  $\mathbf{r}''$ , we then have

$$\begin{aligned} & \int_V d\mathbf{r}''^3 \nabla_{\mathbf{r}''}^2 G_{ij}(\mathbf{r}, \mathbf{r}''; \omega) \cdot G_{i'j}^*(\mathbf{r}', \mathbf{r}''; \omega) - k_0^2 \int_V d\mathbf{r}''^3 \varepsilon(\mathbf{r}'') G_{ij}(\mathbf{r}, \mathbf{r}''; \omega) \cdot G_{i'j}^*(\mathbf{r}', \mathbf{r}''; \omega) \\ & = k_0^2 \int_V d\mathbf{r}''^3 \delta_{ij}^T(\mathbf{r} - \mathbf{r}'') \cdot G_{i'j}^*(\mathbf{r}', \mathbf{r}''; \omega) \end{aligned} \quad (\text{B.3})$$

Now, using the integral by part to split the first part of the left-hand-side of Eq. (B.3) as

below

$$\begin{aligned} & \int_{\partial V} d\mathbf{r}''^2 \hat{\mathbf{n}} \cdot \nabla_{\mathbf{r}''} G_{ij}(\mathbf{r}, \mathbf{r}''; \omega) \cdot G_{i'j}^*(\mathbf{r}', \mathbf{r}''; \omega) - \int_V d\mathbf{r}''^3 \nabla_{\mathbf{r}''} G_{ij}(\mathbf{r}, \mathbf{r}''; \omega) \cdot \nabla_{\mathbf{r}''} G_{i'j}^*(\mathbf{r}', \mathbf{r}''; \omega) \\ & - k_0^2 \int_V d\mathbf{r}''^3 \varepsilon(\mathbf{r}'') G_{ij}(\mathbf{r}, \mathbf{r}''; \omega) \cdot G_{i'j}^*(\mathbf{r}', \mathbf{r}''; \omega) = k_0^2 \int_V d\mathbf{r}''^3 \delta_{ij}^T(\mathbf{r} - \mathbf{r}'') \cdot G_{i'j}^*(\mathbf{r}', \mathbf{r}''; \omega) \end{aligned} \quad (\text{B.4})$$

Take the complex conjugation of Eq (B.4), exchange  $\mathbf{r}$  to  $\mathbf{r}'$ ,  $i$  to  $i'$ , and then subtract back with Eq (B.4), we finally reach our destination in Eq. (B.5).

$$\begin{aligned} M_{ii'}^j(\mathbf{r}, \mathbf{r}') - 2ik_0^2 \int_V d\mathbf{r}''^3 \varepsilon''(\mathbf{r}'') G_{i'j}^*(\mathbf{r}', \mathbf{r}''; \omega) G_{ij}(\mathbf{r}, \mathbf{r}''; \omega) \\ = k_0^2 [G_{i'i}^*(\mathbf{r}', \mathbf{r}; \omega) - G_{ii'}(\mathbf{r}, \mathbf{r}'; \omega)] \end{aligned} \quad (\text{B.5})$$

, where  $\varepsilon''$  is the imaginary part of the dielectric function,  $M_{ii'}^j(\mathbf{r}, \mathbf{r}')$  comes from the surface integral above written as

$$\begin{aligned} M_{ii'}^j(\mathbf{r}, \mathbf{r}') = \int_{\partial V} d\mathbf{r}''^2 \hat{\mathbf{n}} \cdot \nabla_{\mathbf{r}''} G_{ij}(\mathbf{r}, \mathbf{r}''; \omega) \cdot G_{i'j}^*(\mathbf{r}', \mathbf{r}''; \omega) \\ - \int_{\partial V} d\mathbf{r}''^2 \hat{\mathbf{n}} \cdot \nabla_{\mathbf{r}''} G_{i'j}^*(\mathbf{r}', \mathbf{r}''; \omega) \cdot G_{ij}(\mathbf{r}, \mathbf{r}''; \omega) \end{aligned} \quad (\text{B.6})$$

We can then rewrite the integral of Green's function in the photon transfer spectrum  $\chi_{e-r}$  according to Eq. (B.5) by considering  $\mathbf{r} = \mathbf{r}'$ ,  $\mathbf{r}'' = \mathbf{r}_0$ ,  $i = i'$ ,  $j = m$  as below, where the relationship between the projected local density of optical states (LDOS)  $\rho_i$  and local Green's function  $\rho_i = \frac{6}{\pi\omega} \text{Im} \{G_{ii}(\mathbf{r}, \mathbf{r}; \omega)\}$  has been applied.

$$\int_{V_e} d\mathbf{r}_0^3 G_{im}(\mathbf{r}, \mathbf{r}_0; \omega) \varepsilon_e''(\mathbf{r}_0; \omega) G_{im}^*(\mathbf{r}, \mathbf{r}_0; \omega) = \text{Im} \{G_{ii}(\mathbf{r}, \mathbf{r}; \omega)\} - \frac{i}{2k_0^2} M_{ii}^m(\mathbf{r}, \mathbf{r}) \quad (\text{B.7})$$

$$\begin{aligned} \chi_{e-r} &= \frac{2}{\pi} \int_{V_r} d\mathbf{r}^3 \varepsilon_r''(\mathbf{r}; \omega) \int_{V_e} d\mathbf{r}_0^3 G_{im}(\mathbf{r}, \mathbf{r}_0; \omega) \varepsilon_e''(\mathbf{r}_0; \omega) G_{im}^*(\mathbf{r}, \mathbf{r}_0; \omega) \\ &= \frac{2}{\pi} \int_{V_r} d\mathbf{r}^3 \varepsilon_r''(\mathbf{r}; \omega) \left[ \text{Im} \{G_{ii}(\mathbf{r}, \mathbf{r}; \omega)\} - \frac{i}{2k_0^2} M_{ii}^m(\mathbf{r}, \mathbf{r}; \omega) \right] \\ &= \frac{2}{\pi} \int_{V_r} d\mathbf{r}^3 \varepsilon_r''(\mathbf{r}; \omega) \left[ \frac{\pi\omega\rho_i(\mathbf{r}; \omega)}{6} - \frac{i}{2k_0^2} M_{ii}^m(\mathbf{r}, \mathbf{r}; \omega) \right] \\ &= \frac{\omega}{3} \int_{V_r} d\mathbf{r}^3 \varepsilon_r''(\mathbf{r}; \omega) \rho_i(\mathbf{r}; \omega) - \frac{i}{\pi k_0^2} \int_{V_r} d\mathbf{r}^3 \varepsilon_r''(\mathbf{r}; \omega) M_{ii}^m(\mathbf{r}, \mathbf{r}; \omega) \\ &= \frac{\omega}{3} \int_{V_r} d\mathbf{r}^3 \varepsilon_r''(\mathbf{r}; \omega) \rho_i(\mathbf{r}; \omega) - \hat{S}(\mathbf{r}; \omega) \end{aligned} \quad (\text{B.8})$$

## Appendix C

# Methods of transient absorption characterization of lead-halide perovskites

### Contribution Statement:

Many talented collaborators contribute this perovskite work.

Dr. Xiaoming Wen conceived the project;

Mr. Jianfeng Yang, the author of the thesis, analyzed experimental results with assistance from Dr. Xiaoming Wen, Dr. Hongze Xia, and Dr. Robert Patterson;

Mr. Jianfeng Yang and Dr. Hongze Xia performed theoretical calculations, particularly, Dr. Hongze Xia contributed significantly to the first-principle calculation of phonon band structures;

Dr. Xiaoming Wen performed experiments with assistance from Dr. Patrick Tapping, Dr. Takaaki Harada and Prof. Tak W. Kee at the University of Adelaide;

Dr. Rui Sheng, Mr. Qingshan Ma, Mr. Jincheol Kim, and Dr. Fuzhi Huang (Wuhan University of Technology) fabricated samples;

Prof. Gavin Conibeer, Prof. Martin Green, Prof. Yi-Bing Cheng (Monash University), Dr. Antia Ho-Baillie, Dr. Shujuan Huang, Dr. Santosh Shrestha and all the other collaborators above contributed to the discussion of results.

### C.1 Sample preparation

**FAPbI<sub>3</sub>:**

To prepare 1.2 M  $\text{HC}(\text{NH}_2)_2\text{PbI}_3$  solution,  $\text{HC}(\text{NH}_2)_2\text{I}$  is mixed with  $\text{PbI}_2$  in dimethylformamide (DMF) at 1:1 mole ratio at room temperature. The solutions with added HI at specific molar ratio (0.10 g of HI solution 1 ml of perovskite solution) were spread on borosilicate glass and spun at 6500 rpm for 30 s using gas-assisted method [164]. The films were dried on a hot plate at 160 °C for 20 min.

#### **MAPbBr<sub>3</sub>:**

All samples were deposited on borosilicate glass substrates. The substrates were cleaned by 2% Hellmanex detergent, acetone, and isopropanol in an ultrasonic bath for 10 min in each cleaning agent followed by UVO treatment for 10 min. All  $\text{CH}_3\text{NH}_3\text{PbBr}_3$  films were fabricated by vapor-assisted method [204]. First,  $\text{PbBr}_2$  solution in DMF with a concentration of 1 M was spin-coated on a glass substrate at 2000 rpm for 60 s. After annealing at 70 °C for 30 min, the film was treated by  $\text{CH}_3\text{NH}_3\text{Br}$  vapor at 175 °C for 10 min in a closed glass Petri-dish with  $\text{CH}_3\text{NH}_3\text{Br}$  powder surrounded on a hot plate in a glovebox, then rinsed in isopropanol at room temperature, followed by drying in a nitrogen stream.

#### **MAPbI<sub>3</sub>:**

Unless specified otherwise, all materials were purchased from either Alfa Aesar or Sigma-Aldrich and used as received.  $\text{CH}_3\text{NH}_3\text{I}$  was synthesized by mixing 24 ml  $\text{CH}_3\text{NH}_3$  (33% in ethanol) and 10 ml HI (57% in water) in 100 ml ethanol. After stirring for 2 h, the solvent was removed on a rotary evaporator. The white crystals were dried in a vacuum oven at 60 °C for 24 h. The soda-lime glass substrates were cleaned and then cut into around 1 cm<sup>2</sup>. A 25  $\mu\text{l}$  45 wt%  $\text{CH}_3\text{NH}_3\text{PbI}_3$  DMF solution, prepared from  $\text{PbI}_2$  and  $\text{CH}_3\text{NH}_3\text{I}$  in a molar ratio of 1:1, was spread on it, using a spin-coater. For the conventional spin-coating method, the solution was spun at 6500 rpm for 30 s, while for the gas-assisted method, a 40 psi dry Argon gas stream was blown over the film during spinning at 6500 rpm for 2 s after the spin-coating commenced. The films were then annealed at 100 °C on a hotplate for 10 min, and then cooled to room temperature on a steel substrate.

#### **CsPbIBr<sub>2</sub>:**

Boro-silicate glass was cleaned by sonication in solutions of 2% Hellmanex in deionized water, acetone, and isopropanol for 15 min. After drying, the substrate was treated by UV ozone cleaner for 10 min. A dual source thermal evaporation of the two precursors cesium iodide (CsI) and lead bromide ( $\text{PbBr}_2$ ) was carried out in a thermal evaporation system (Kurt J. Lesker Mini Spectros) integrated in a glove box. CsI and  $\text{PbBr}_2$  were loaded in separate crucible heaters and the sample substrates were fixed on a rotatable

substrate holder. After the pressure of the evaporator chamber was pumped down to 10<sup>-6</sup> mbar, CsI and PbBr<sub>2</sub> were then heated to the set temperature of 350 °C and 180 °C, respectively. Once the temperatures were reached, the shutter for each source was opened to commence deposition. The temperature of the substrate holder was kept at 75 °C during the deposition. The deposition rates of CsI and PbBr<sub>2</sub> were set at 0.21 Å s<sup>-1</sup> and 0.2 Å s<sup>-1</sup> respectively to achieve a molar ratio of 1:1 for the two materials. After the evaporation, the samples were annealed on a hot plate at 250 °C for 10 min in the glove box.

## C.2 Ultrafast transient absorption

Femtosecond pump-probe TA experiments were performed on MAPbI<sub>3</sub>, FAPbI<sub>3</sub>, MAPbBr<sub>3</sub> and CsPbIBr<sub>2</sub> samples with a TA spectrometer. The laser consisted of a Ti:sapphire mode-locked oscillator that seeded a regenerative amplifier. The output of the amplifier was centered at 800 nm with a repetition rate of 1 kHz and pulse duration of 100 fs, which was then split into pump and probe beamlines. The 400 nm pump pulses were generated using a BBO crystal and were attenuated. The probe beam passed through a delay stage and was used to generate a white light continuum. The probe beam was then detected by a polychromatic-CCD. All of the measurements were performed at room temperature (295 K).

Lattice heating by the pump laser is shown to be a minor effect in our measurements. Supposing that all the laser energy that is absorbed by the sample heats the lattice directly, the temperature change can be calculated as below

$$\Delta T_L = \frac{E_{\text{pump}}}{C_V \cdot V_{\text{pump}}} = \frac{F_{\text{pump}} \cdot \alpha_{400}}{C_V} \quad (\text{C.1})$$

In the above equation,  $C_V$  is the volume heat capacity of perovskites,  $E_{\text{pump}}$  is the pumping energy,  $F_{\text{pump}}$  is the corresponding fluence,  $V_{\text{pump}}$  is excitation volume in the sample and  $\alpha_{400}$  is the absorption coefficient of the material at 400 nm. The typical value of  $C_V$  can be found in Ref. [199] which is about  $1.25 \times 10^6 \text{ J m}^{-3} \text{ K}$  at 300 K. With the maximum excitation fluence  $100 \mu\text{J cm}^{-2}$ , the maximum temperature increase is only about 15-20 K. In practice, considering most of the incident energy will be directly absorbed by the carriers and also given the material's finite thermal conductivity, the actual lattice heating resulting from the laser will be much smaller than the maximum value we deduced above. Therefore, we conclude that direct lattice heating has a negligible impact

on our analysis and cannot explain the significant difference in the carrier relaxation in different perovskites samples.

### C.3 Carrier injection level estimation

The initial photogenerated carrier concentration  $N_0$  is estimated using the following equation.

$$N_0 = \frac{A(\lambda) \times F}{E_{\text{ph}}(\lambda) \times W} \quad (\text{C.2})$$

, where  $F$  is the total incident fluence at excitation wavelength  $\lambda = 400$  nm, photon energy  $E_{\text{ph}}(\lambda) \approx 4.97 \times 10^{-13}$   $\mu\text{J}$ , sample thickness  $W \approx 300$  nm,  $A(\lambda)$  is the overall absorbance of the thin film. When the absorption thickness is much smaller than  $W$ , the absorbance can be analytically estimated by

$$A(\lambda) = 1 - R - T = \left(1 - e^{-\alpha(\lambda) \cdot W}\right) \cdot (1 - R) \quad (\text{C.3})$$

, where  $R$  and  $T$  are the reflectance and transmittance respectively,  $\alpha\lambda$  is the absorption coefficient of the material. For the four lead-halide perovskite samples discussed here, the overall absorbance is about  $A(400\text{nm}) \approx 0.8$  at 400 nm according to previous reports [162–164, 205], where most of the loss in absorption comes from surface reflections. Therefore,  $N_0$  is estimated as  $5.38 \times 10^{18}$   $\text{cm}^{-3}$  when  $F = 100$   $\mu\text{J cm}^{-2}$ .

### C.4 Calculation of phonon band structure

The density functional theory (DFT) calculations were carried out using Quantum Espresso [206]. The Perdew-Ernzerhof-Burke (PBE) functional [207] was used to evaluate the ground state properties, electron and phonon properties. The plane-wave energy cutoff was set to 100 Ry, while a grid of  $6 \times 6 \times 6$  was used for  $\mathbf{k}$ -point sampling. The tolerance for the electronic system was set to 10-12 Ry, while that for the phonon calculations was set to 10-14 Ry. Density functional perturbation theory (DFPT) was used to predict the phonon energies at a  $4 \times 4 \times 4$  grid of  $\mathbf{Q}$  points for  $\text{FAPbI}_3$ ,  $\text{MAPbI}_3$ , and  $\text{CsPbBr}_3$ . Lattice constants for the calculations are given in Table C.1. The phonon band structures were then interpolated from this grid using the interatomic force constants. The phonon band structure for  $\text{MAPbBr}_3$  is extrapolated using the mass approximation approach [208] with the force constants for  $\text{MAPbI}_3$ .

APPENDIX C. METHODS OF TRANSIENT ABSORPTION CHARACTERIZATION  
OF LEAD-HALIDE PEROVSKITES

---

Table C.1: Lattice constants used for phonon band structure calculation in DFT. The phonon band structure for MAPbBr<sub>3</sub> is extrapolated using the mass approximation approach with the force constants for MAPbI<sub>3</sub>

Material	MAPbI <sub>3</sub>	FAPbI <sub>3</sub>	CsPbBr <sub>3</sub>
E <sub>g</sub> (eV)	1.77	1.439	1.731
Lattice constant (Å)	6.29012	a=6.3620 b=6.1930 c=6.3513	5.9595

APPENDIX C. METHODS OF TRANSIENT ABSORPTION CHARACTERIZATION  
OF LEAD-HALIDE PEROVSKITES

---

## Appendix D

# Sensitivity and stability analysis of carrier temperature fitting in lead-halide perovskites

All carrier temperatures are fitted using the method developed in the main text for the lead-halide perovskite samples.

To estimate the global reliability of the fitting results, the fitting procedure is repeated with three different tail lengths  $L$  that are 0.15 eV, 0.2eV, and 0.3 eV respectively. All the fitting results are summarized in Figure D.1 below. In most of the cases, our fitting scheme shows reasonably stable and reproducible fitting results under different  $L$ , especially after a time delay of about 10 ps where most of our discussions and comparisons are made. Most of the large variations are in the first few picoseconds especially when  $L$  is small. Large variations in the fitting results also appear when the carrier injection is low, which results from the data quality of the transient absorption (TA) spectra.

The adopted fitting scheme only has two input parameters that are the tail head ratio  $R$  and tail length  $L$ . Based on the fitting results with different  $R$  and  $L$  in Figure D.1, the first order sensitivity index  $S_R(t)$  of the fitting results on the parameter  $R$  is analyzed. This indicates the influence from the starting point of high-energy tails. The first order sensitivity index is defined as

$$\begin{aligned} S_R(t) &= \frac{V(E(T_c(t)|R))}{V(T_c(t))} \\ &= \frac{V(E(T_c(t)|R))}{E(V(T_c(t)|R)) + V(E(T_c(t)|R))} \end{aligned} \tag{D.1}$$

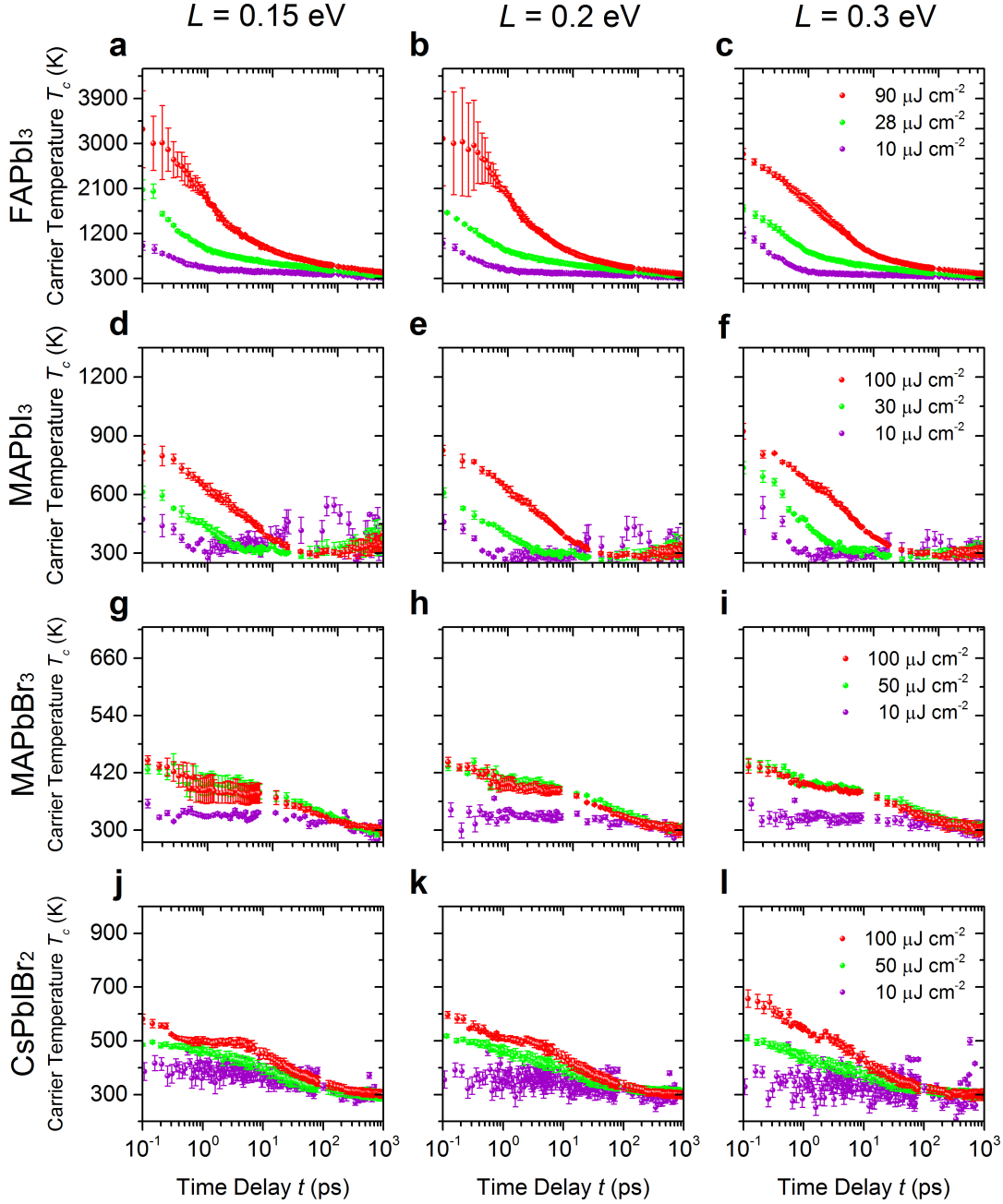


Figure D.1: Averaged carrier temperature fitting results with different tail length  $L$  (0.15 eV, 0.2eV, and 0.3 eV). At the same time delay  $t$ , an average fitting result is shown in the graph when the tail head  $R$  is changed between 1/2 and 1/5. The error bar shows the corresponding standard error (s.e.m) of the average temperature. In the main text and below, we use the fitting results with  $L = 0.3$  eV to conduct other analyses

, where function  $V$  calculates the variation while function  $E$  takes the mean of the values. The term  $V(E(T_c(t)|R))$  denotes the variation of the averaged carrier temperature for a certain time delay  $t$  when keeping the  $R$  as a constant but varying  $L$ . Similarly,  $E(V(T_c(t)|R))$  means the average of the variation of the fitted temperatures.

Figure D.2 shows the statistical distribution of  $S_R(t)$  in each sample, while Figure D.3 shows the distribution of the normalized standard error when varying  $R$ . The normalized standard error is defined as a standard error divided by its corresponding mean. All the distributions are counted over the entire time delay period. Roughly speaking, the variation of  $R$  contributes about 50% to the variation of the final fitted temperature as shown in Figure D.2. However, according to Figure D.3, most of the fitting standard errors are distributed around and below 5% when varying  $R$ . This illustrates that the actual numerical impact from the selection of tail starting point is very small. Therefore, we conclude that the numerical results based on our fitting scheme are reasonably stable and insensitive to the choice of the high-energy tail. All the fitting results are reliable and comparable. In the main text and below, we use the fitting results with  $L = 0.3$  eV (the third column in Supplementary Figure D.1) to conduct other analyses.

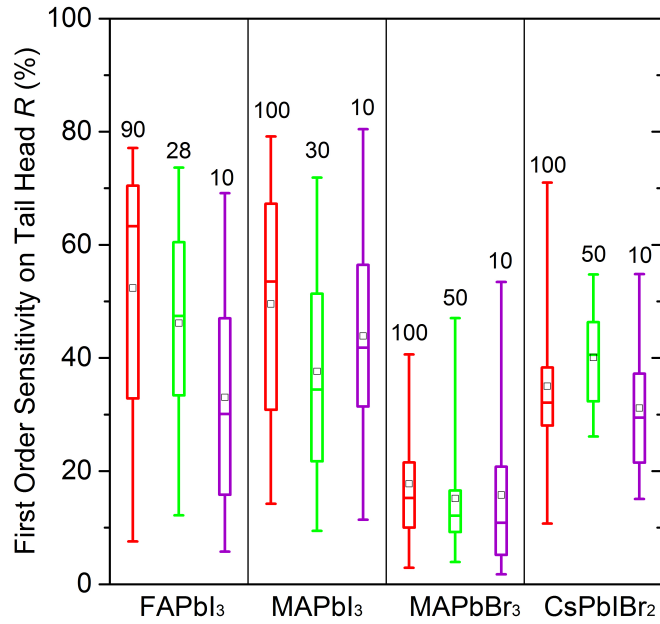


Figure D.2: Statistical distribution of  $S_R(t)$  to the carrier temperature fitting over the entire time delay  $t$  is shown in the box plots. The distributions are counted over the entire time delay period. The boxes show the first and third quartiles of the distribution with the median band inside, while the whiskers label 1.5 times of the interquartile range ( $1.5 \times \text{IQR}$ ). The square dot in the boxes shows the mean of the distribution. Each material has three box plots under different excitation fluences labeled at top of the boxes (unit:  $\mu\text{J cm}^{-2}$ ).

APPENDIX D. SENSITIVITY AND STABILITY ANALYSIS OF CARRIER TEMPERATURE FITTING IN LEAD-HALIDE PEROVSKITES

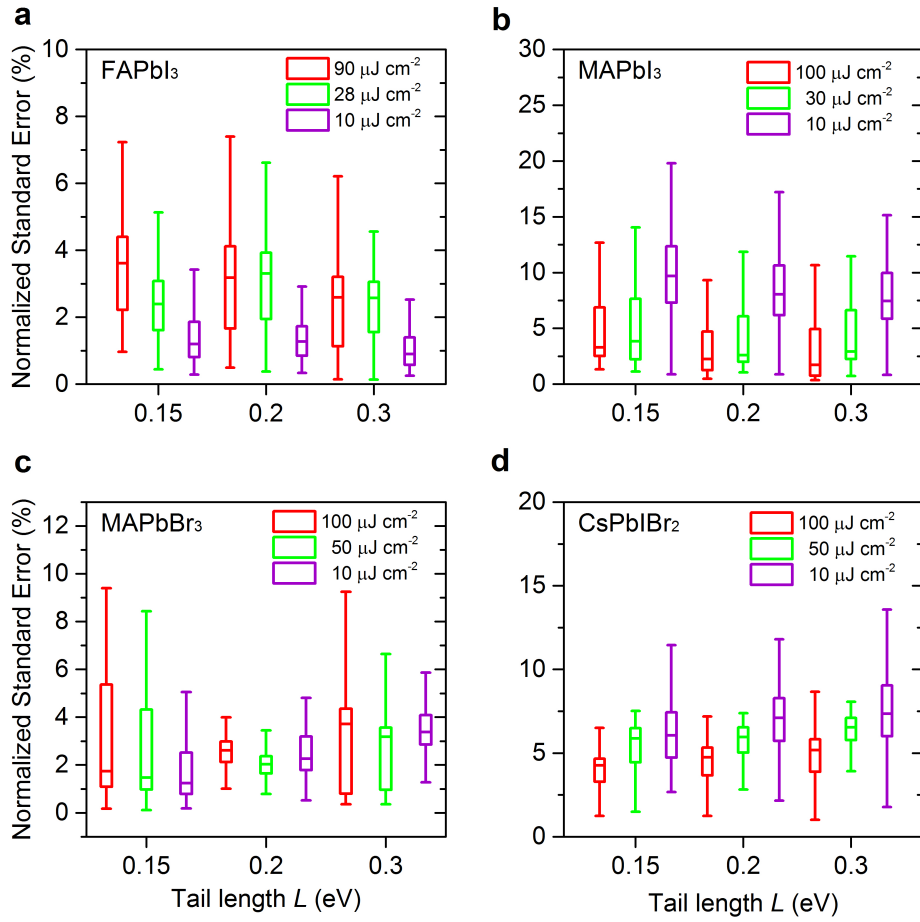


Figure D.3: Statistical distribution of the normalized fitting standard error when varying the tail head ratio  $R$  under different tail lengths  $L$ . The distributions are counted over the entire time delay period. The boxes show the first and third quartiles of the distribution with the median band inside, while the whiskers label 1.5 times of the interquartile range ( $1.5 \times \text{IQR}$ ).